

SPECTROSCOPIC INVESTIGATIONS ON Eu^{3+} AND Nd^{3+} IN CERTAIN SINGLE CRYSTALS

A Thesis Submitted
In partial Fulfilment of the Requirements
for the Degree of
DOCTOR OF PHILOSOPHY

By
U. VIGNANESWARA KUMAR

TH
Phys 1875/D
K96 S.

to the

DEPARTMENT OF PHYSICS

INDIAN INSTITUTE OF TECHNOLOGY KANPUR

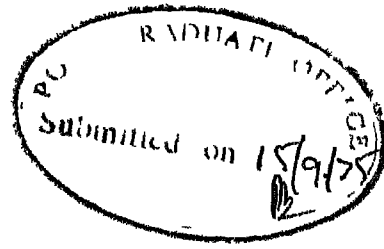
SEPTEMBER, 1975

PHY-1975-D-KUM-SPE

I.I.I. H. FUR
CENTRAL LIBRARY
Acc. No. **A 51158**

22 SEP 1977

TO
MY PARENTS



CERTIFICATE

This is to certify that the work presented in this thesis is the original work of Mr. U. Vignaneswara Kumar done under my supervision and it is not submitted elsewhere for a degree.

Putchha Venkateswarlu
(Putchha Venkateswarlu)
Senior Professor of Physics
Indian Institute of Technology
Kanpur, (U.P.) India

ACKNOWLEDGEMENTS

I am very grateful to Professor P. Venkateswarlu for introducing me to the field of Optical Spectroscopy and his kind encouragement and guidance. The help and active involvement of Professor D. Ramachandra Rao is gratefully acknowledged. I am very thankful to both of them for their interest in my welfare.

I am much indebted to Professor B.D. Nageswara Rao, who initiated me into research, for his kind guidance during the early part of my graduate career.

I sincerely thank Professor T.M. Srinivasan for his help and co-operation during the experiments done with liquid helium. Thanks are also due, to Dr. K.S. Gandhi of the Chemical Engineering Department for help in the design of the heat exchanger used in the work.

The author is indebted to Professor H.P. Broida of the University of California at Santa Barbara for the loan of the single crystals used in the work through Professor Venkateswarlu. Some initial experimental work carried out by Dr. Venkateswarlu and Dr. J.J. Kim at Santa Barbara was helpful to the author in planning and carrying out further detailed work at Kanpur, and for this the author is thankful to them.

It is a pleasure to thank my many colleagues for the companionship and co-operation they have extended to me. Particular mention is here made of M/s. A. Sivaram,

H. Jagannath and D. Madhavan. I have benefitted highly from my association with Drs. R. Janakiraman and M.D. Sastry. Mr. Bansilal has been a source of help and assistance althrough. His cheerful disposition has gone a long way in solving many of the problems we faced. I am very much thankful to him. To my friends who have helped in the preparation of the thesis I am much thankful.

I am very thankful to the staff of our Spectroscopy laboratories for the assistance they have provided me. My thanks are also due to the staff of the Physics Electronics shop, the Low Temperature laboratory, the Central Glass-shop; Mr. N.V.G. Swamy for help in the laboratory, Mr. K.S. Ubhey for the machanical fabrication, Mr. R.K. Bajpai for the tracings, and Mr. H.K. Panda for the cyclostyling work.

I appreciate Smt. Rukmini Devi for her neat and patient typing of the manuscript.

The financial assistance of the National Bureau of Standards, Washington for the purchase of some equipment used in the work, is gratefully acknowledged.

U Vignaneswara Kumar.
U. Vignaneswara Kumar

CONTENTS

LIST OF FIGURES	viii
LIST OF TABLES	xii
SYNOPSIS	xiv
CHAPTER 1	
INTRODUCTION	1
REFERENCES	10
CHAPTER 2	
'EXPERIMENTAL DETAILS'	
ABSTRACT	11
2.1 Spectrophotometer set-up for use with Argon ion laser.	
1. Basic description	12
2. The Argon ion laser used	14
3. Cooling unit for the laser	16
4. Illumination and collection optics	19
5. Crystal mounting and cooling	21
6. Polarizers	23
7. The spectrometer	23
8. Photomultiplier tubes and cooled housings	25
9. Electronics	32
10. Wavelength markers and calibration	32
11. Sensitivity test	35
2.2 Spectrophotometer used in Santa Barbara.	35
2.3 Experimental arrangement with the nitrogen laser excitation.	38
2.4 Optical absorption set-up.	39
REFERENCES	41
CHAPTER 3	
'OPTICAL ABSORPTION AND FLUORESCENCE SPECTRA OF $\text{Eu}^{3+}:\text{LaF}_3$ AT LNT'	
ABSTRACT	43

3.1	Introduction	44
3.2	Crystal structure of LaF_3	45
3.3	The absorption and fluorescence spectra at LNT.	
1.	General remarks	53
2.	Transitions involving the $7F_0$ ground state	56
3.	Fluorescence terminating in $7F_1$	67
4.	Fluorescence terminating in $7F_2$	74
5.	Fluorescence terminating in $7F_3$	78
6.	Fluorescence terminating in $7F_4$	80
7.	Fluorescence terminating in $7F_5$	89
	CONCLUSION	92
	REFERENCES	96
CHAPTER 4		
	'OPTICAL ABSORPTION AND FLUORESCENCE SPECTRA OF $\text{Nd}^{3+}:\text{LaF}_3$ '	
	ABSTRACT	98
4.1	Introduction	100
4.2	The optical absorption spectrum at LNT	104
4.3	The fluorescence spectrum at LNT	116
4.4	Two photon absorption under laser excitation	152
4.5	Oscillator strength determination from self-absorption	156
4.6	The fluorescence spectrum at high temperatures	170
4.7	Polarization of the observed lines	175
	REFERENCES	177
CHAPTER 5		
	THE EPR SPECTRUM OF Nd^{3+} IN LaF_3 AND PbMoO_4 AT LIQUID HELIUM TEMPERATURE'	
	ABSTRACT	180
5.1	Introduction	181
5.2	The spin Hamiltonian	182
5.3	Experimental details	183
5.4	The EPR spectrum of $\text{Nd}^{3+}:\text{LaF}_3$	186
5.5	The EPR spectrum of $\text{Nd}^{3+}:\text{PbMoO}_4$	188
5.6	Forbidden transitions in the EPR spectrum of $\text{Nd}^{3+}:\text{PbMoO}_4$	196
	REFERENCES	201

LIST OF FIGURES

1.1	Two types of ion pair exchange processes	8
2.1	Block diagram of the spectrophotometer set-up used with Argon ion laser excitation.	13
2.2	Block diagram of the cooling unit for the Argon ion laser.	17
2.3	Cross section of the heat exchanger.	18
2.4	Profile of a focussed gaussian laser beam.	20
2.5	Cold finger dewar used for work at 77°K.	22
2.6	Cooled housing for the RCA No. 7102 photomultiplier.	26
2.7	Cooled housing for the ITT No. FW130 photomultiplier.	30
2.8	Schematic diagram of the wavelength marker circuit.	33
2.9	Raman spectrum of Benzene: 4880Å, 20mW.	36
2.10	Raman spectrum of Benzene: 4880Å, 500mW.	37
3.1	Free ion energy levels of Eu^{3+} below 40,000 cm^{-1} (from ref. 2).	46
3.2	Orientation of the ionic co-ordinate axes (XYZ) with respect to the crystalline co-ordinate axes (X'Y'Z').	51
3.3	$\text{Eu}^{3+}:\text{LaF}_3$ fluorescence at 77 K, $^5\text{D}_1-^7\text{F}_0$ group.	63
3.4	$\text{Eu}^{3+}:\text{LaF}_3$ fluorescence at 77 K, $^5\text{D}_2-^7\text{F}_0$ group.	64
3.5	$\text{Eu}^{3+}:\text{LaF}_3$ fluorescence at 77K $^5\text{D}_0-^7\text{F}_1$, $^5\text{D}_1-^7\text{F}_1$ and $^5\text{D}_2-^7\text{F}_1$ groups.	68
3.6	Partial energy level diagram of $\text{Eu}^{3+}:\text{LaF}_3$ showing the observed fluorescence transitions at 77°K terminating in $^7\text{F}_1$.	73

3.7	$\text{Eu}^{3+}:\text{LaF}_3$ fluorescence at 77' K, $^5\text{D}_1-^7\text{F}_2$ and $^5\text{D}_1-^7\text{F}_3$ groups.	75
3.8	Partial energy level diagram of $\text{Eu}^{3+}:\text{LaF}_3$ showing the observed fluorescence transitions at 77 K terminating in $^7\text{F}_2$.	77
3.9	$\text{Eu}^{3+}:\text{LaF}_3$ fluorescence at 77' K, $^5\text{D}_2-^7\text{F}_3$ group.	81
3.10	Partial energy level diagram of $\text{Eu}^{3+}:\text{LaF}_3$ showing the observed fluorescence transitions at 77' K terminating in $^7\text{F}_3$.	82
3.11	$\text{Eu}^{3+}:\text{LaF}_3$ fluorescence at 77" K, $^5\text{D}_0-^7\text{F}_4$ group.	84
3.12	$\text{Eu}^{3+}:\text{LaF}_3$ fluorescence at 77 K, $^5\text{D}_1-^7\text{F}_4$ group	85
3.13	Partial energy level diagram of $\text{Eu}^{3+}:\text{LaF}_3$ showing the observed fluorescence transitions at 77" K terminating in $^7\text{F}_4$.	88
3.14	$\text{Eu}^{3+}:\text{LaF}_3$ fluorescence at 77 K, $^5\text{D}_1-^7\text{F}_5$ group.	90
3.15	$\text{Eu}^{3+}:\text{LaF}_3$ fluorescence at 77' K, $^5\text{D}_2-^7\text{F}_5$ group.	91
4.1	Free ion energy levels of rare earth ions (from Dieke, ref. 2).	102
4.2	$\text{Nd}^{3+}:\text{LaF}_3$ absorption spectrum at 77" K, 2500-4000Å.	105
4.3	$\text{Nd}^{3+}:\text{LaF}_3$ absorption spectrum at 77 K, 4100-4700Å.	113
4.4	$\text{Nd}^{3+}:\text{LaF}_3$ absorption spectrum at 77' K, 4800-5750Å.	114
4.5	$\text{Nd}^{3+}:\text{LaF}_3$ fluorescence at 77' K, 3400-5000Å, obtained with 3371Å excitation.	117
4.6	$\text{Nd}^{3+}:\text{LaF}_3$ fluorescence at 77' K, 6000-9000Å, obtained with 3371Å excitation.	118

4.7 a	E-Z fluorescence at LNT, σ polarization.	119
4.7 b	E-Z fluorescence at LNT, π polarization.	120
4.8	$\text{Nd}^{3+}:\text{LaF}_3$ fluorescence at 77'K, $\text{E}(^4\text{G}_{7/2})$ - $\text{Y}(^4\text{I}_{11/2})$ group; 5145Å excitation.	121
4.9	$\text{Nd}^{3+}:\text{LaF}_3$ fluorescence at 77' K, D-Z($^4\text{I}_{9/2}$) group; 5145Å excitation.	122
4.10	$\text{Nd}^{3+}:\text{LaF}_3$ fluorescence at 77' K, L-S group; 5145Å excitation.	123
4.11	$\text{Nd}^{3+}:\text{LaF}_3$ fluorescence at 77 K, $\text{E}(^4\text{G}_{7/2})$ - $\text{X}(^4\text{I}_{13/2})$ group; 5145Å excitation.	124
4.12	$\text{Nd}^{3+}:\text{LaF}_3$ fluorescence at 77 K, L-A group; 5145Å excitation.	125
4.13	$\text{Nd}^{3+}:\text{LaF}_3$ fluorescence at 77' K, K-S group, 5145Å excitation.	126
4.14	$\text{Nd}^{3+}:\text{LaF}_3$ fluorescence at 77 K, L-B($^4\text{F}_{9/2}$) group; 5145Å excitation.	127
4.15	$\text{Nd}^{3+}:\text{LaF}_3$ fluorescence at 77° K, part of the $\text{R}(^4\text{F}_{3/2})$ -Z($^4\text{I}_{9/2}$) group in σ polarization, showing self absorption; 5145Å excitation.	128
4.16	The variation of the intensity of K and L fluorescence with power.	153
4.17	Variation of the 'line centre intensities' of the R-Z fluorescence lines with path-length x , in σ polarization at 77'K.	164
4.18	Variation of the 'line centre intensities' of the R-Z fluorescence with path-length x in π polarization at 77°K.	165
4.19	Variation of the hump separation (S) of the self reversed lines of the R-Z group with path-length (x) at 77°K.	166

5.1	Configuration of the magnetic fields in the EPR set-up at 4.2°K.	185
5.2	$\text{Nd}^{3+}:\text{LaF}_3$ EPR spectrum at 4.2°K H_0 in a direction perpendicular to the c axis.	187
5.3	Unit cell of PbMoO_4 .	189
5.4	$\text{Nd}^{3+}:\text{PbMoO}_4$ EPR spectrum at 4.2°K. H_0 at 25° from the c axis in an ac plane.	191
5.5	$\text{Nd}^{3+}:\text{PbMoO}_4$ EPR spectrum at 4.2 K, angular variation in the ac plane.	192
5.6	Allowed and forbidden hyper-fine transitions of a spin $\frac{1}{2}$ system.	198
5.7	EPR spectrum of $\text{Nd}^{3+}:\text{PbMoO}_4$ at 4.2°K with $H_0 // c$ axis showing allowed and forbidden hyperfine transitions.	200

LIST OF TABLES

2.1	The various emissions available from Spectra-Physics model 165-03 Argon ion laser.	15
3.1	Selection rules for C_{2v} sites in the D_{6h}^3 structure of LaF_3 a. Electric dipole b. Magnetic dipole	50
3.2	Selection rules for C_s sites in the O_{6v}^3 structure of LaF_3 a. Electric dipole b. Magnetic dipole	50
3.3	Correlation table for C_{2v} and $C_s(YZ)$ groups.	52
3.4	The fluorescence spectrum of $Eu^{3+}:LaF_3$ at LNT.	57
3.5	The absorption spectrum of $Eu^{3+}:LaF_3$ at LNT.	62
3.6	Splitting of the various J states under C_{2v} and C_s symmetries.	66
3.7	Difference matrix for the D_1-F_1 group of fluorescence lines.	70
3.8	Difference matrix for the D_1-F_2 group of fluorescence lines.	76
3.9	Difference matrix for the D_1-F_3 group of fluorescence lines.	79
3.10	Difference matrix for the D_1-F_4 group of fluorescence lines.	86
3.11	The energy levels of $Eu^{3+}:LaF_3$ (0 to 22,000 cm^{-1})	93
4.1	The ultraviolet absorption spectrum of $Nd^{3+}:LaF_3$ at liquid nitrogen temperature.	106
4.2	The energy levels of $Nd^{3+}:LaF_3$	108
4.3	The fluorescence spectrum of $Nd^{3+}:LaF_3$ at LNT obtained with 5145Å (Ar^+) excitation.	131
4.4	The 'Sum' matrix for the 7200Å group of fluorescence lines and the 'S' group of Stark levels.	139

4.5	The fluorescence spectrum of $\text{Nd}^{3+}:\text{LaF}_3$ at LNT obtained with 3371Å (N_2 laser) excitation.	141
4.6	Crystal field splitting of the $^4\text{I}_{9/2}(\text{Z})$ level of $\text{Nd}^{3+}:\text{LaF}_3$ from the fluorescence data.	147
4.7	Crystal field splitting of the $^4\text{I}_{11/2}(\text{Y})$ level of $\text{Nd}^{3+}:\text{LaF}_3$ from the fluorescence data.	148
4.8	Crystal field splitting of the $^4\text{I}_{13/2}(\text{X})$ level of $\text{Nd}^{3+}:\text{LaF}_3$ from the fluorescence data.	149
4.9	Crystal field splitting of the $^4\text{I}_{15/2}(\text{W})$ level of $\text{Nd}^{3+}:\text{LaF}_3$ from the fluorescence data.	150
4.10	Crystal field splitting of the $^4\text{F}_{5/2}, ^2\text{H}_{9/2}(\text{S})$ level of $\text{Nd}^{3+}:\text{LaF}_3$ from the fluorescence data.	151
4.11	Peak absorptivities and oscillator strengths of the transitions between R and Z levels at LNT.	168
4.12	Possible ion pair transitions to populate the 'S' level of Nd^{3+} at high temperatures.	173
4.13	Possible ion pair transitions to populate the 'A' level of Nd^{3+} at high temperatures.	174

SYNOPSIS

The work reported in this thesis mainly deals with the optical absorption and Ar^+ and N_2 laser excited fluorescence spectra of Eu^{3+} and Nd^{3+} in LaF_3 crystals at room and liquid nitrogen temperatures. A chapter of the thesis deals with an investigation of the EPR spectra of Nd^{3+} doped in LaF_3 and PbMoO_4 single crystals at liquid helium temperature. The EPR work was carried out to supplement the optical studies on Nd^{3+} .

The first chapter gives a brief introduction to the spectroscopy of Rare Earth ions and an outline of the theoretical framework relevant to the present studies.

The second chapter is devoted to a description of the experimental details, the assembly of a recording spectrophotometer and the fabrication of a heat exchanger. The spectrophotometer is assembled around a 0.75 m Jarrell-Ash grating spectrograph and is used for recording the fluorescence excited by the Argon ion laser. The lines recorded have a minimum half width (at half maximum) of 1\AA and the wavelengths could be measured to an accuracy of $\pm 1.5\text{\AA}$. Fluorescence excited by the pulsed nitrogen laser is however recorded only photographically. This chapter also describes the fabrication of a 12kW heat exchanger needed to cool the Argon ion laser used (Spectra Physics Model No. 165-03).

Chapter three presents the work on the absorption and fluorescence spectra of $0.5\% \text{Eu}^{3+}:\text{LaF}_3$. Only three lines due to $^5\text{D}_2$ and three lines due to $^5\text{D}_1$ are observed in absorption (4500-9000 \AA). The fluorescence excited by the Argon ion laser consists in all of twelve groups of transitions from $^5\text{D}_{0,1,2}$ to the levels $^7\text{F}_{0,1,2,3,4,5}$ of the ^7F ground multiplet. No transitions to $^7\text{F}_6$ are found. The availability in the Ar^+ laser of several excitation wavelengths was of some help in identifying the upper levels of fluorescence. Using the fluorescence data, positions of all the Stark components of $^5\text{D}_{0,1,2}$ and $^7\text{F}_{1,4}$ levels

are determined. Only three levels of 7F_2 (of the expected five) are determined, as fluorescence to other levels is not observed, while the identification of the Stark components of 7F_3 and 7F_5 was hampered by a multitude of overlapping transitions. Attempts to determine the positions of levels of 7F multiplet by infrared absorption did not bear fruit. LaF_3 has a hexagonal unit cell and the R.E. ions are known to replace the La ions substitutionally at sites of orthorhombic symmetry. The polarizations of lines indicate a C_{2v} site symmetry. Some deviations are however observed which indicate a distortion towards C_s . However, a consistent set of symmetry species assignments could be made to all the observed levels under the classification of a C_{2v} symmetry.

Exciting this crystal with a nitrogen laser resulted only in continuum fluorescence in the blue, most likely due to Eu^{2+} .

The work performed on the optical spectra of 2% Nd^{3+} : LaF_3 is described in the fourth chapter. Five groups of lines are observed in the ultraviolet absorption spectrum (2500-4000Å). The SLJ level designations could be assigned to the concerned levels of four of these groups by comparison with the spectrum reported for Nd^{3+} : LaCl_3 . The absorption spectrum in the region /but 4000-9000Å conforms with earlier data/for the observation of few sharp extra lines. As a reinvestigation of the EPR spectrum of Nd^{3+} : LaF_3 did not produce any new lines, these extra absorption

lines are assigned to be vibronic transitions rather than lines from a different Nd^{3+} centre.

Excitation with the 5145\AA ($19,430\text{ cm}^{-1}$) emission of the Ar^+ laser, at LNT produced fluorescence from the E ($19,300\text{ cm}^{-1}$), D ($17,450\text{ cm}^{-1}$) and R ($11,600\text{ cm}^{-1}$) levels as well as some other fluorescence lines whose intensity was proportional to $P^{1.76}$ where P is the incident laser power. These are identified as arising from the K ($26,400\text{ cm}^{-1}$) and L ($28,350\text{ cm}^{-1}$) levels of the Nd^{3+} . This assignment is confirmed by the fluorescence obtained with N_2 laser excitation (3371\AA) which contained transitions from the K and L levels to several lower levels and also from R to the ground state. A sequential two step excitation process is proposed to explain the population of these two high lying levels when excited with the $19,430\text{ cm}^{-1}$ radiation.

Three lines of the R-Z group showed significant self absorption. The simple geometry of laser excitation permitted an accurate calculation of oscillator strengths of these transitions using this effect.

With the 5145\AA excitation fluorescence from S and A levels also is observed at room temperature beside the fluorescence observed at LNT. The intensity of these two transitions increases with the temperature above RT. This

is explained as due to an anomalous increase in the populations of S and A levels due to an ion pair relaxation process active at high temperatures.

Several lines, in absorption as well as fluorescence are partially polarized contrary to the expected behaviour of Kramers' ions in orthorhombic sites. Some possible explanations are offered for this behaviour but no firm conclusions could be reached.

Chapter five describes a reinvestigation of the EPR spectra at liquid helium temperatures of $\text{Nd}^{3+}:\text{LaF}_3$ and $\text{Nd}^{3+}:\text{PbMoO}_4$. This is taken up to check whether extra lines found in the respective absorption spectra could be due to the existence of different kinds of Nd centres. No evidence for this was found in LaF_3 . In PbMoO_4 however the EPR spectrum contained a set of lines attributable to Nd^{3+} possibly associated with a next neighbour defect in the [110] plane. The intensity of these lines is less than 1% of the main lines which are due to Nd^{3+} experiencing a crystal field of S_4 symmetry oriented along the C axis of the crystal.

CHAPTER 1

INTRODUCTION

Europium and Neodymium are the fourth and seventh members respectively of the Lanthanide series of rare earths which is characterized by the progressive filling of the 4f shell of the electronic configuration. The neutral Lanthanides all possess the Xenon structure of electrons ($1s^2 2s^2 2p^6 3s^2 3p^6 3d^{10} 4s^2 4p^6 4d^{10} 5s^2 5p^6$), n 4f electrons (n=0 to 14) and two or three outer electrons ($6s^2$ or $5d6s^2$). All these outer electrons are shed off in the trivalent state which is their most common valence state. In this state they have only 4f electrons beside their Xenon cores. The maxima of the 4f orbitals fall quite within those of 5s and 5p orbitals and move further inside with increasing nuclear charge (Lanthanide

contraction). The shielding thus accorded to the electrons in the 4f shell by the $5s^2 5p^6$ electrons is the cause of their distinctive properties. The 4f shell behaves as an 'inner' shell and the interaction with the environment is quite weak. There is very little tendency for these ions to form bonds. They retain their 'free ion' properties more or less intact even inside a solid lattice. The wavefunctions remain to be almost pure angular momentum eigenfunctions and the energy levels shift very little from lattice to lattice.

The free ion Hamiltonian of an N electron atom contains three principal parts given by

$$H = \sum_{i=1}^N \left(\frac{\hbar^2}{2m} \nabla_i^2 - \frac{Ze^2}{r_i} \right) + \sum_{i>j}^N \frac{e^2}{r_{ij}} + \sum_{i=1}^N \zeta_i \mathbf{l}_i \cdot \mathbf{s}_i$$

in standard notation. An exact solution of this Hamiltonian has not been possible and one is usually content with a perturbation treatment. The starting point is the zero order approximation in which the outer (4f) electrons are considered to be moving in a central field produced by the nucleus and the 54 electrons of the Xenon core. In this approximation all states of a given configuration have the same energy. The degeneracy of this state for an f^n configuration is $14C_n$ and is very large. Part of this degeneracy is removed with the inclusion of the interelectronic repulsion and spin orbit

interaction. The effect of these terms is usually calculated by a perturbation treatment in which it is assumed that the energy separation between various configurations is large enough for the effect on each configuration to be calculated separately. That is, the different configurations do not interact with each other. Without this assumption, the number of wavefunctions to be considered becomes enormous. The perturbation calculations are usually done in a set of basis states formed according to LS coupling as this is the most realistic approximation for rare earth ions and taking up both the perturbations simultaneously rather than one by one. This is the so called intermediate coupling calculation.

The electronic repulsion term splits the various terms having different L and S (total orbital and spin angular momenta), and the levels with different J values ($J=L+S$ to $L-S$) constituting these terms are separated out by the spin-orbit interaction. Also, the off-diagonal matrix elements of the spin orbit interaction cause mixtures of levels having the same J value but differing in L and S by ± 1 and ∓ 1 respectively. As a result, the levels finally have only one good quantum number J, but L and S are poorly defined. The accepted nomenclature however uses an SLJ designation for these levels. The L and S values refer however to the particular LS state, the eigenstate approaches continuously as ζ_1 approaches zero.

This may not necessarily be the state which constitutes the major percentage of the perturbed state.

The $(2J+1)$ fold degeneracy of these states is lifted in a crystal ^{to} ~~by~~ an extent depending upon the symmetry of the crystal field. The centre of gravity of the split components however stays quite close to the free ion value. A more important effect of the crystal field is - unless the ion is situated at an inversion centre, parity is not a good quantum number. The crystal field brings about a small but finite mixture of the wavefunctions belonging to configurations of different parities, and due to this, electric dipole transitions between levels of a given configuration become formally allowed. These are called forced electric dipole transitions. Since transitions between levels of a single configuration are almost totally forbidden for the free ions, most of the information about the 'free ion' energy levels is thus obtained in practice from crystal spectra only.

In the intermediate coupling calculations, the energy levels are expressed in terms of the so called Slater integrals F_2 , F_4 and F_6 and the spin orbit coupling constant ζ_1 . These quantities cannot be calculated ab initio accurately. For this reason, these are treated as parameters and are optimized to obtain the observed energy level structure.

The energy level structure is experimentally determined mainly from the absorption spectrum. But information about levels to which the transition from the ground state is either forbidden or lies in an inaccessible region of the electromagnetic spectrum can often be obtained from the fluorescence spectrum. As a matter of fact, the Stark splitting of the ground state is almost invariably established from the fluorescence data only. At the low temperatures at which the experiments are done, these higher Stark components are not populated and thus no transitions are observed from them.

The oscillator strengths of these forced electric dipole transitions are very small, of the order of 10^{-6} or less. The allowed magnetic dipole transitions on the other hand have oscillator strengths of about 10^{-8} , and are even weaker. The latter are allowed strictly between states for which $\Delta L=0$, $\Delta S=0$ and $\Delta J=0, \pm 1$. Due to the mixing produced by the spin orbit coupling however, these have a larger occurrence than is obvious from the selection rules. A case in point is the magnetic dipole transitions observed in the spectrum of Eu^{3+} between the Stark levels of the ^5D and ^7F multiplets. The large majority of the observed transitions are however of the forced electric dipole type.

Most of the theoretical as well as experimental problems associated with the observation and analysis of the

energy level structures of several rare earth ions were satisfactorily solved by the mid 1960s. Figure 4.1 (chapter 4) summarizes the information obtained upto about 1968. The emphasis of the later work was mainly towards an understanding of the energy exchange processesⁱⁿ various materials because of their applications as laser hosts and infrared quantum counters (IRQC).

A rare earth ion in an excited electronic level can revert to lower levels in one of several ways: radiative decay, that is fluorescence; energy exchange with other ions in the crystal; or through interaction with lattice phonons. The phonon interaction is very effective when the energy separation of the electronic levels is of the same order as the phonon energies. As a matter of fact, levels which are separated by less than 1000 cm^{-1} from their next lower levels rarely decay by fluorescence; they are invariably deexcited non-radiatively.

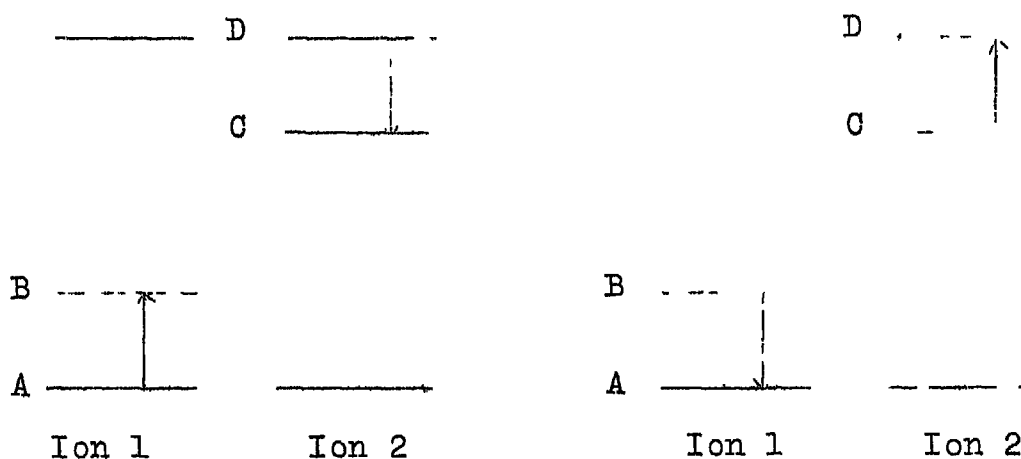
There are three different phonon coupling mechanisms that are usually active. In the direct process, the energy released by a rare earth transition generates a single lattice phonon. In the Raman process the electronic transition is accompanied by the creation and annihilation of two phonons, of different energies. The difference in the energies of the two phonons is equal to the energy of the electronic

transition. The last, the multiphonon process involves the generation of several phonons; not necessarily of the same energy, simultaneous to an electronic transition. The direct process and the Raman process depend on the density of the lattice phonons and their efficiency increases with temperature. The multiphonon process is however essentially temperature independent and is active even at the lowest temperatures (about 2°K) investigated so far. The importance of these processes is demonstrated by the following.

Almost all observed lines of the rare earth spectra show Lorentzian shapes characteristic of lifetime broadening. This broadening completely masks the inhomogeneous broadening caused by strains or other statistical factors except in a few cases. The linewidths are typically of the order of a few cm^{-1} in most cases and reflect non-radiative transition rates in excess of 10^{13} per sec. The observed radiative lifetimes are in the range of a few microseconds to few milliseconds and cannot give rise to such large widths.

Significant energy transfer rates between ions separated by large distances are observed in rare earth spectroscopy. The mechanism responsible for this is the overlap of the electric dipole fields of the ions concerned. The overlap of the wavefunctions as such cannot be effective beyond a short distance. The effects of this interaction

are twofold. Inhomogeneous broadening of the lines due to slight differences in the crystal field experienced by different ions and shortening of lifetimes or concentration quenching of fluorescence due to ionic cross relaxation when the emission and absorption bands of the ions overlap. The exchange process, also called ion pair exchange is of two types. As shown in the figure below, the exchange process might lead to excitation of ion 1 and a deexcitation of ion 2,



$$E_{AB} = E_{CD}$$

Figure 1.1 Two types of ion pair exchange processes

or a further excitation of ion 2 and a decay of ion 1. The latter process is also called energy up-conversion and is of interest in IRQC applications.

An analysis and understanding of these non-radiative processes is the aim of most of the current studies and a vast amount of literature exists on the subject. Only a cursory review of the salient features necessary for this thesis is presented here. A list of a few general references is attached.

REFERENCES

1. G.H. Dieke, Spectra and Energy Levels of Rare Earth Ions in Crystals (Interscience 1968).
2. Optical Properties of Rare Earth Ions in Crystals. ed. H.M. Crosswhite and H.W. Moos (Interscience 1967).
3. B.G. Wybourne, Spectroscopic Properties of Rare Earths (Interscience 1965).
4. B.R. Judd, Operator Techniques in Atomic Spectroscopy (Mc. Graw Hill, New York 1963).
5. R. Orbach, in Fluctuations, Relaxation and Resonance in Magnetic Systems. ed. D. ter Haar (Oliver and Boyd, Edinburgh 1961).
6. I. Waller, Zs. f. Physik, 79, 370 (1932).
7. J.H. Van Vleck, Phys. Rev. 57, 426 (1940).
8. W.M. Yen, W.C. Scott and A.L. Schawlow, Phys. Rev. 136, A271 (1964).
9. Th. P.S. Botden, Phillips Res. Rept. 6, 425 (1951).
10. L.G. Van Uitert and S. Iida, J. Chem. Phys. 37, 986 (1962).

CHAPTER 2

EXPERIMENTAL DETAILS

ABSTRACT

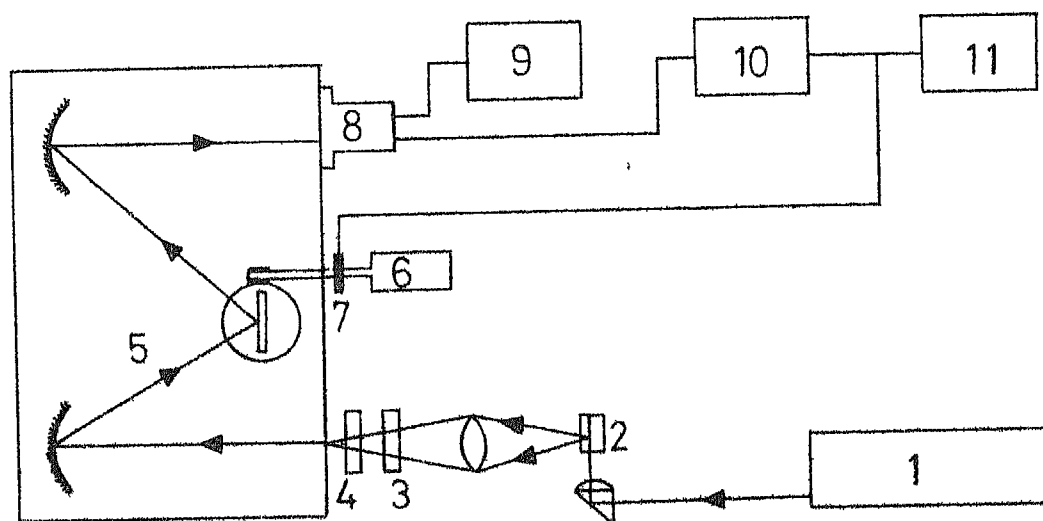
Fluorescence spectra are recorded using Ar^+ and N_2 laser excitations. A spectrophotometer set-up assembled around a Jarrell-Ash 0.75 m. grating spectrograph is used for recording the fluorescence excited by the Argon ion laser. The lines recorded have a minimum half width (at half maximum) of 1\AA and the wavelengths could be measured to an accuracy of $\pm 1.5\text{\AA}$. Fluorescence excited by the pulsed nitrogen laser is recorded photographically. A 12kW heat exchanger needed to cool the Argon ion laser used is also fabricated. The optical absorption spectra in the region 2500-9000 \AA are photographed on a Jarrell-Ash 3.4 m. grating spectrograph in the first order.

2.1 Spectrophotometer set up for use with the Argon ion laser

2.1.1 Basic description

This set-up is built⁺ around a Jarrell-Ash 0.75 m plane grating spectrograph that is converted for photometric recording. The block diagram of the set-up is shown in figure 2.1. The laser beam is made vertical by a right angled prism and enters the bottom face of the crystal under study. The fluorescence emitted is collected in a direction perpendicular to that of the laser beam, and imaged on to the slit of the spectrometer as a vertical line parallel to it. The diffracted light is detected by a photomultiplier tube placed directly in front of the exit slit and the current produced in it is recorded by an electrometer, strip chart recorder combination.

⁺ This recording spectrophotometer has been jointly planned and assembled by the author and Mr. Bansilal, his colleague in the laboratory.



- | | |
|------------------|--------------------------|
| 1. Laser | 7. Cam and microswitch |
| 2. Crystal | 8. Photomultiplier tube |
| 3. Polarizer | 9. H V Power supply |
| 4. Filter | 10. Picoammeter |
| 5. Monochromator | 11. Strip chart recorder |
| 6. Motor | |

Fig. 2.1, Block diagram of the spectrophotometer set-up used with Argon Ion laser excitation.

Wavelength scanning is accomplished by a variable speed D.C. motor attached to the grating drive shaft. A cam and micro-switch mounted on this shaft provide markers for wavelength calibration.

2.1.2 The Argon ion laser used

The laser used is a Spectra Physics Model 165-03, equipped with an intra-cavity tuning prism to select the lasing wavelength. Table 2.1 lists the available wavelengths and their maximum powers as per the manufacturers' specifications. The output power can be varied by varying the discharge current of the laser plasma tube between 10 and 35 amperes. An intra-cavity iris diaphragm is also provided to further reduce the power if needed, to levels below that obtainable with the minimum current. The output power of the laser is monitored by a built-in photo-cell which receives a small part of the light. A provision is available to use the photo-cell voltage in a feed back loop to maintain the output power constant at any desired level, irrespective of changes in the line voltage, plasma tube temperature etc. Most of the recordings made in this work are done in this 'Light control' mode of operation. The values of 'power' quoted throughout this thesis are the values measured by this photo-cell in the laser head itself. The power that actually enters the crystal will be 35 to 40% less than this because of reflection losses suffered by the beam on the way.

Table 2.1

The various emissions available from Spectra-Physics Model 165-03

Argon ion Laser

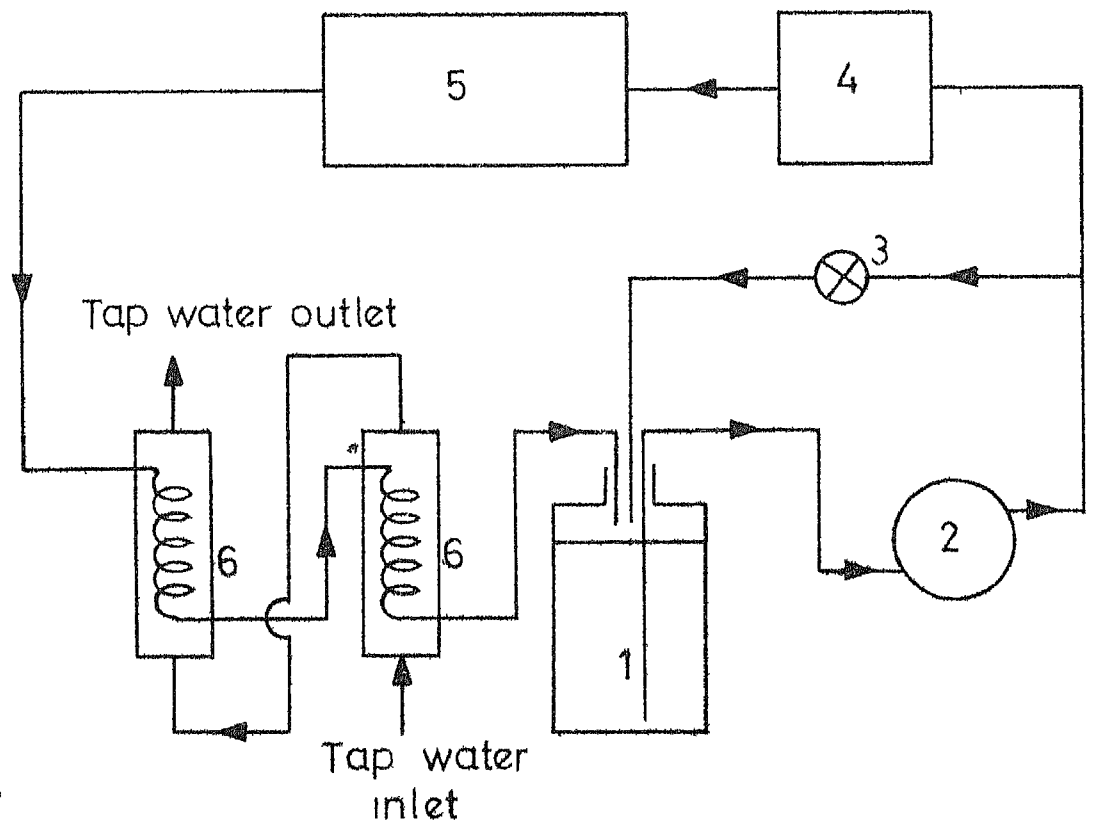
Wavelength \AA	Wavenumber cm^{-1}	Power mw
5145	19431	1400
5017	19927	250
4965	20135	400
4880	20486	1300
4765	20980	500
4727	21149	150
4658	21462	100
4579	21832	250

2.1.3 Cooling unit for the laser

The laser and its power supply together consume maximum of 12kW of electrical power and have to be water cooled to prevent over-heating. The manufacturer recommends cooling with clean dust free water and to this end, a unit has been built to cool the laser unit (laser head and power supply) by circulating distilled water which is in turn cooled by running tap water in a heat exchanger. Figure 2.2 shows the block diagram of the cooling unit.

The heat exchanger is of standard counter current design⁺ (figure 2.3) in which the distilled water flows inside a 9/16" inner diameter thin walled copper tube (seamless, coil grade) wound spirally between two concentric steel drums of 12" and 14" diameter. The tap water flows in the remainder of the annular region between the two drums. The flow directions are as shown in figure 2.3. For convenience, the heat exchanger is split up into two such similarly built units connected in series (figure 2.2). Each unit contains 20 turns of copper coil. The drums are fabricated (Silicon bronze welding) with 22SWG mild steel sheet and painted with one coat of lead oxide primer paint and two coats of black bitumen anticorrosive paint to prevent corrosion by the flowing water. The rate of flow of distilled water is 10 lit/min at a pressure of 40-50 psi (values recommended by Spectra

⁺ This heat exchanger is designed and fabricated in association with Dr. K.S. Gandhi of the Chemical Engineering Department, IIT Kanpur.



1. Distilled water storage tank (50 litres)
2. Pump
3. Bypass valve to regulate water pressure
4. Particle filter
5. Laser and power supply
6. Heat exchangers

Fig. 2.2 Block diagram of the cooling unit for the Argon ion laser.

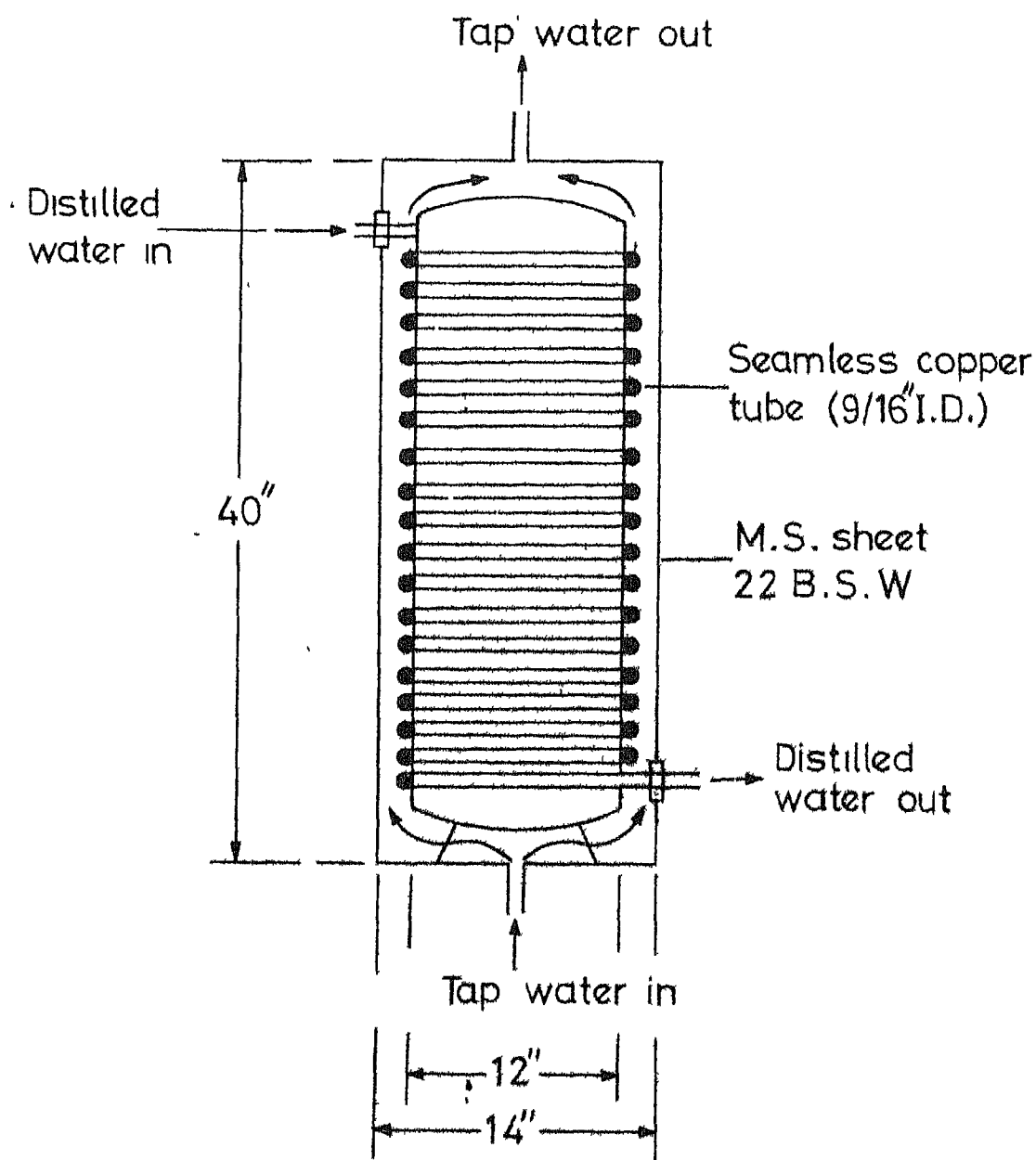


Fig. 2.3 Cross section of the heat exchanger.

Physics) and is obtained by a Beacon (India) No.1-TPS-2M, 0.5 H.P. pump. The rate of flow of tap water is 35 lit/min and is obtained from a 1/2" pipe connected to the campus mains (tube well pumped) .

2.1.4 Illumination and collection optics

The illuminating optics (for the laser beam) consists of a single plano convex lens of 2" focal length glued on top of the right angle prism that bends the beam upwards. The laser beam diameter between $1/e^2$ points (Gaussian profile) is specified to be 1.5 mm or about 1 mm between $1/e$ points. The beam 'waist' diameter of a focussed laser beam is given by¹ $d = 2\lambda/\pi\phi$, where ϕ is the semi-angle of convergence shown in figure 2.4. For a beam of 5000\AA , and 1 mm diameter, 'd' would be 14μ between $1/e$ points with the 2" focal length used. And at 100 mw incident power, the average photon flux (5000\AA) within this area (of diameter 14μ) is calculated as 1.25×10^{16} photons $\text{cm}^{-2} \text{sec}^{-1}$. Thus for the power range of 60 to 700 mw used in this work, a photon flux of about 10^{15} - 10^{16} photons $\text{cm}^{-2} \text{sec}^{-1}$ is obtained. The right angle prism, lens assembly used here is taken out of a Carl-Zeiss electrode illuminator lamp and is used as such. The working distance of 2" provided by this is found convenient for working with the crystals mounted inside a low temperature dewar.

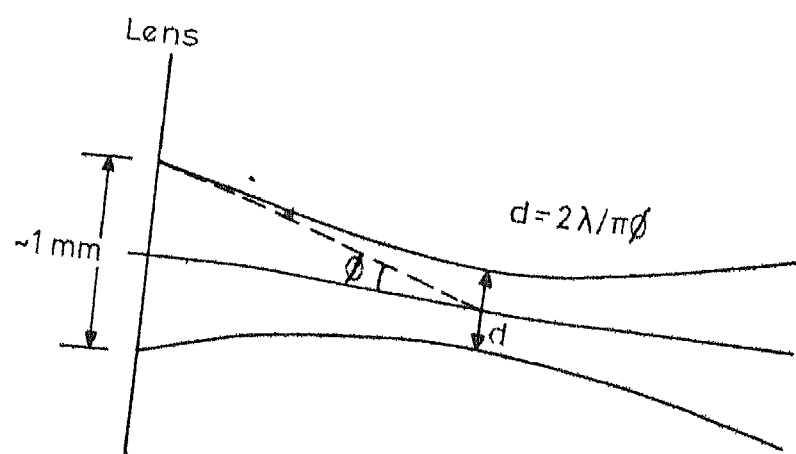


FIG. 2.4 Profile of a focused Gaussian laser port.

The collection optics for the fluorescence consists of a single double convex lens of 2" focus and 2" aperture and is so chosen as to 'overfill' the collimating mirror of the f/6.3 spectrometer used. The source of fluorescence being a narrow vertical line, such a system which simply images this 'line' on to the slit is adequate.

2.1.5 Crystal mounting and cooling

Most of the work is done by cooling the crystals to liquid nitrogen temperatures. For this, the crystals are mounted inside a demountable cold finger dewar fabricated in our glass shop. This is of usual design and is illustrated in figure 2.5. The body of the dewar is made from a B55 glass joint. The inner tube of the dewar terminates in a glass to metal (covar) seal and a stout copper cylinder silver soldered to this covar tube provides the cold finger. The crystal is usually fixed with QuickfixTM (Wembley-India) on a 1/2" thick copper block which can be attached to the cold finger by 1/8" BSW screws. The crystal is protected from room temperature radiation by another 1/2" copper block similarly screwed to the cold finger. Thermal contact between the metal surfaces is improved by applying a layer of grease between them. 2" diameter plate glass windows are provided on the 'tail' of the dewar to facilitate the entry and extraction of light. The windows are attached with Torr SealTM (Varian) or

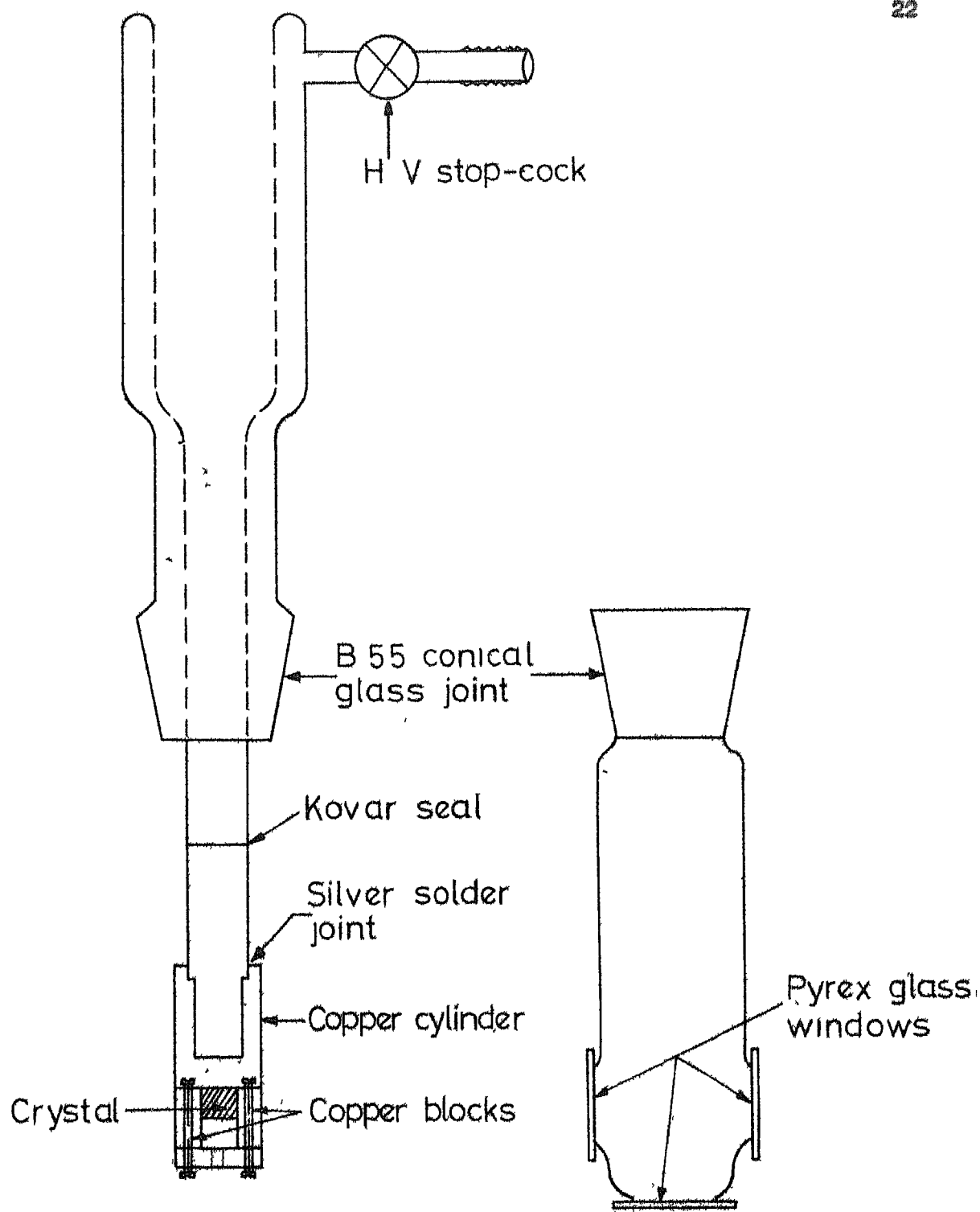


Fig. 2.5 Gold finger dewar used for work at 77°K.

AralditeTM (Ciba) on to window seats ground for the purpose. A dewar similar in design but equipped with 1" diameter quartz windows is used for work in the ultra violet region.

2.1.6 Polarizers

A Polaroid sheet held between glass plates is found adequate for the region 4000-7000Å. It did not work in the infrared region, and a Glan-Thomson polarizer⁺ is used for the region 7000-9000Å.

2.1.7 The spectrometer

The following easily recognizable criteria are used to select a suitable instrument for the work. (a) constancy of focal plane with wavelength, (b) linear wavelength scanning, (c) high light gathering power, and (d) moderate resolving power. All these criteria are found to be adequately met by a Jarrell Ash 0.75 m. plane grating spectrograph available in the laboratory^δ. It uses an asymmetric Czerny-Turner mounting and has a rather large f/6.3 aperture. Standard accessories are supplied alongwith the instrument to convert it from photographic to photometric (direct reading) mode. However the conversion involves a complete removal of the exit side face plate and necessitates a cumbersome focussing procedure when it has to be equipped again for photography. This being very undesirable in a laboratory where spectrographs

⁺ This was kindly loaned to us by Dr. S.C. Sen of our department.

^δ This spectrograph is kindly loaned to us by Professor V. Subbarao of the Chemical Engineering Department.

have to be shared between various workers it is decided not to use the J-A accessory. Instead, an 'exit slit mount' is made of exactly the same dimensions as the photographic plate holder and can be clamped to the face of the spectrograph using the same clamping arrangement as for the plate holder. A Jarrell-Ash No. 12-000 precision bilateral slit (10-400 μ) is mounted on this plate. The plate factor of the spectrograph is about 20 \AA /mm with a 15,000 LPI grating. Alternately the scanning speed is 550 \AA per one degree rotation of the grating. The spectrograph comes equipped with an angle drive and a reduction gear train so that, one revolution of the grating drive shaft results in a 0.1 degree rotation of the grating. A four position mechanical counter reads the grating rotation angle to the second decimal place. The grating used is blazed at 5000 \AA .

A Bodine No. NSH-12RG reversible D.C motor fed by Minarik electronics No. 1214, 115V regulated D.C. source is used for grating rotation. The speed of the motor can be varied in six steps⁺ between 0.8 and 3 RPM by changing the D.C. voltage. This corresponds to wavelength scanning of 45 to 165 \AA /min. A speed of 100 \AA /min is generally employed.

The minimum linewidth of the lines recorded and consequently the experimental resolution is limited essentially by the width of slits used: 50 to 150 μ on the input side and 100 μ on the output side. The sharp lines of a Geissler

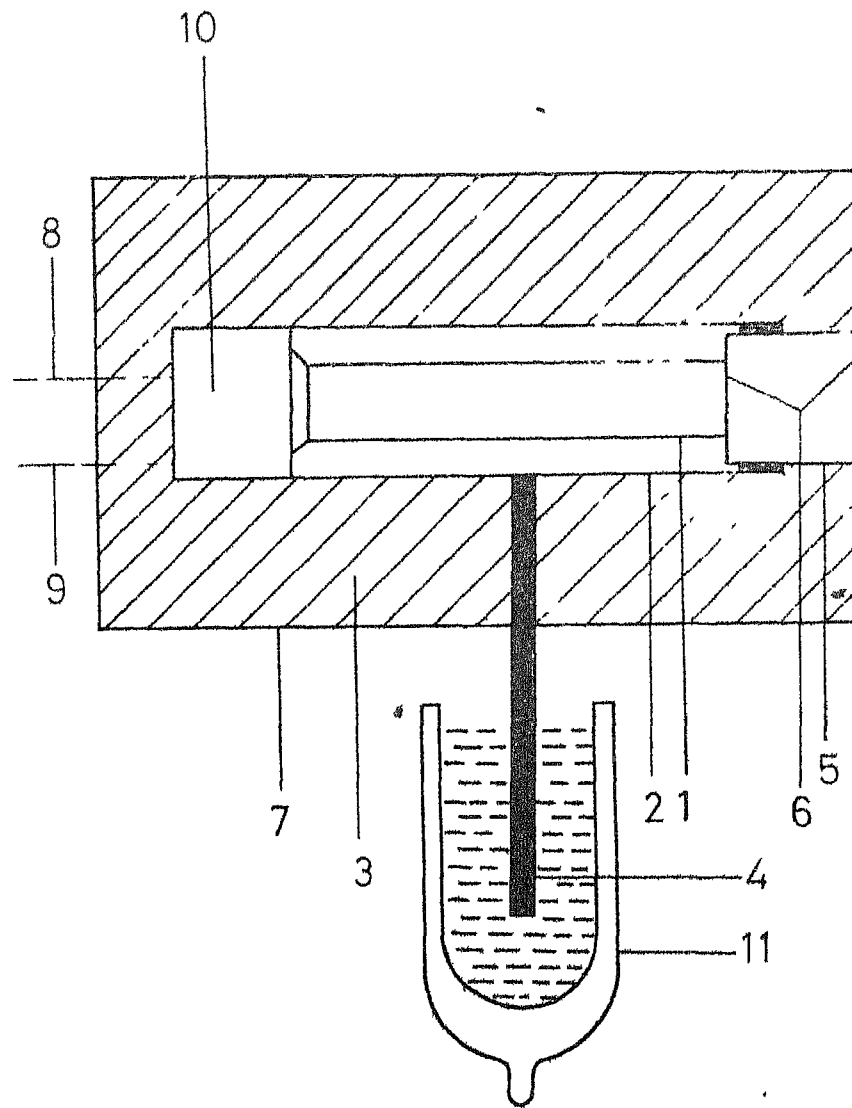
⁺ The potentiometer provided on the D.C. source, to vary the speed continuously between 0 and 3 RPM is replaced by a bandswitch to get reproducible speeds.

discharge tube are recorded with a full width at half maximum (FWHM) of 2.5\AA and this is the lowest achieved. And lines of equal intensity and separated by about 2\AA are just seen as two. At the temperatures at which the experiments are done (LNT,RT) lifetime broadening is the dominant factor determining the line shapes of rare earth spectral lines² and thus all lines are expected to be Lorentzians. No significant deviation from this is observed in the recorded line shapes.

2.1.8 Photomultiplier tubes and cooled housings

The work was initially started using a cooled R.C.A No. 7102 tube. This tube was chosen primarily for its wide SI spectral response extending into the infrared. At the room temperature this tube has a very large dark current and attendant dark current noise largely of thermionic origin. A liquid nitrogen cooled housing is therefore built to reduce this dark current.

The housing uses what can be called conduction cooling and is illustrated in figure 2.6. In this the PMT is surrounded by a thin walled brass tube to which one end of a stout ($3/4"$ dia) copper rod is soldered. The other end of this rod is lowered into a dewar containing liquid nitrogen. The PMT is thus cooled by conduction along the copper rod. The PMT is plugged into a socket fixed on top of a perspex box which houses the resistors of the potential divider chain.



- | | |
|--------------------------|--|
| 1. PMT | 7. Outer Aluminum box |
| 2. Inner brass tube | 8. H V cable |
| 3. Insulating foam | 9. Signal cable |
| 4. Copper rod (3/4" dia) | 10. Potential divider encased in perspex box |
| 5. Evacuated glass cell | 11. Liquid nitrogen dewar |
| 6. Pyrex windows | |

Fig. 2.6 Cooled housing for the RCA No. 7102 photomultiplier.

The sides of this box are firmly glued together with methylene chloride (which forms a bond by dissolving perspex) rather than screwed together. This is done in order to prevent moisture from entering the box through the joints and shorting the resistors. Moisture would also condense on the cool photocathode surface and reduce the amount of light detected, if the cathode surface is allowed to come into direct contact with the atmospheric air. Several techniques to overcome this problem are reported in literature³. Here it is achieved by an evacuated (to 10^{-5} mm of Hg) glass cell with plane parallel quartz windows which is pushed fit (with a few layers of Teflon pipe sealant tape to serve as a gasket) into the brass tube surrounding the PMT (reference to figure). The length of this cell is chosen to be 3" by trial and error. This puts the photocathode at a rather large distance of about 3" from the exit slit but no light is lost because of its large diameter (1.25"). The whole assembly is now placed inside a large Aluminium box and the intervening space is stuffed with StyrofoamTM to provide thermal insulation. The copper rod projects out of a large hole cut in the bottom face of the Aluminum box.

With this arrangement the dark current is reduced from a room temperature value of about 1μ amp (the six tubes tested have dark currents between 1 and 10μ amps) to as low as

1×10^{-11} amps with a cathode voltage of -1000V. From this value it is estimated⁴ that the PMT would have reached a temperature of about -160° C. The dark current noise is quite negligible under these conditions. The initial cool down period of the housing is about 45 minutes after which the operation is quite stable. The liquid nitrogen consumption is about one litre per hour which is rather large.

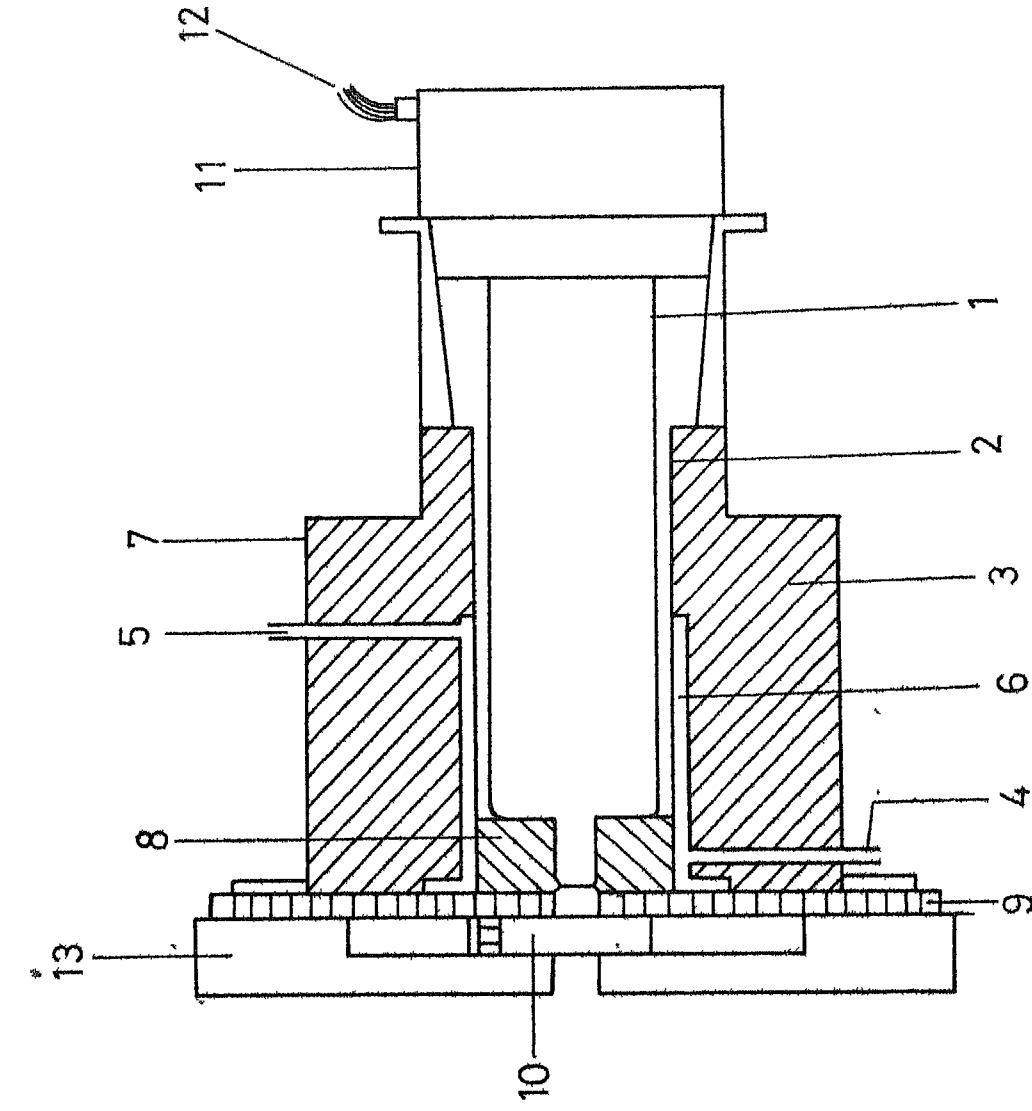
The dark current noise being thus eliminated the more serious limitation of the tube namely the shot noise has become apparent. This noise is surprisingly so excessive in this tube that even with the strongest signals recorded (eg. I.R. fluorescence of $\text{Nd}^{3+}:\text{LaF}_3$, signal strength about 10^{-8} amp at 1000V) the signal to noise ratio was only of the order of ten. Also some major difficulties are encountered in the operation of this housing. The Torr seal used for fixing the windows of the vacuum cell does not withstand repeated thermal cycling and it has become necessary to reseal and reevacuate the cell after every month or two. It is also found that after prolonged use some moisture does seep into the potential divider box and leads to sparking. A remedy for this latter problem is to ^upot the divider chain in some foam or epoxy, impervious to moisture. However, there is reason to believe that both these problems are partly due to the very low temperatures that are reached. Unfortunately there is no way in which this can be

avoided and thus the use of this housing is discontinued in latter work. A new housing has been designed partly eliminating the above difficulties.

This housing is made specifically to accommodate the I.T.T. No. FW130 tube and is illustrated in figure 2.7. In this design the tube is sought to be cooled by circulating cold nitrogen gas through an annular brass chamber surrounding it. The gas is obtained by boiling liquid nitrogen with an immersed heater and the temperature of the tube can be controlled by varying the heater current. Polyurethane foam that is polymerized⁺ 'in-place' provides the thermal insulation.

The FW130 tube has an S20 response. The particular tube used is a variant of the standard version in that, it has a slit shaped photo cathode. This is especially suited for spectroscopic work where the light to be detected is frequently in the form of a slit shaped beam. This configuration obviates the need for a focussing magnet around the photocathode which is sometimes used to reduce the dark current and noise. The magnetic field is used to deflect the 'dark' electrons emitted by the unused portion of the photocathode from reaching the first dynode. This tube has a low dark current of about 1×10^{-8} amp at 1800V and room temperature. The dark current noise is small compared to the intensity of even the weakest lines recorded even at room temperature.

⁺ The chemicals necessary for this polymerization are kindly provided by the U Foam Co., Hyderabad.



1. PMT
2. Inner brass tube
3. Insulating foam (polymerized in place)
4. Cool nitrogen gas inlet
5. Nitrogen gas outlet
6. Gas circulation chamber
7. Outer brass tube
8. Thermally conducting annular ring
9. Bakelite plate
10. Adjustable slit
11. Potential divider case
12. Signal and HV cables
13. Exit slit mounting plate

Fig. 2.7 Cooled housing for the IRT No. PV 190 photomultiplier.

For this reason the tube is operated always at room temperature itself though the housing described is built especially to cool this tube. The shot noise of the tube also is quite small. The signals recorded are usually in the range of 1 n.amp to several microamperes with an applied voltage between 1250V and 1400V.

Because of this exceptional performance, all the subsequent work is done only with this tube. The recordings made with this tube only are reproduced in this thesis as the ones made with the 7102 tube are quite inferior in quality. The sensitivity of the tube falls off steeply after about 8000\AA . Only one group of fluorescence lines is observed in this region namely the R-Z ($^4F_{3/2} - ^4I_{9/2}$) group of Nd^{3+} , but the inherently large intensity of this group compensates somewhat for this poor sensitivity. (The grating efficiency also is small in this region).

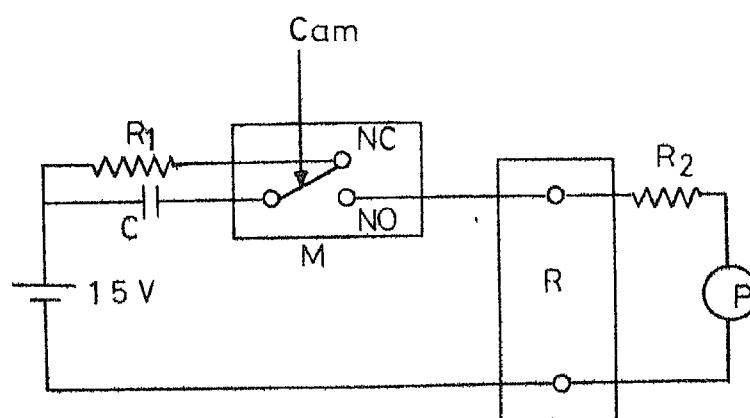
The high voltage required for the tubes is obtained either from an ECIL No. HV204 power supply (300 to 1500V variable, positive or negative) or a -1400V to -2000V variable voltage power supply fabricated in our electronics shop. With a negative voltage power supply the anode is at ground potential which is very convenient for subsequent signal processing.

2.1.9 Electronics

The current from the PMT is measured by a Keithley No. 417 Picoammeter (figure 2.1). This is an electrometer amplifier with a full scale range variable between 10^{-5} amps and 3×10^{-14} amps in a 0.3, 1, 3 sequence. A 0 to 3 sec. variable time constant low pass filter usable in the 10^{-8} amp and lower current ranges provides some noise rejection. There is also a 'current suppress' facility by which the dark current of the tube can be subtracted out. This differs from the ordinary zero suppression in that, it is independent of the current range in which the signal is being measured and is a very convenient feature. The amplifier has a recorder output of 3 volts full scale swing that can be used to drive potentiometric recorders. A Varian No. G.14 strip chart recorder is used to record this voltage. The chart speed is 10 cm/min giving a dispersion on the chart of about 0.4 to 1.6 \AA/mm (1 \AA/mm is generally used).

2.1.10 Wavelength markers and calibration

The schematic of the marker circuit is shown in figure 2.8. A cam attached to the grating drive shaft closes the microswitch [KESBO (India) No. MVR6] contact once every rotation and connects a 1.5V dry cell across the recorder terminals through a capacitor. The capacitor allows only a



M = Microswitch-(Kesba No. MVR-6)
 NC = Normally closed contact
 NO = Normally open contact
 R = Recorder
 P = Picoammeter
 C = $\sim 0.1 \mu\text{F}$
 R₁ = $\sim 10 \text{ K}\Omega$
 R₂ = $\sim 50 \text{ K}\Omega$

Fig. 2.4 Schematic diagram of the wavelength marker circuit.

sharp spike of voltage to go through, essentially at the instant the contact is closed. Without this a broad marker of about 2 to 3 millimetres width would be obtained which is useless. During the off period of the microswitch the capacitor is discharged through the resistor R_1 to make it ready for the next marker. An isolation resistor R_2 inserted in the picoammeter output lead prevents the low output impedance of the picoammeter from shunting off the 1.5V pulse. Since the input impedance of the recorder is as large as one Megohm this series resistance does not reduce the voltage received by the recorder to any significant extent. The values of the capacitor (about $0.1\mu\text{F}$) and the series resistor R_2 are chosen by trial and error to get a marker of distinguishable length (about 1 cm) and without overshoot.

The calibration of the spectrometer thus consists of ascertaining the wavelengths corresponding to these marker positions. This is easily done by recording the spectra of some standard sources that are rich in sharp strong lines. Two Geissler discharge tubes, one filled with Argon and one with a Helium-Neon mixture, as well as an Osram Cesium vapour standard lamp are used for this purpose. Put together these lamps contain more than 200 usable lines distributed over the region of interest that is $4500\text{--}9000\text{\AA}$. The positions of markers⁺ found out in this way are found repeatable to $\pm 1\text{\AA}$.

⁺ The markers are numbered by the grating rotation angle in tenths of a degree. These are indicated in the tracings - numbers like 10.6 etc.

The wavelengths measured on the chart have a further measurement error of about $\pm 0.5\text{\AA}$ (corresponding to 0.5 mm) giving a total inaccuracy of $\pm 1.5\text{\AA}$ for the wavelengths measured. It needs be pointed out here that relative separations of lines within a single group (of say 100\AA extent) are subject only to this second error of $\pm 0.5\text{\AA}$. Usually each spectral line is recorded several times, under different polarizations, crystal orientations, gain etc., and the wavelength is taken as the average of the values measured from all the recordings. It is found that these numbers rarely differ from each other by more than 1\AA and the R.M.S. deviation (of 5 to 10 readings) is not more than 0.5\AA .

2.1.11 Sensitivity test

The Raman spectrum of Benzene at R.T. is recorded to get an idea of the sensitivity of the spectrometer. Figures 2.9 and 2.10 illustrate this spectrum recorded with 20 mw and 500 mw of laser power (4880\AA) respectively. It could be seen from figure 2.9 that the two strong lines of Benzene at 992 and 3062 cm^{-1} could be recorded with adequate S/N even with 20 mw of power.

2.2 Spectrophotometer used at Santa Barbara

Some preliminary work on the fluorescence spectra of $\text{Nd}^{3+}:\text{LaF}_3$ and $\text{Eu}^{3+}:\text{LaF}_3$ in some crystal orientations using

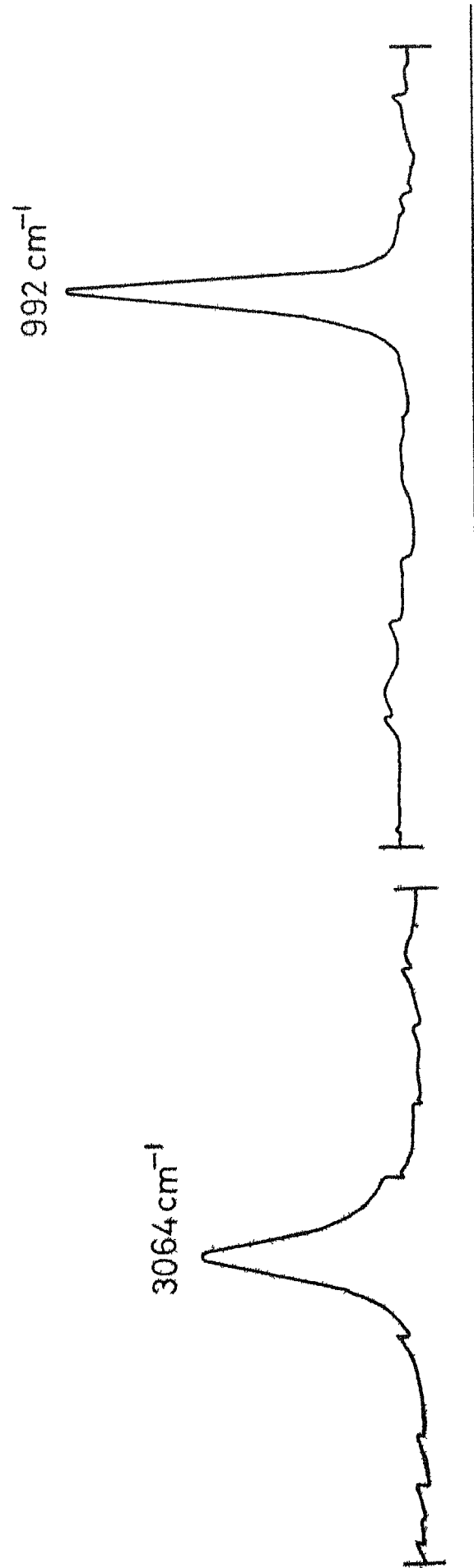


Fig. 2.9 Raman spectrum of Benzene: 4880\AA , 20 mW .

HT voltage 1200V , Slits 100\AA , 100\AA , Sensitivity $1 \times 10^{-2}\text{ amp}$.

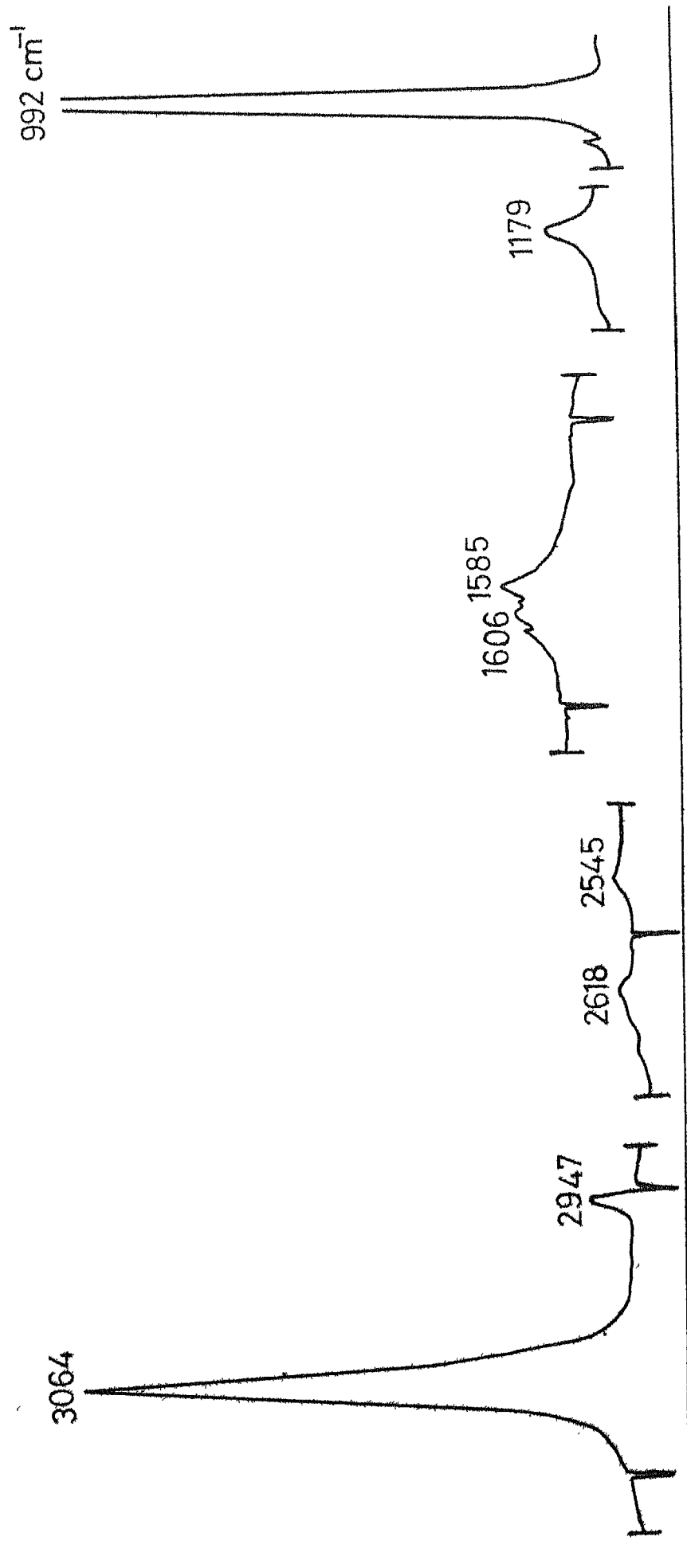


Fig. 2.10 Raman spectrum of Benzene: 4330\AA , 500 mW.

HEE voltage 1200V. Slits 100 μ , 100 μ . Sensitivity $1 = 10^{-3}$ cps.

Ar⁺ laser excitation was done by Professor P. Venkateswarlu in association with Dr. J.J. Kim in the University of California at Santa Barbara. These spectra are recorded on a Spex No. 1400 double monochromator using Coherent Radiation No. 52 Argon ion laser. The PMT used is an EMI No. 9558. The spectra recorded by the author here on the set up described compare quite favourably with those spectra in terms of S/N as well as wavelength accuracy. The double monochromator gives superior performance however in case of lines lying close to the exciting laser line because of the much smaller scattering inherent in such a system. The (E-Z) group of Nd³⁺ in the region 5170-5300Å is an example of this. All the recordings reproduced in this thesis except this above mentioned one, are those made by the author on the set-up assembled here.

2.3 Experimental arrangement with the nitrogen laser excitation

The N₂ laser used was built in our laboratory by Mr. H. Jagannath and Dr. G. Chakrapani. The laser operates in a plane wave excited mode, achieved by placing the nitrogen plasma tube across a laminated sheet transmission line etched in a parabolic shape. The exciting voltage pulse of 16 to 20 KV is applied at the focus of the parabola by a spark gap. The laser pulse generated has a width of about 7.5 ns. The peak power is estimated to be between 100kW and

1 MW. At the time these experiments are made it was operating in a self quench mode, at a frequency of about 20 pulses per sec. A detailed description of the laser is given in a technical report⁺ prepared in the laboratory .

The cross section of the laser beam is a rectangle approximately $4 \times 10 \text{ mm}^2$. The beam is bent upwards by a front coated Aluminum mirror and is focussed into the crystal by a quartz lens of 1" focal length. The fluorescence is collected in a horizontal direction by a condensing lens chosen to suit the particular spectrograph used. The Carl-Zeiss Q24 medium quartz spectrograph was used for work in the ultraviolet region and the Carl-Zeiss three prism spectrograph in the visible and infrared. The exposure times ranged between 30 mts and one hour with the Q24 and between 1 hour and 6 hours with the three prism instrument. The plate factor of these plates ranges between 30 and $200\text{\AA}/\text{mm}$. The principle inaccuracy in the wavelengths measured from these plates is due to the 30μ slitwidth used.

2.4 The optical absorption set up

The optical absorption spectra are recorded photographically on a Jarrell-Ash 3.4 metre Ebert grating spectrograph. Interchangeable gratings with 15,000 and 30,000 L.P.I. are used. The first order dispersion of $5\text{\AA}/\text{mm}$ and $2.5\text{\AA}/\text{mm}$ provided by these gratings respectively proved adequate for

⁺ In press

the spectra recorded. Higher orders are suppressed by the use of various glass filters of the Corning CS series.

A 750W Tungsten (projector) lamp is used in the visible region and a Carl-Zeiss No. H₂-0.3 Hydrogen lamp for work in the ultra violet. The exposure times with the tungsten lamp ranged between 30 sec and 5 minutes. The Hydrogen lamp however required exposures of upto 30 minutes duration. The spectra are recorded on Kodak 103a-N,0 and F plates of 25 x 5 cm² dimensions in their respective regions of sensitivity.

Iron arc is used as the standard and the plates are mostly measured on Carl-Zeiss Model B Abbe comparator which has a least count of 1 μ . Positions of some broad lines whose centres could not be located on the comparator are measured using a Carl-Zeiss Model III microdensitometer. This has a least count of 10 μ .

The inaccuracy in the measured wavelengths of sharp lines (Eu³⁺:LaF₃) is mainly due to the slitwidth used. At a dispersion of 2.5 \AA /mm the used slitwidth of 50 μ corresponds to 0.125 \AA . At 5000 \AA this is equal to 0.5 cm⁻¹. The absorption spectrum of Nd³⁺:LaF₃ on the other hand consists of many overabsorbed lines and the error in their measurement is due to errors in locating the line centres. Even from microdensitometer traces these could not be located to better than 1 \AA and this is the limiting error.

REFERENCES

1. Amnon Yariv, Introduction to Quantum Electronics.
(Holt, Reinhart and Winston Inc. 1971).
2. W.M. Yen, W.C. Scott and A.L. Schawlow, Phys. Rev.
136, A271 (1964).
3. Sharadanand, Rev. Sci. Instrum. 43, 641 (1972).
G.W. Carribeau, J. Phys. E. 3, 929 (1970)
F.L. Lipsett, Rev. Sci. Instrum. 38, 278 (1967); and
references given there.
4. EMI Photomultiplier tubes brochure reference
No. P001/fP70.

CHAPTER 3

OPTICAL ABSORPTION AND FLUORESCENCE
SPECTRA OF $\text{Eu}^{3+}:\text{LaF}_3$ AT LNTABSTRACT

The optical absorption and fluorescence spectra of $0.5\%\text{Eu}^{3+}:\text{LaF}_3$ are observed in the region $4500\text{--}9000\text{\AA}$. Only three lines due to $^5\text{D}_2$ and three lines due to $^5\text{D}_1$ are observed in absorption. The fluorescence excited by the Argon ion laser consists in all, of twelve groups of transitions from $^5\text{D}_{0,1,2}$ to the levels $^7\text{F}_{0,1,2,3,4,5}$ of the ^7F ground multiplet. No transitions to $^7\text{F}_6$ are found. The availability in the Ar^+ laser of several excitation wavelengths was of some help in identifying the upper levels of fluorescence. Using the fluorescence data, positions of all the Stark components of $^5\text{D}_{0,1,2}$ and $^7\text{F}_{1,4}$ levels are determined. Only three levels of $^7\text{F}_2$ (of the expected five) are determined, as fluorescence

to other levels is not observed, while the identification of the Stark components of 7F_3 and 7F_5 was hampered by a multitude of overlapping transitions. Attempts to determine the positions of levels of 7F multiplet by infrared absorption did not bear fruit. LaF_3 has a hexagonal unit cell and the R.E. ions are known to replace the La ions substitutionally at sites of orthorhombic symmetry. The polarizations of the lines indicate a C_{2v} site symmetry, but with some deviations which indicate a distortion towards C_s . However, a consistent set of symmetry species assignments could be made to all the observed levels under the classification of a C_{2v} symmetry.

Exciting this crystal with a nitrogen laser resulted only in continuum fluorescence in the blue, most likely due to Eu^{2+} .

3.1 Introduction

Europium is the seventh element in the Lanthanide series and in the trivalent state, has six electrons in the 4f valence shell. The low lying levels of this $4f^6$ configuration have been fairly well established by several past studies¹⁻⁴. The intermediate coupling calculations made by Ofelt² incorporating the septet-quintet-triplet interactions have lead to a positive identification of several levels observed below $40,000 \text{ cm}^{-1}$ in $\text{Eu}^{3+}:\text{LaCl}_3$. The level structure is particularly simple below $24,000 \text{ cm}^{-1}$. In this region are contained the regular ^7F ground multiplet ($0-5000 \text{ cm}^{-1}$) and four levels $^5\text{D}_{0,1,2,3}$ of the ^5D multiplet between $17,000$ and $24,000 \text{ cm}^{-1}$. The energy level diagram

is given in figure 3.1. Above $24,000\text{ cm}^{-1}$ occur several levels belonging to different terms and the region is very crowded. Identification of many of these levels is due to Ofelt².

$\text{Eu}^{3+}:\text{LaF}_3$ was investigated earlier by Weber⁵ who studied the lifetimes of $^5\text{D}_{0,1,2,3}$ levels as functions of Europium concentration and temperature. However only a few details of the spectrum as such were reported, from which it is not possible to establish the energy level structure.

In this work aimed at obtaining this information, the optical absorption spectrum and the laser excited fluorescence spectrum of $\text{Eu}^{3+}:\text{LaF}_3$ are recorded in the visible. From these spectra most of the Stark components of the levels of ^5D and ^7F multiplets below $22,000\text{ cm}^{-1}$ are determined. A site symmetry of C_{2v} is found to be a fairly good approximation to the site symmetry of the rare earth ion and all the observed Stark components are classified according to the species of this symmetry group.

3.2 Crystal structure of LaF_3 and selection rules

The crystal structure of LaF_3 has been a subject of discussion for a long time. Neutron scattering studies⁶ have determined the unit cell to be hexagonal and hexamolecular, and belonging to the space group O_{6v}^3 . The Lanthanum

ions are determined to be lying in two planes, forming equilateral triangles rotated by 60° about the crystalline symmetry axis (c axis) with respect to each other and with a separation of $c/2$ between them. The E.P.R. measurements⁷ on a number of rare earth ions (Nd, Ce, Er, Dy and Yb) doped in LaF_3 indicate a site symmetry of C_s for the rare earth ion, the reflection plane being a plane containing the R.E. ion and the c axis. This is in conformity with a unit cell of C_{6v}^3 symmetry. However two structures which are more symmetric, viz D_{6h}^3 and D_{3d}^4 have been proposed on the basis of X-ray measurements^{8,9}

Differences of the order of 0.1\AA in the co-ordinates of the various ions distinguish these three structures from each other. The site symmetry of Lanthanum is C_{2v} and C_2 respectively in the two latter structures. The C_2 axis is perpendicular to the c axis and in case of C_{2v} , one of the reflection planes is perpendicular to the c axis, and the other contains it,

The studies on the Raman spectra¹⁰ are consistent with a D_{3d}^4 structure, but only small deviations from the more symmetric D_{6h}^3 structure are observed. The optical spectrum of $\text{Pr}^{3+}:\text{LaF}_3$ ¹¹ exhibits polarization and selection rules compatible with C_{2v} site symmetry with only a few deviations. A site symmetry of C_{2v} was derived for the Gd^{3+} from the E.P.R.

measurements of Gd^{3+} doped in several rare earth trifluorides isomorphous with LaF_3 ¹². It was however considered to be indicative only of local adjustments of the ligands around the spherically symmetric Gd^{3+} rather than a space group higher than C_{6v}^3 for the crystal as a whole. In any case the Raman and optical studies cited above indicate that a site symmetry of C_{2v} compatible with a D_{6h}^3 structure is not far from the reality and is atleast a very good approximation.

The observations on the optical spectra of Kramers ions doped in this lattice (Nd^{13} , Dy^{14} , Sm^{15} and Er^{16}) present however a more intriguing problem in that, the spectra are partially polarized. None of the orthorhombic (C_{2v} , C_2 , C_s) symmetry groups contain more than one double valued representation. So under any of these symmetries all the Kramers' wavefunctions belong to a single species and no selection rules exist nor should there be any polarization. The polarization of the lines does not conform also to the pattern expected for a D_{3h} site symmetry which the R.E. ions possess in the highly symmetric D_{6h}^4 unit cell proposed by Schlyter¹⁷. Some explanations are offered for this discrepancy by earlier workers¹⁴ but no conclusions could be reached at. This aspect is discussed in a greater detail in section 4.7.

The selection rules for the symmetry groups C_{2v} and C_s are given in Tables 3.1 and 3.2. Since the quantization axis of the R.E. site is perpendicular to the symmetry axis of the crystals a right handed co-ordinate system illustrated in figure 3.2 is used in deriving these tables. The ionic co-ordinate system XYZ is so oriented that the X and Z axis lie in a plane perpendicular to the c axis and the Y axis coincides with it. The horizontal plane being a symmetry plane the X and Z axis are indistinguishable. The only recognizable axis is Y, parallel to the c axis. Thus in Tables 3.1 and 3.2, σ and π refer to the electric vector perpendicular and parallel respectively to the c axis and not to the ionic Z axis. This degeneracy of the X and Z axis leads to an ambiguity in the species assignment (under C_{2v}) of the relevant levels, if based only on the polarization of the transition between them. Specifically it is not possible to distinguish strictly between A_1 and B_1 or between A_2 and B_2 . However in the present case where several transitions involving a particular level are observed, the information from all these are put together and with the a priori information of the kind that $J=0$ level is an A_1 (not a B_1), unique species assignments are arrived at for most of the levels. The next section describes the observed spectrum and its analysis.

Table 3.1

Selection rules for C_{2v} sites in the D_{6h}^3 structure of LaF_3

a. Electric Dipole						b. Magnetic Dipole					
	A_1	A_2	B_1	B_2	E'		A_1	A_2	B_1	B_2	E'
A_1	σ		σ	π		A_1		π	σ	π	
A_2		σ	π	σ		A_2	π		π	σ	
B_1	σ	π	σ			B_1	σ	π		π	
B_2	π	σ		σ		B_2	π	σ	π		
E'					$\sigma\pi$	E'					$\sigma\pi$

E' is the double valued representation

π Electric vector parallel to C axis

σ Electric vector perpendicular to C axis

Table 3.2

Selection rules for C_s sites in the C_{6v}^3 structure of LaF_3

a. Electric Dipole			b. Magnetic Dipole				
	A'	A''	E'		A'	A''	E'
A'	$\sigma\pi$	σ		A'	π	$\sigma\pi$	
A''	σ	$\sigma\pi$		A''	$\sigma\pi$	π	
E'			$\sigma\pi$	E'			$\sigma\pi$

E' is the double valued representation

σ and π have the same meaning as in Table 3.1

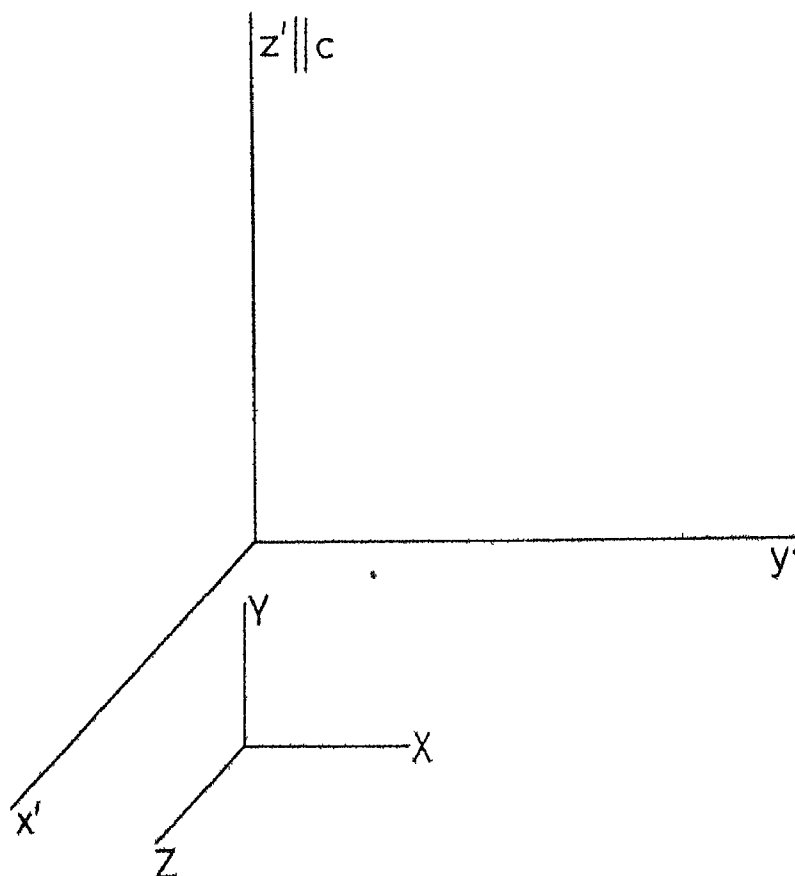


Fig. 3.2 Orientation of the ionic co-ordinate axes (XYZ) with respect to the crystalline co-ordinate axes ($X'Y'Z'$).

LIBRARY
CENTRAL LIBRARY
Acc. No. 51158

Table 3.3

Correlation table for C_{2v} and $C_s(YZ)$ groups

Species under C_{2v}	Species under $C_s(YZ)$
A_1	A'
A_2	A''
B_1	A''
B_2	A'

3.3 The absorption and fluorescence spectra at LNT

3.3.1 General features

A single crystal of LaF_3 containing 0.5 %Europium purchased from the Optovac Co. (USA) was kindly loaned to us by Professor H.P. Broida. The crystal is of very good optical quality and measures $10 \times 7 \times 4 \text{ mm}^3$ with the c axis specified to be parallel to the shortest side (4mm). This is checked by viewing it under a polarization microscope. The crystal contains beside Europium, an unknown but small quantity of Praseodymium as an unintentional co-dopant.

The absorption spectrum at LNT recorded in the range 4000-9000Å consists of only two groups of sharp and weak lines⁺ around 4640Å and 5240Å. By comparison with the spectra of Eu^{3+} in other lattices¹⁻⁴ these lines are easily identified as due to the $^7\text{F}_0-^5\text{D}_2$ and $^7\text{F}_0-^5\text{D}_1$ transitions. The $^7\text{F}_0-^5\text{D}_3$ (expected at about 4100Å) is not observed, as well as the $^7\text{F}_0-^5\text{D}_0$. The latter is forbidden by both electric dipole and magnetic dipole selection rules but is seen to become allowed⁴ due to J mixing. Weber⁵ reports observing this transition at 5830Å in the excitation spectrum of $^5\text{D}_0$ fluorescence.

Weber also mentions observing the infrared absorption due to the transitions within the ^7F multiplet but did not give any details. Efforts to observe this here on a Perkin-

⁺ The lines are very weak. No satisfactory print could be obtained and therefore the figure is not presented.

the two namely; $^5D_0-^7F_3$, $^5D_1-^7F_5$ (6600\AA) and $^5D_0-^7F_2$, $^5D_1-^7F_4$ (6100\AA). This is however not possible with the crystal used, as excitations capable of populating 5D_2 also lead to strong fluorescence from the Pr^{3+} in both these regions and masks the Europium fluorescence. The observed fluorescence at LNT are listed in Table 3.4. The excitations used are 4580\AA (for 5D_2) and 5145\AA (for 5D_1 and 5D_0) throughout⁺, as the other excitations give much weaker fluorescence

In the spectrum recorded at RT the lines show width larger by factors of two or three than at LNT. This is not very large per(se) but still large enough to obscure several fine details and small splittings, limiting the usefulness of the spectrum. Also the intensity is about three times smaller at R.T. The discussion is therefore limited to the spectrum observed at LNT only.

The elucidation of the energy level structure being the main task of the analysis, in what follows, the various transitions terminating in a particular 7F_J level are discussed together. In the discussion the totality of transitions between a particular 5D_J level and a 7F_J level is referred to as a 'group' and the superscripts 5 and 7 are omitted for brevity. For example the group of six lines identified as transitions between 5D_1 and 7F_1 levels is referred to as the D_1-F_1 group. The word 'transition' is

⁺ Excitation with the 3371\AA emission of the nitrogen laser resulted only in some continuum fluorescence in the blue, attributable to Eu^{2+} . An EPR spectrum characteristic of Eu^{2+} is also observed in this crystal.

however used to denote a single transition between any two Stark components. A notation is also introduced to denote the individual Stark components as follows. The Stark levels of say, the 5D_1 are denoted as $D1,1$; $D1,2$ and $D1,3$ in order of increasing energy. In Dieke's notation these would be called B_1 , B_2 and B_3 respectively. This notation would lead to a clash with the C_{2v} species notation (A_1 , A_2 , B_1 , B_2) and for this reason is not used here. Stark components of 7F_4 for example are similarly denoted $F4,1$; $F4,2$; ... $F4,9$. The transition assignments shown in Table 3.4 use this notation only. The word 'level' is primarily used to denote an SLJ level (5D_1 say) but it is also sometimes used to denote individual Stark components. Care is however taken to avoid confusion due to this double usage by making the context clear.

3.3.2 Transitions involving the 7F_0 ground state

These are observed in absorption as well as fluorescence. The absorption lines are given in Table 3.5. The fluorescence spectrum is illustrated in figures 3.3 and 3.4. The numbers marked in the figures under the various fluorescence lines are the wavelengths in Angstrom units. Three transitions are observed between F_0 and D_1 in both cases. Two of these are π polarized and the other σ . The axial spectrum

Table 3.4

The fluorescence spectrum of $\text{Eu}^{3+}:\text{LaF}_3$ at LNT

π	E Vector parallel to C axis.
and σ	E Vector perpendicular to C axis, direction of viewing perpendicular to C axis
a	Observed while viewing along the C axis.
E,e	Strong, weak electric dipole transitions.
M,m	Strong, weak magnetic dipole transitions.
*	The partial polarization of the line can be explained under C_s symmetry only
+	The partial polarization of the line cannot be explained even under C_s symmetry.

Wavelength Å	Energy (cm^{-1})	Polarization		Transition	Nature
		Strong	Weak		
4635.8	21565	σa		D2,5 — FO*	E
4641.0	21541	σa		D2,4 — FO	E
4643.0	21532	π		D2,3 — FO	E
4647.7	21509.7	σa		D2,2 — FO	E
4658.0	21462			D2,1 — IO Raman, 4580Å	excitation
4663.0	21439			" "	
4704.6	21250	$\pi \sigma a$		D2,5 — F1,1*	E
4711.0	21221	$\pi \sigma a$		D2,3 — F1,1*	E
4717.8	21191.5	$\pi \sigma$	a	D2,5 — F1,2*	E,m
				D2,1 — F1,1	E,m
4724.3	21161	πa		D2,3 — F1,2	M
4727.2	21148	σ		D2,5 — F1,3	M
4729.6	21138	σ		D2,2 — F1,2	M
4731.0	21131	π	a	D2,4 — F1,3	E,m
4739.8	21092	$\sigma \pi a$		D2,1 — F1,3*	M

Table 3.4 (cont.)

Wavelength Å	Energy (cm ⁻¹)	Polarization		Transition	Nature
		Strong	Weak		
5070.5	19716	π	σ_a	$5D_2 \longrightarrow 7F_3$	
5076.9	19692	$\pi\sigma_a$		"	
5079.2	19683	πa		"	
5083.4	19666	πa	σ	"	
5085.2	19659	$\pi\sigma_a$		"	
5088.5	19647	σ	πa	"	
5091.0	19637	$\pi\sigma_a$		"	
5097.2	19613	σ	πa	"	
5103.1	19591	$\pi\sigma$		"	
5110.6	19562	σ		"	
5116.7	19538	π		"	
5124.5	19509	$\pi\sigma_a$		"	
5222.0	19144			Raman, 5145Å	excitation
5227.6	19124			" "	
5244.0	19063	σ		$D_{1,3} \longrightarrow F_0$	M
5246.2	19056	πa		$D_{1,2} \longrightarrow F_0$	M
5249.7	19043	πa		$D_{1,1} \longrightarrow F_0$	M
5284.0	18920	σ_a	π	$5D_2 \longrightarrow 7F_4 ?$	E
5287.0	18909	σ_a	π	" "	E
5293.0	18888	π	σ	" "	E
5332.8	18747	$\pi\sigma_a$		$D_{1,3} \longrightarrow F_{1,1}$	E
				$D_{1,2} \longrightarrow F_{1,1}$	E
5337.6	18730	σ_a		$D_{1,1} \longrightarrow F_{1,1}$	E
5349.5	18688	σ_a		$D_{1,3} \longrightarrow F_{1,2}$	E
5355.2	18668	π	σ_a	$D_{1,1} \longrightarrow F_{1,2}^*$	E
5363.2	18640	σ_a		$D_{1,2} \longrightarrow F_{1,3}$	E
5366.5	18629	σ_a		$D_{1,1} \longrightarrow F_{1,3}$	E

Table 3.4 (cont.)

Wavelength Å	Energy (cm ⁻¹)	Polarization		Transition	Nature
		Strong	Weak		
5523.6	18099	σ	πa	D1,3 — F2,1*	M
5529.6	18080	πa		D1,1 — F2,1	M
5533.2	18068	σ		D1,3 — F2,2	M
5535.5	18060	πa		D1,2 — F2,2	M
5540.3	18045	πa		D1,1 — F2,2	M
5564.2	17967	πa		D1,3 — F2,3	M
5571.6	17943	σ		D1,1 — F2,3*	M
5619.5	17790	π	σa	$5D_2$ — $7F_5$	E
5627.0	17767	$\pi \sigma a$		"	E
5631.0	17754	σa		"	E
5633.2	17747	σa		"	E
5635.0	17741	π		"	E
5640.5	17724	σa		"	E
5642.0	17719	π		"	E
5651.0	17691	$\pi \sigma a$		"	E
5675.0	17616	σa	?	"	E
5680.5	17599	σa	?	"	E
5684.0	17588	σa	?	"	E
5690.5	17568	π	σa	"	E
5704.5	17525	$\pi \sigma a$		"	E
5713.5	17498	π		"	E
5721.5	17473	σa		"	E
5805.8	17219	σa		D1,3 — F3,1	E
5812.5	17200	π		D1,1 — F3,1	E
5814.0	17195	σa		D1,3 — F3,2	E
5816.0	17189	π		D1,2 — F3,2	E

Table 3 4 (cont.)

Wavelength Å	Energy (cm ⁻¹)	Polarization		Transition	Nature
		Strong	Weak		
5819.9	17178	π		D1,3 — F3,3	E
				D1,3 — F3,4	E
5821.3	17174	σ_a		D1,2 — F3,3	E
5827.7	17155	π		D1,3 — F3,5	E
		σ_a		D1,1 — F3,4	E
5829.7	17148	σ_a		D1,2 — F3,5	E
5859.3	17062	σ_a		D1,2 — F3,6	E
5865.1	17045	?		D1,1 — F3,6	E
5888.0	16978	π_a		D0 — F1,1	M
5908.8	16918	π_a		D0 — F1,2	M
5922.1	16881	σ		D0 — F1,3	M
6078.3	16447	σ_a		D1,3 — F4,1	E
6085.3	16428	π		D1,1 — F4,1	E
6123.5	16326	σ_a		D0 — F2,1	E
6136.5	16291	π		D0 — F2,2*	E
6143.5	16273	$\pi \sigma_a$		D1,3 — F4,2 ⁺	E
6165.9	16213	π		D1,2 — F4,3	E
6175.1	16189	σ_a		D1,3 — F4,5	E
6182.1	16171	$\pi \sigma_a$		D1,1 — F4,5 ⁺	E
				D1,3 — F4,6 ⁺	
6186.0	16161	π		D1,2 — F4,6	E
6197.9	16129	σ_a		D1,2 — F4,7	E
6201.0	16121	σ_a		D1,1 — F4,7	E
6241.5	16017	σ_a		D1,3 — F4,8	E
6250.0	15995	π		D1,1 — F4,8	E
				D1,3 — F4,9	
6257.8	15975	σ_a		D1,1 — F4,9	E

Table 3 4 (cont.)

Wavelength λ Å	Energy (cm^{-1})	Polarization		Transition	Nature
		Strong	Weak		
6482.1	15423			$5D_0 \text{ --- } 7F_3$	
6490.3	15403			"	
6493.6	15395			"	
6499.7	15381			"	
6543.0	15279			$5D_1 \text{ --- } 7F_5$	
6551.0	15260			"	
6561.5	15236			"	E
6570.5	15215			"	E
6618.6	15104			"	E
6641.6	15052			"	E
6646.0	15042			"	E
6659.4	15012			"	E
6667.4	14993			"	E
6675.5	14976			"	E
6685.5	14953			"	E
6809.5	14681	$\pi\sigma_a$		$DO \text{ --- } F4,1^*$	E
6891.8	14505	σ_a		$DO \text{ --- } F4,2$	E
6919.8	14446	σ_a		$DO \text{ --- } F4,4$	E
6932.2	14421	π		$DO \text{ --- } F4,5$	E
6959.4	14364	π		$DO \text{ --- } F4,7$	E
7017.6	14246	σ_a		$DO \text{ --- } F4,8$	E

Table 3.5

The absorption spectrum of $\text{Eu}^{3+} \cdot \text{LaF}_3$ at LT

Wavelength Å	Energy cm^{-1}	Polarization
4642.95	21532.0	π
4647.2	21512.3	σa
4648.26	21507.4	σa
5244.36	19062.8	σ
5246.19	19056.1	πa
5249.69	19043.4	πa

Note: All the six lines are sharp and weak.

Excitation 4580 \AA , 60 mw
 Input slit width 100μ
 Range 3 namp

63

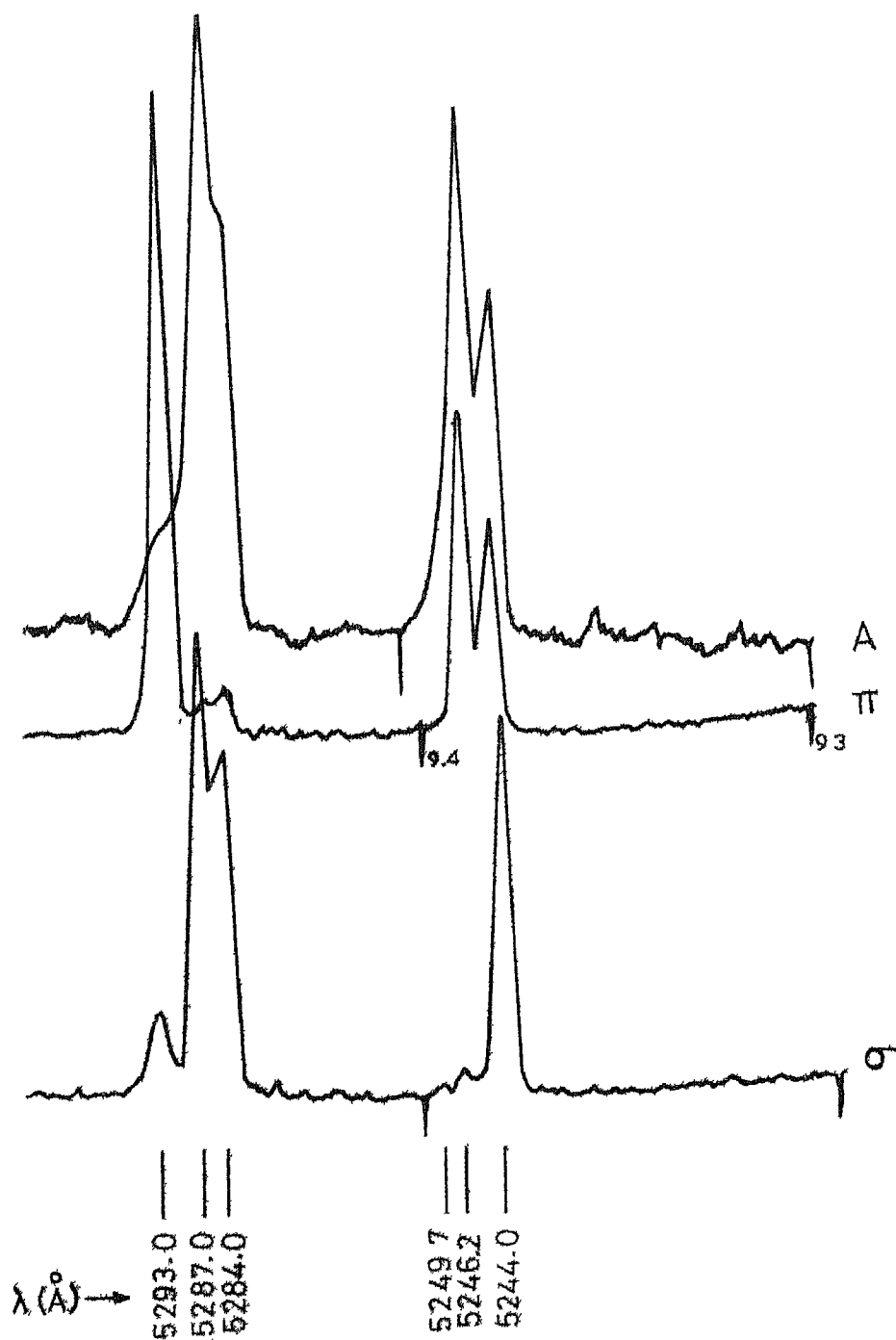


Fig. 3.3 $\text{Er}^{3+}:\text{LaF}_3$ fluorescence at 77°K , $^5\text{D}_1 - ^7\text{F}_0$ group.
 (The three lines at 5284.0, 5287.0 and 5293.0 \AA
 are unresolved).

Excitation 4880Å, 60 mw
 Input slit width 100 μ
 Range 30 n amps

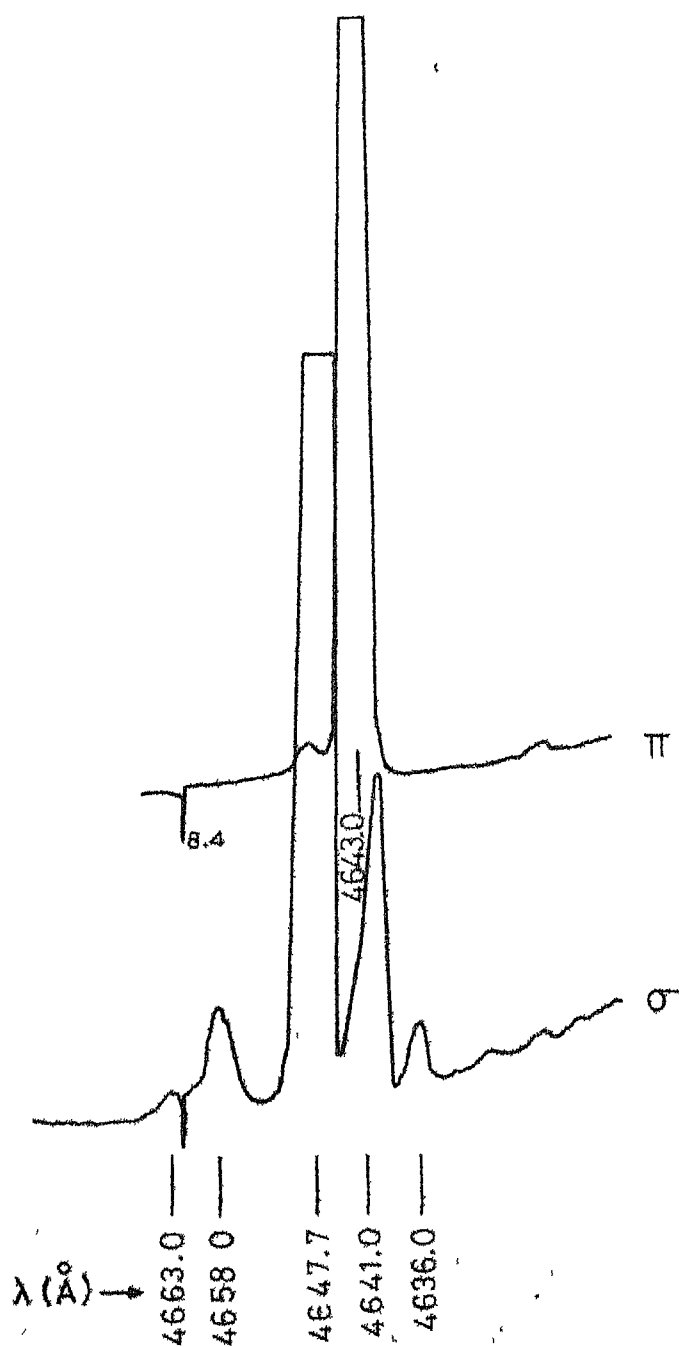


Fig. 3.4 $\text{Mn}^{3+}:\text{LaP}_3$ fluorescence at 77°K, $^5\text{D}_2 \rightarrow ^7\text{F}_0$ group.

is identical to the π spectrum. Thus these are magnetic dipole (MD) transitions. The ED transitions between these levels are actually forbidden by the zero to odd selection rule given by Ofelt¹⁸. The mixing of 7F and 5D wavefunctions² by the off-diagonal elements of the spin orbit coupling (chapter 1) is responsible for allowing these MD transitions. The splitting of 5D_1 is $A_2 + B_1 + B_2$ under C_{2v} and $A' + A''$ under C_s (Table 3.6). From the selection rules of these groups (Tables 3.1b, 3.2b) it is seen that the observed polarizations check only with C_{2v} . The two π lines are due to Stark components of A_2 or B_2 species whereas the σ line is due to a component of B_1 species. Thus the splitting of the 5D_1 is $D1,1-19043.4 \text{ cm}^{-1}$ (A_2), $D1,2-19056.1 \text{ cm}^{-1}$ (B_2) and $D1,3-19062.8 \text{ cm}^{-1}$ (B_1).

The F_0-D_2 group contains two σ lines and one π line in absorption (Table 3.5). In fluorescence the two σ lines at 4647.2\AA and 4648.3\AA are not resolved. Also two more weak lines are observed in σ polarization. The axial spectrum is identical to the σ spectrum confirming the electric dipole (ED) nature of the group. Actually $\Delta J = 2$ for this group and no MD transitions are allowed[†]. Under C_{2v} three σ lines and one π line are expected, the ED transition to A_2 being forbidden (Table 3.1a). However as the symmetry descends to C_s this transition ($A'-A''$) becomes allowed in

[†] For all such cases where $\Delta J=2$ or larger, the axial spectrum is invariably found to be similar to the σ spectrum and since there is no possibility of doubt the axial spectrum is not shown in the figures.

Table 3.6

Splitting of the various J states under C_{2v} and C_s symmetries

J	C_{2v}	C_s
0	A_1	A'
1	$A_2 + B_1 + B_2$	$A' + 2A''$
2	$2A_1 + A_2 + B_1 + B_2$	$3A' + 2A''$
3	$A_1 + 2A_2 + 2B_1 + 2B_2$	$3A' + 4A''$
4	$3A_1 + 2A_2 + 2B_1 + 2B_2$	$5A' + 4A''$
5	$2A_1 + 3A_2 + 3B_1 + 3B_2$	$5A' + 6A''$
6	$4A_1 + 3A_2 + 3B_1 + 3B_2$	$7A' + 6A''$

σ polarization (Table 3.2a). The weakest of the four σ lines is therefore attributed to a Stark component of A_2 species⁺. The other three σ lines are due to components of A_1 or B_1 species, the π line from that of B_2 species. Thus the splitting of the 5D_1 is D2,1-21507.4 cm^{-1} (A_1 or B_1); D2,2-21512.3 cm^{-1} (A_1 or B_1); D2,3-21532 (B_2); D2,4-21541 cm^{-1} (A_1 or B_1) and D2,5-21565 cm^{-1} (A_2). These assignments are somewhat tentative at this stage and have to be confirmed by the analysis of other groups.

3.3.3 Fluorescence terminating in 7F_1

This level is expected around 350 cm^{-1} and the groups of lines around 5900Å, 5350Å, and 4700Å are easily identified as the D_0-F_1 , D_1-F_1 and D_2-F_1 groups. All these three groups are shown in figure 3.5. MD transitions to F_1 are allowed from all the three fluorescing levels, whereas ED transitions are allowed only from D_2 and D_1 . ED transitions from D_0 are forbidden by the zero to odd selection rule. Figure 3.5 shows that the character of the D_0-F_1 group in MD, and that of the D_2-F_1 is mixed. The D_1-F_1 group however does not show any MD transitions. The reason may very well be the same as advanced by Judd³ to explain their absence in the spectrum of Europium ethyl sulphate, namely the accidental vanishing of the MD matrix element due to the coincidence of the g factors of 7F_1 and 5D_1 .

⁺ It is checked that none of these lines is a Raman line.

Excitation 5145 Å, 400 mw
 Input slit width 100 μ
 Range 10 n amp
 $5D_0-7F_1$

4580 Å, 60 mw
 100 μ
 3 n amp
 $5D_2-7F_1$

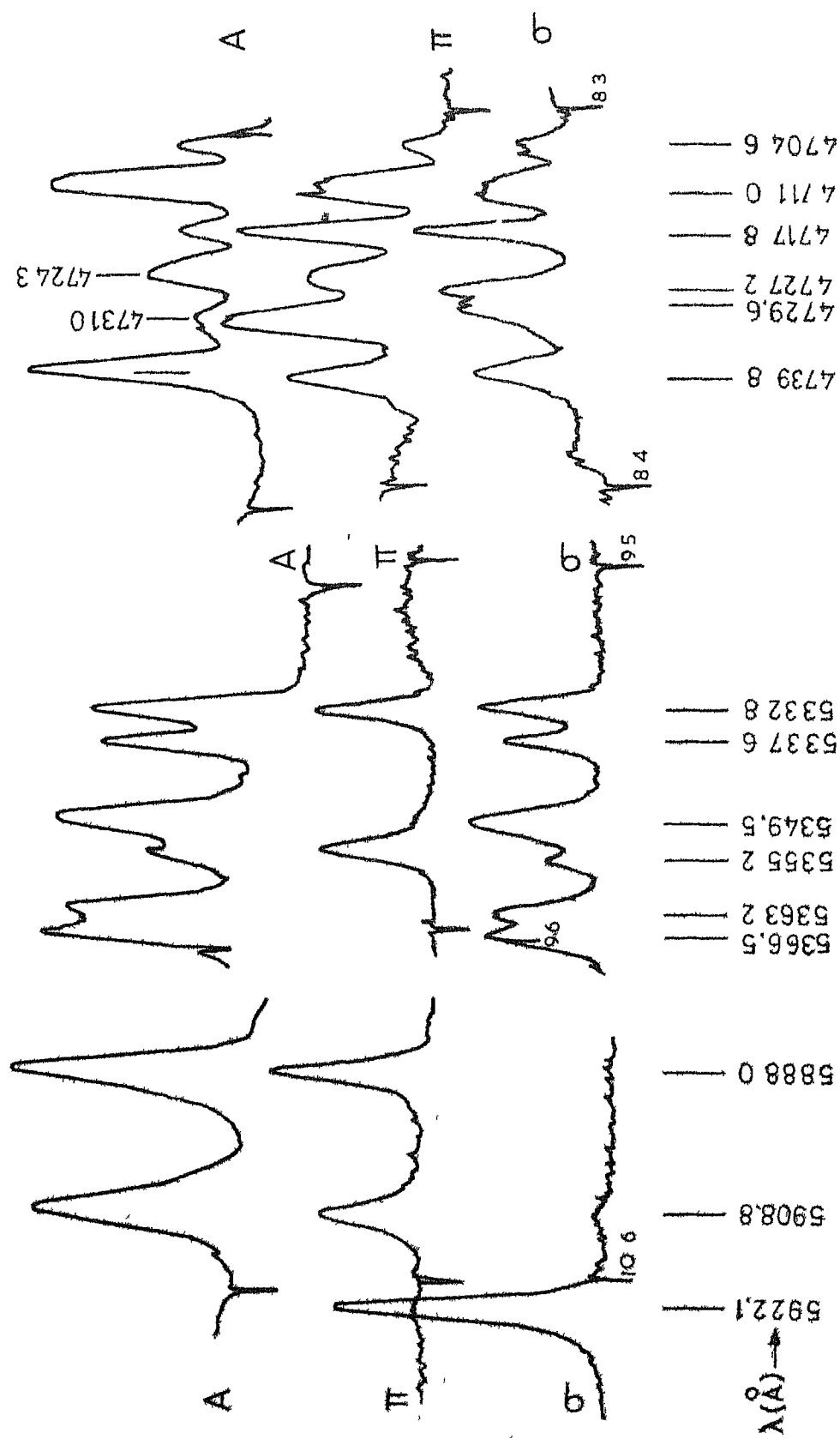


Fig. 3.5 Nd^{3+} in LaF_3 fluorescence at 77°K. $5D_0-7F_1$, $5D_1-7F_1$ and $5D_2-7F_1$ groups.

The position of the D_0 level being still unknown, the D_1-F_1 group is analysed first. Both these levels split as $A_2+B_1+B_2$ under C_{2v} and seven FD transitions are allowed in all between them, first in the σ polarization and two in the π . Under C_s symmetry one expects four σ lines and five unpolarized lines. The observed spectrum consists of four σ lines, one π line and one line that is present in both polarizations (5332.8\AA). This last line appears with a slightly larger width in the unpolarized spectrum. It is likely that it consists of two lines, one in σ and one in π . Thus a C_{2v} symmetry seems to be a valid approximation here also.

The transition assignments are done with the help of Table 3.7. In this table, the wavelengths, wavenumbers and the polarizations of the six observed lines are written in the first three columns. The energies of the levels of 5D_1 alongwith their species assignments as are determined so far are written on top of the next three columns. The table is now filled as a matrix of the differences of energies of the upper levels (5D_1) and the observed lines. These differences correspond to possible lower level positions and since particular lower levels are involved in more than one transitions some of these numbers must coincide with each other. The upper level positions are obtained from the absorption plates

Table 3.7

Difference matrix for the (D_1-F_1) group of fluorescence lines

Wavelength Å	Observed lines		D1,1(A_2 or B_2) D1,2(A_2 or B_2) D1,3(B_1)		
	Energy cm^{-1}	Polarization	19043 cm^{-1}	19056 cm^{-1}	19063 cm^{-1}
5366.5	18629	$\underline{\sigma}$	414 ²	427 ¹	434
5363.2	18640	σ	403	416 ²	423 ¹
5355.2	18668	$\underline{\pi}$	375 ³	388	395
5349.5	18688	σ	355	368	375 ³
5337.6	18730	σ	313 ⁴	326	333
5332.8	18747	$\sigma\pi$	296	309 ⁴	316 ⁴

Note: In this and the succeeding difference matrices, sets of
'matching' numbers are indicated by superscripts 1,2,3 etc.

and are accurate to $\pm 0.5 \text{ cm}^{-1}$. The fluorescence line positions however are not as accurately measurable. Thus a 'match' or 'coincidence' is taken to occur if any two numbers are within 5 cm^{-1} of each other. Four such sets of numbers; indicated by superscripts, could be seen in the table.

The match 423 and 427 implies two σ transitions from D1,2 and D1,3 to a lower level at that energy. These two upper levels however belong to (A_2 or B_2) and B_1 species respectively and cannot both have σ transitions to a single level (Table 3.1a). This coincidence is thus considered fortuitous. The match 414 and 416 is however valid since σ transitions from two levels both of A_2 or B_2 species are possible to a single level also of A_2 or B_2 species. The match 375 is again valid, and since a π transition is allowed only between A_2 and B_1 this determines the species of D1,1 as A_2 and that of the Stark component at 375 cm^{-1} as B_1 . D1,3 being already how¹ assigned as belonging to B_1 the remaining D1,2 must belong to B_2 species. The match 316, 309, 313 is valid polarization-wise and also determines the 313 cm^{-1} (average value) component of 7F_1 as A_2 , since it is only levels of this species that can have transitions to A_2 , B_1 as well as B_2 levels. This identification enables the assignment of the Stark component at 415 cm^{-1} as a B_2 . The splitting of 5D_1 therefore is D1,1-19043.4 cm^{-1} (A_2); D1,2-19056.1 cm^{-1} (B_2) and D1,3-19062.8 cm^{-1} (B_1).

The splitting of the 7F_1 is F1,1-313 cm^{-1} (A_2); F1,2-375 cm^{-1} (B_1) and F1,3-415 cm^{-1} (B_2). Figure 3.6 represents all the transitions terminating in 7F_1 diagramtically.

The magnetic dipole induced D_0 - F_1 group can now be used to fix the position of 5D_0 level. The separations of these three lines (5888 , 5908.8, 5922.1Å, Table 3.4) and their polarizations check with what can be expected from the species assignments made above for the 7F_1 . Using these energies of the Stark components of 7F_1 , 5D_0 is determined to lie at 17293 cm^{-1} .

With the splitting of the 7F_1 level thus established it is a rather simple matter to analyse the D_2 - F_1 group (also shown in figure 3.5). The transition assignments made are given in Table 3.4. However the partial polarization of four of these eight lines cannot be explained under C_{2v} but only under C_s . These are indicated by a * in the transition assignments column in this table. Out of the polarized lines, the MD transition at 4727.2Å (σ) between D2,5 and F1,3 (B_2) determines the species of the former to be A_2 as is tentatively assigned already. Similarly the MD transition (σ) to F1,2 (B_1) at 4729.6Å fixes the species of D2,2 as A_1 .
 ? The 4731.0Å line is present strongly in π and is weak along the axis. That is, it is a strong electric and weak magnetic transition. The lower level is F1,3 (B_2) and π polarized ??

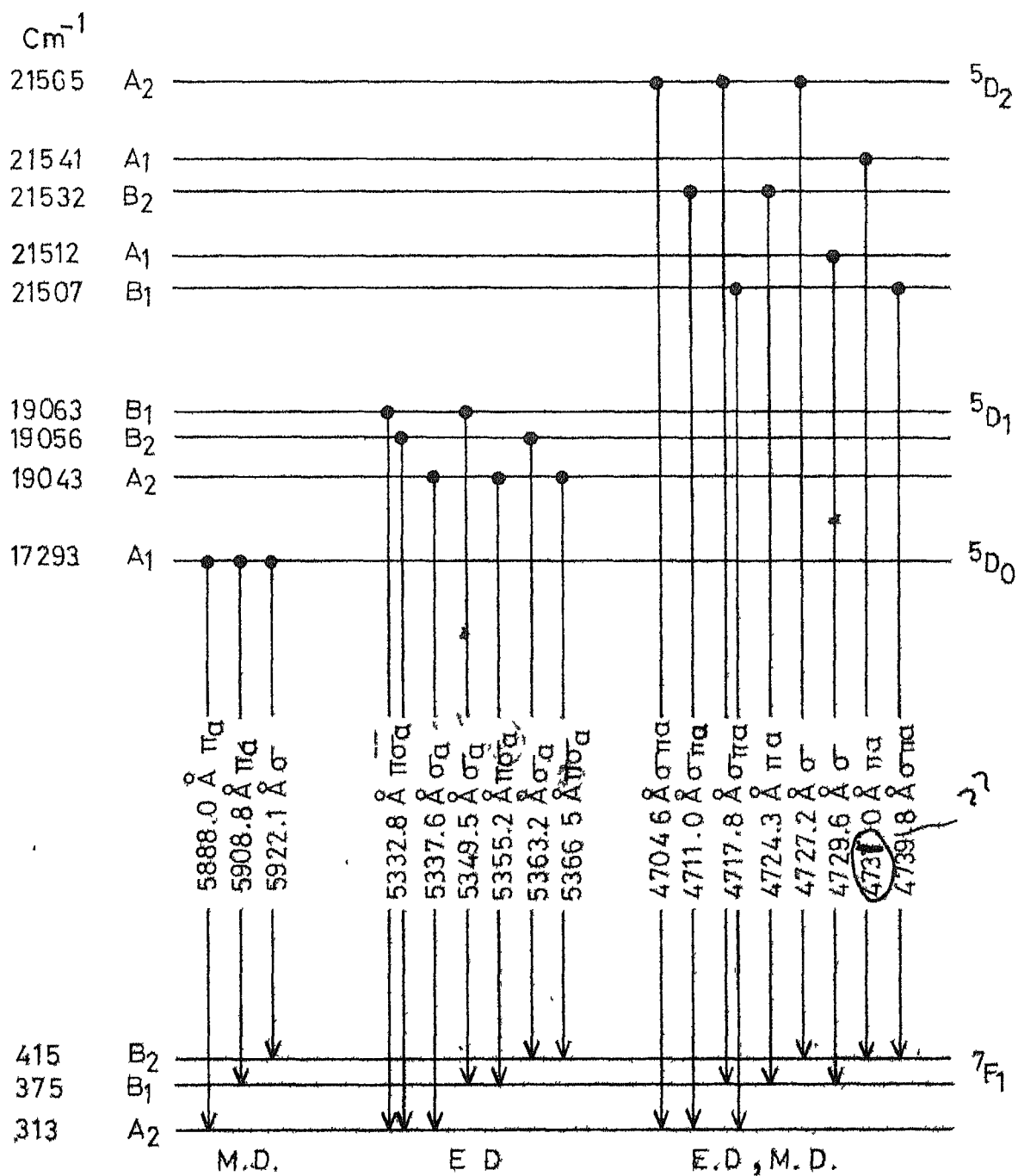


Fig. 3.6 Partial energy level diagram of $\text{Eu}^{3+}:\text{LaF}_3$ showing the observed fluorescence transitions at 77°K terminating in $7F_1$.

ED and MD transitions are allowed to it only from A_1 not B_1 . So the upper level D2,4 is an A_1 . The remaining D2,1 then has to be a B_1 . So the splitting of 5D_2 is D2,1-21507 cm^{-1} (B_1), D2,2-21512 cm^{-1} (A_1), D2,3-21532 cm^{-1} (B_2); D2,4-21541 cm^{-1} (A_1) and D2,5-21565 cm^{-1} (A_2).

3 3 4 Fluorescence terminating in 7F_2

Only the magnetic dipole induced D_1-F_2 group around 5550Å, shown in figure 3 7 is properly identified in this case. The D_2-F_2 group expected around 4780Å is masked by the Pr^{3+} fluorescence and D_0-F_2 lines are mixed up with those of D_1-F_4 . Table 3 8 gives the difference matrix for the D_1-F_2 , set up similar to Table 3 7. Using appropriate selection rules three coincidences at 964 cm^{-1} (A_1), 996 cm^{-1} (A_1) and 1098 cm^{-1} (B_2) are found to be valid and the two at 983 and 976 as invalid. Figure 3 8 summarizes the transition assignments. Here the above three levels are denoted as F2,1, F2,2 and F2,3 respectively.

With these assignments the last line at 5571.6Å [$D_{1,1}$ (A_2)-F2,3 (B_2)] should be σ polarized. Whereas there is significant intensity in the π polarization also. It is likely that this is due to a coincident transition from $D_{1,2}$ or $D_{1,3}$ to any one of the four Stark components of 7F_2 not determined so far. But the present method of analysis

Excitation 5145 Å , 400 mw

Input slit width 100 μ

Range 10 n amp

75

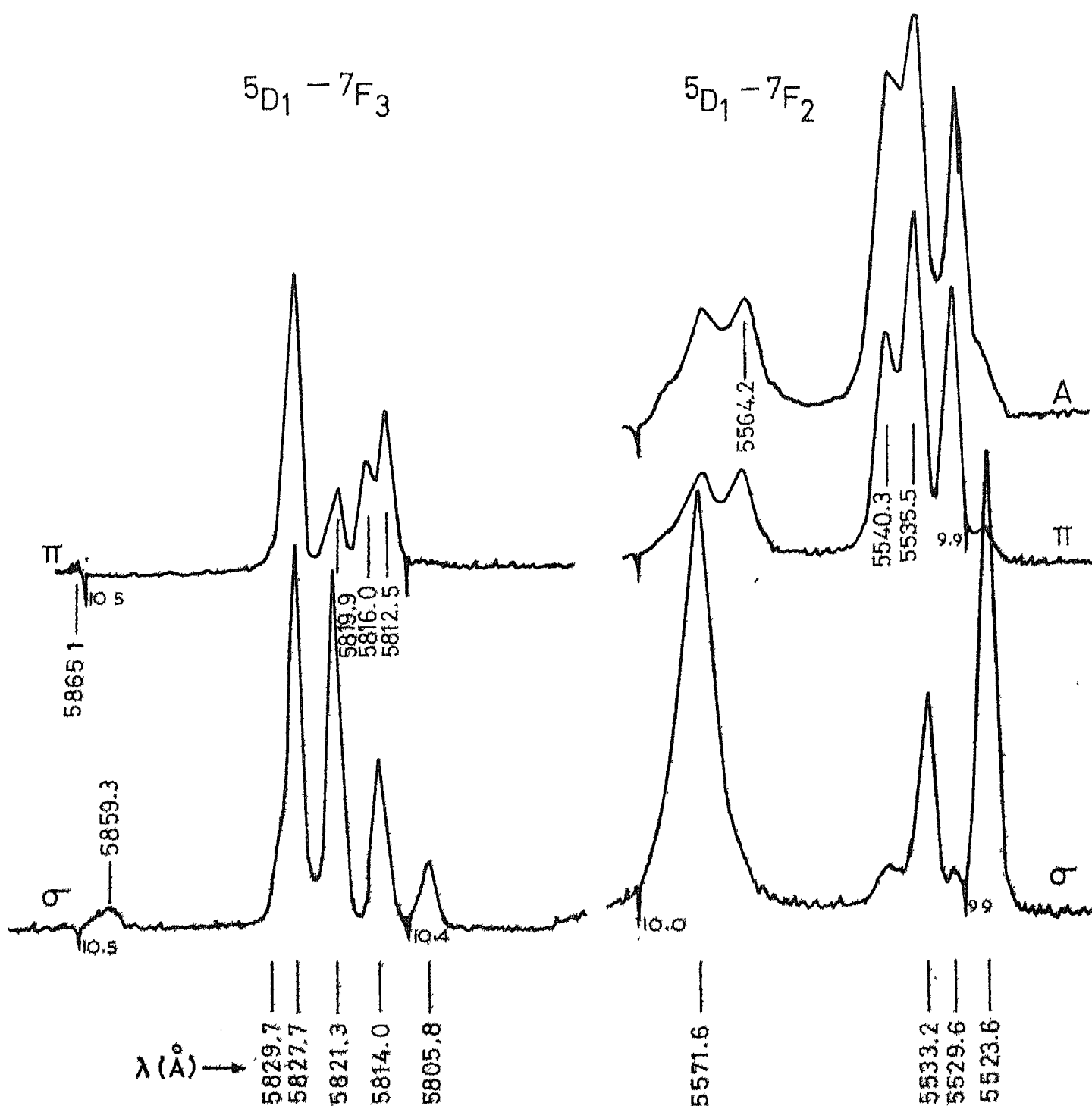


Fig. 1.7 $\text{Er}^{3+}:\text{LaF}_3$ fluorescence at 77°K, $5D_1 - 7F_2$ and $5D_1 - 7F_3$ spectra.

Table 3.8

Difference matrix for the (D_1-F_2) group of fluorescence lines

Wavelength Å	Observed lines		$D1,1(A_2)$	$D1,2(B_2)$	$D1,3(B_1)$
	Energy cm^{-1}	Polarization	19043 cm^{-1}	19056 cm^{-1}	19063 cm^{-1}
5571.6	17943	$\sigma\pi$	1100 ¹	1113	1120
5564.2	17967	π	1076	1089	1096 ¹
5540.3	18045	π	998 ²	1011	1018
5535.5	18060	π	983	996 ²	1003
5533.2	18068	σ	975	988	995 ²
5529.6	18080	π	963 ³	976	983
5523.6	18099	σ	944	957	964 ³

Note: The superscripts indicate sets of matching numbers.

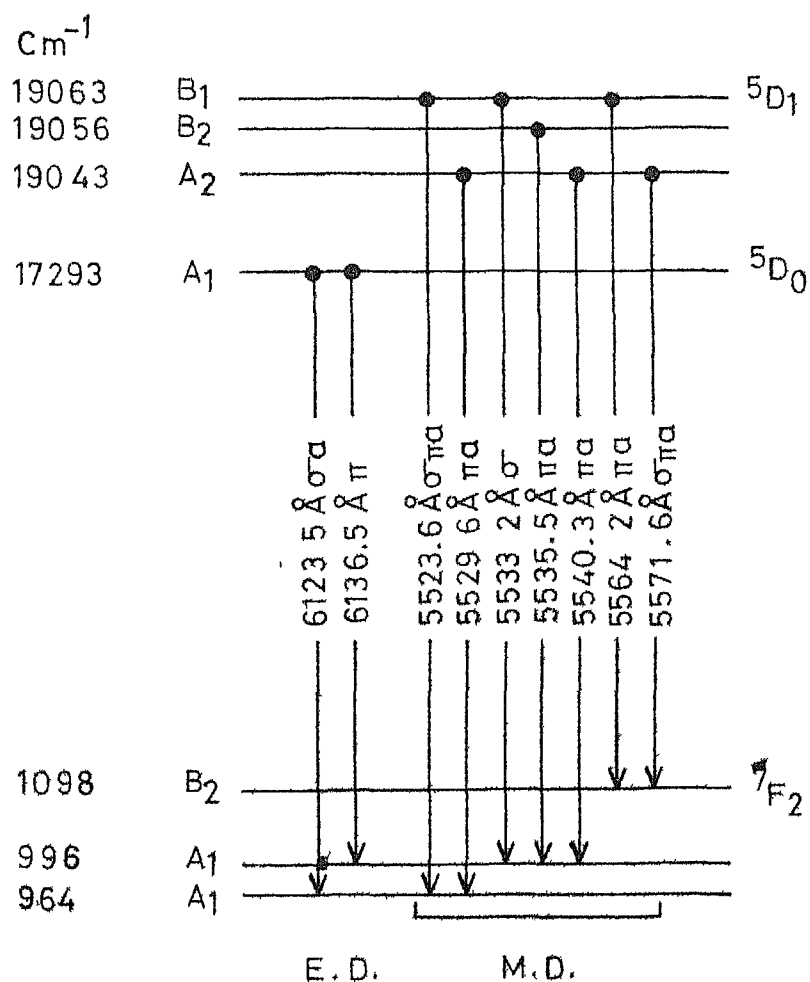


Fig. 3.8 Partial energy level diagram of $\text{Bi}^{3+}:\text{LaP}_3$ showing the observed fluorescence transitions at 77°K terminating in 7F_2 .

which relies on finding atleast two transitions to a single Stark component to identify it, cannot lead to any conclusions of this nature. The partial polarization can however be explained by considering the descent in symmetry to C_s . Only the latter is indicated in Table 3.4 to maintain consistency.

3.3.5 Fluorescence terminating in 7F_3

The ED transitions to this level from the 5D_0 are again forbidden by the zero to odd selection rule¹⁸. Any weak lines that might have become allowed due to J mixing are mixed up in the D_1-F_5 group and are not easily separable. The analysis is thus again started with the transitions from D_1 . This group (D_1-F_3) is also illustrated in figure 3.7.

The difference matrix for this group given in Table 3.9 indicates the following seven lower levels, 1867- A_1 ; 1843, 1889- B_1 ; 1862, 1884, 1908- A_2 and 1996- A_2 or B_2 . The numbers written here are the averages of the sets of matching numbers indicated by superscripts in the table. The expected splitting of the level is $A_1 + 2A_2 + 2B_1 + 2B_2$ (Table 3.6). Thus the one A_1 level and two B_1 levels are accounted for, whereas the A_2 levels are in excess. That means atleast one of the coincidences is fortuitous and should be discarded. A choice is made here to drop the 1862 cm^{-1} coincidence since, dropping any of the other two would leave one line

Table 3.9

Difference matrix for the (D_1-F_3) group of fluorescence lines

Wavelength \AA	Observed lines		$D1,1(A_2)$	$D1,2(B_2)$	$D1,3(B_1)$
	Energy cm^{-1}	Polarization	19043 cm^{-1}	19056 cm^{-1}	19063 cm^{-1}
5805.8	17219	σ	1824	1837	1844 ¹
5812.5	17200	π	1843 ¹	1856	1863 ²
5814.0	17195	σ	1848	1861 ²	1868 ³
5816.0	17189	π	1854	1867 ³	1874
5819.9	17178	π	1865	1878	1885 ⁴
5821.3	17174	σ	1869	1882 ⁴	1889 ⁵
5827.7	17155	$\sigma \pi$	1888 ⁵	1901	1908 ⁶
5829.7	17,148	σ	1895	1908 ⁶	1915
5859.3	17062	σ	1981	1994 ⁷	2001
5865.1	17045	γ	1998 ⁷	2011	2018

Note: Superscripts indicate sets of matching numbers.

unassigned (5819.9\AA or 5829.7\AA). Accepting the remaining two A_2 coincidences as valid, the 1996 is assigned to be a B_2 . Thus only six levels out of the expected seven are determined.

The D_2-F_3 group around 5100\AA is illustrated in figure 3.9. There are only 12 lines in the group whereas all 35 possible transitions are allowed either by MD or ED selection rules. The axial spectrum does not clearly resemble either the σ spectrum or the π spectrum and contains both kinds of transitions. Also several lines are partially polarized. Attempts to make transition assignments using a difference matrix did not lead to any conclusive results. The number of coincidences is too large, and it is not possible to check the validity or otherwise of the coincidences because of the partial polarization of most of the lines.

The splitting of the 7F_3 is thus taken as determined from the D_1-F_3 group only and is as follows. F3,1-1843 (B_1); F3,2-1867 (A_1); F3,3-1884 (A_2); F3,4-1889 (B_1); F3,5-1908 (A_2) and F3,6-1996 (B_2). The observed transitions of this group are given in the bar diagram of figure 3.10.

3.3.6 Fluorescence terminating in 7F_4

The group of six lines between 6800 and 7020\AA (figure 3.11) is in the expected position for the D_0-F_4 group. All

Excitation 4580 Å, 50 mw

Input slit width 50 μ

Range 10 n amp

81

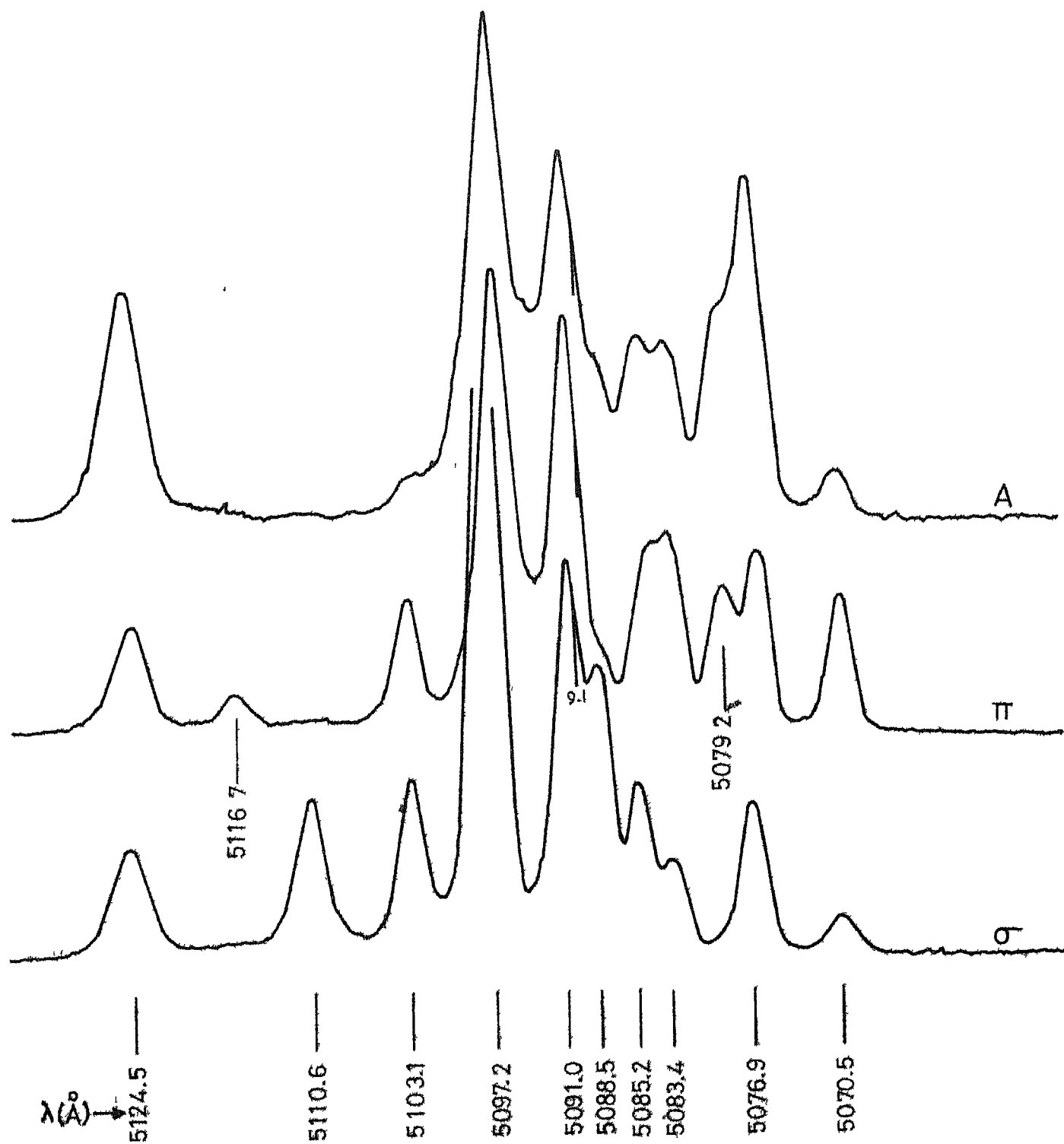


Fig. 3.9. $\text{Er}^{3+}:\text{LaF}_3$ fluorescence at 77°K; $^3\text{P}_2 \rightarrow ^3\text{F}_4$ group.

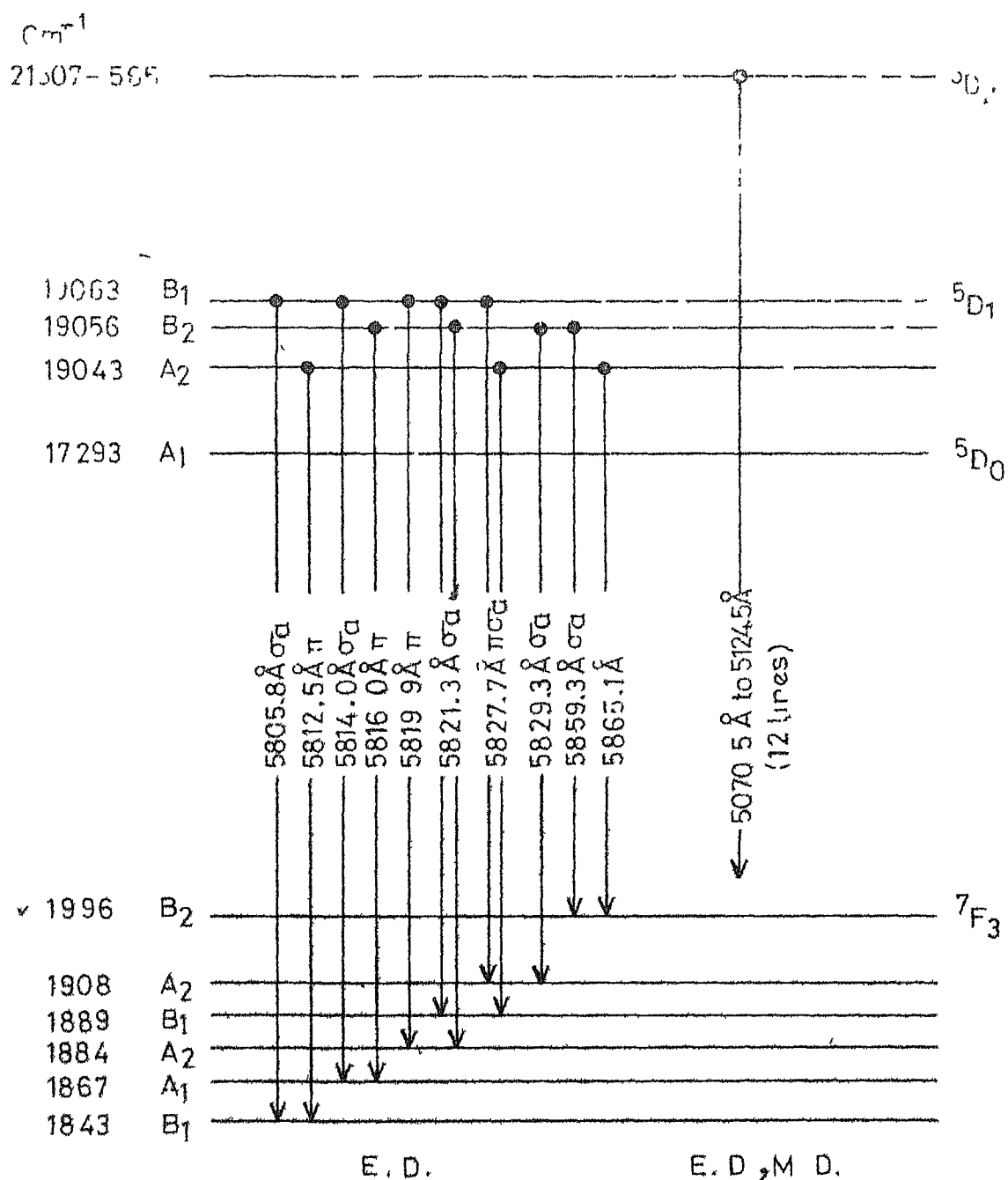


Fig. 3.10 Partial energy level diagram of Mn³⁺:LaF₃ showing the observed fluorescence transitions at 77°K terminating in 7F₃.

the lines except the first one at 6809.5Å are polarized and using the energy of 5D_0 level determined already, the following Stark components are obtained for 7F_4 2788, 2847, 3047- A_1 or B_1 ; 2612 (A_1 , B_1 or B_2); and 2872, 2929- B_2 . Out of the nine levels which split as $3A_1 + 2A_2 + 2B_1 + 2B_2$, ED transitions to the two A_2 components are forbidden and cannot be determined from this group. These have to be determined as well as the ambiguity of the above species assignments removed, from the analysis of the D_1-F_4 group.

The D_1-F_4 group is illustrated in figure 3.12. This is a group of fourteen lines almost all of which are polarized. The difference matrix for this group is given in Table 3.10. A perusal of this table produces the following eight valid (polarizationwise) coincidences 2894- A_1 ; 2616, 2873- B_1 ; 3068, 2771, 2852- A_2 ; 2873- B_2 and 2925- A_2 or B_2 . Some of these agree with the Stark level positions arrived at from the D_0-F_4 group within the experimental uncertainty. Combining the information obtained from both the groups, one has a total of 11 levels: 2894- A_1 ; 2614, 2873- B_1 ; 2788, 2847, 3047- A_1 or B_1 ; 3068, 2771, 2852- A_2 and 2873, 2926 - (B_2). The numbers written are 'averages' and the levels determined by the transitions from 5D_0 are underlined. Since only nine levels are expected some of the above must be wrong.

not shown
in table?

Excitation 5145 Å, 400 mw
 Input slit width 150 μ
 Range 3 n amp

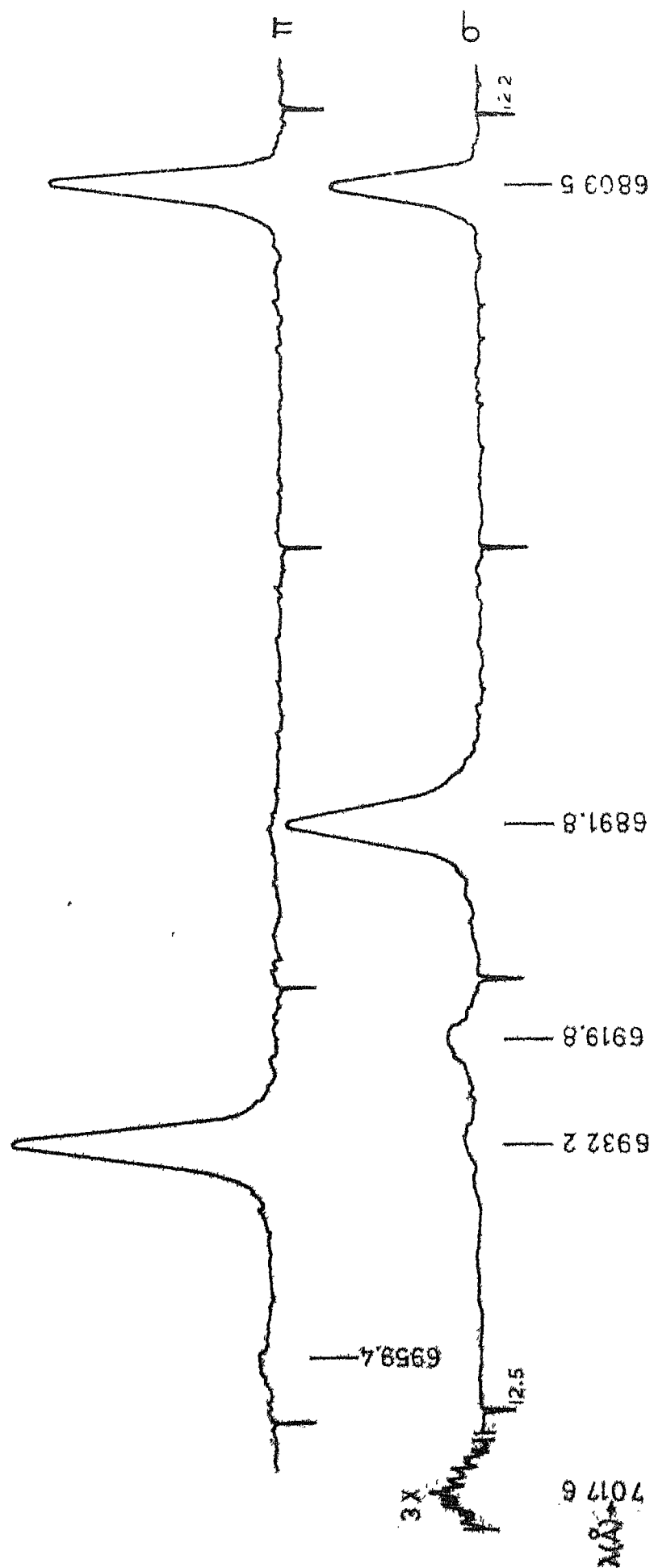
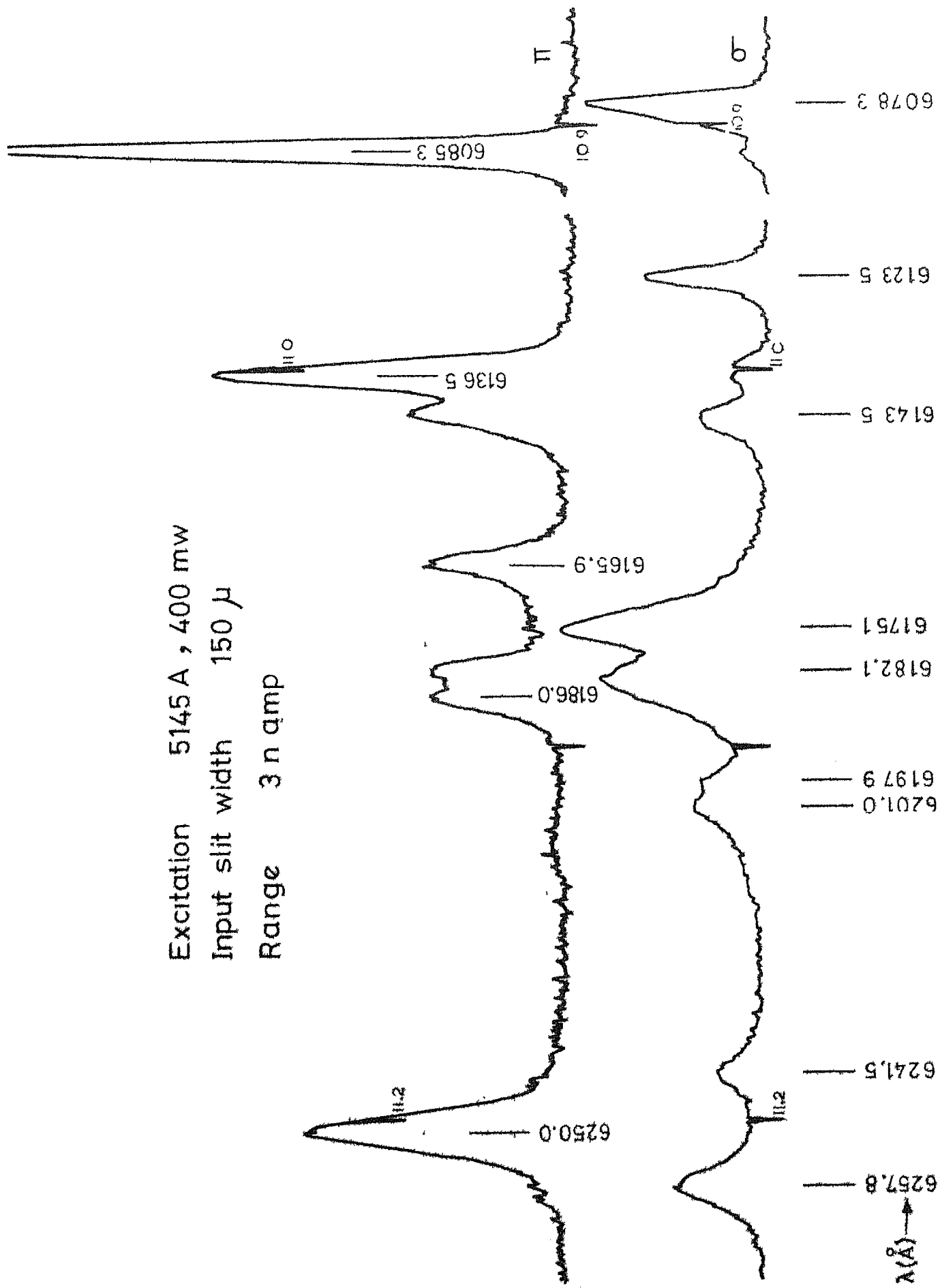


Fig. 3.11 $\text{Eu}^{3+}:\text{LaF}_3$ fluorescence at 77°K, $5_{D_0} \rightarrow 7_{F_4}$ group.

Excitation 5145 A , 400 mw
 Input slit width 150 μ
 Range 3 n amp



... at 77°K, $5D_1 - 3P_4$ system.

Table 3.10

Difference matrix for the (D_1-F_4) group of fluorescence lines

Observed lines			$D1,1(A_2)$	$D1,2(B_2)$	$D1,3(B_1)$
Wavelength λ	Polarization	Energy cm^{-1}	19043 cm^{-1}	19056 cm^{-1}	19063 cm^{-1}
6078.3	σ	16447	2596	2609	2616 ¹
6085.3	π	16428	2615 ¹	2628	2635
6123.5	σ	16326	2717	2730	2737
6136.5	$\pi\sigma$	16291	2752	2765	2772
6143.5	$\sigma\pi$	16273	2770	2783	2790
6165.9	π	16213	2830	2843	2850
6175.1	σ	16189	2854	2867	2874 ²
6182.1	$\sigma\pi$	16171	2872 ²	2885	2892 ³
6186.0	π	16161	2882	2895 ³	2902
6197.9	σ	16129	2914	2927 ⁴	2934
6201.0	σ	16121	2922 ⁴	2935	2942
6241.5	σ	16017	3026	3039	3046 ⁵
6250.0	π	15995	3048 ⁵	3061	3068 ⁶
6257.8	σ	15975	3068 ⁶	3081	3088

Note. Superscripts indicate sets of matching numbers.

Out of three A_2 levels, the 2771 is chosen to be dropped, as the two lines which give this coincidence 6136.5\AA and 61435\AA can be alternatively assigned, the former as a transition from 5D_0 to the component F2,2 of 7F_2 and the latter as a transition from D1,3 to the 2790 cm^{-1} (A_1 or B_1) level determined from the D_0-F_4 group. Out of the two coincidences of the A_1 , B_1 type at 2873 and 2894 obtained only from the D_1-F_4 group, the 2894 is retained, as dropping that would leave the 6186.0\AA line unassigned. In conclusion, the splitting of 7F_4 is F4,1- 2614 cm^{-1} (B_1); F4,2- 2788 cm^{-1} (A_1 or B_1); F4,3- 2847 cm^{-1} (A_1 or B_1); F4,4- 2852 cm^{-1} (A_2); F4,5- 2873 cm^{-1} (B_2); F4,6- 2894 cm^{-1} (A_1); F4,7- 2926 cm^{-1} (B_2); F4,8- 3047 cm^{-1} (A_1 or B_1) and F4,9- 3068 cm^{-1} (A_2). Figure 3.13 summarizes all the transitions observed terminating in 7F_4 .

The line at 6123.5\AA which is not assigned to any of the D_1-F_4 transitions is probably due to a transition from 5D_0 to F2,1 (964 cm^{-1}).

A group of three well polarized ED induced lines is observed around 5920\AA in the spectrum excited with the 4580\AA radiation. This is shown in figure 3.3 along with the D_1-F_0 group. This is the expected region of the D_2-F_4 group but none of these lines can be understood as due to transitions between the 5D_2 and the Stark components of

7F_4 determined above. They are quite far off (2900 cm^{-1}) from the laser line to be thought of as Raman lines (their intensity also does not show any dependance on the polarization of the incident laser light). They do not also check with the expected positions of electronic Raman lines of either Eu^{3+} or Pr^{3+} nor with any fluorescence of $\text{Pr}^{3+}:\text{LaF}_3$. These are left unassigned.

3.3.7 Fluorescence terminating in 7F_5

Figures 3.14 and 3.15 illustrate D_1-F_5 and D_2-F_5 groups of lines. The D_1-F_5 group between 6480 and 6700Å is very weak (the polarized spectra being more so) resulting in very inaccurate wavelength measurements. The D_2-F_5 group between 5600 and 5730Å does not suffer from this problem but the analysis is hampered by a multitude of coincidences (in the difference matrix) and occurrence of several partially polarized lines. From this group it could be determined that the Stark components of 7F_5 occur between 3700 and 4100 cm^{-1} . Using these numbers the first four lines of the previous group (that is the one around 6600Å) are assigned as to be due to D_0-F_3 transitions.

Excitation 5145 Å, 400 mw
 Input slit width 150 μ
 Range 1 namp

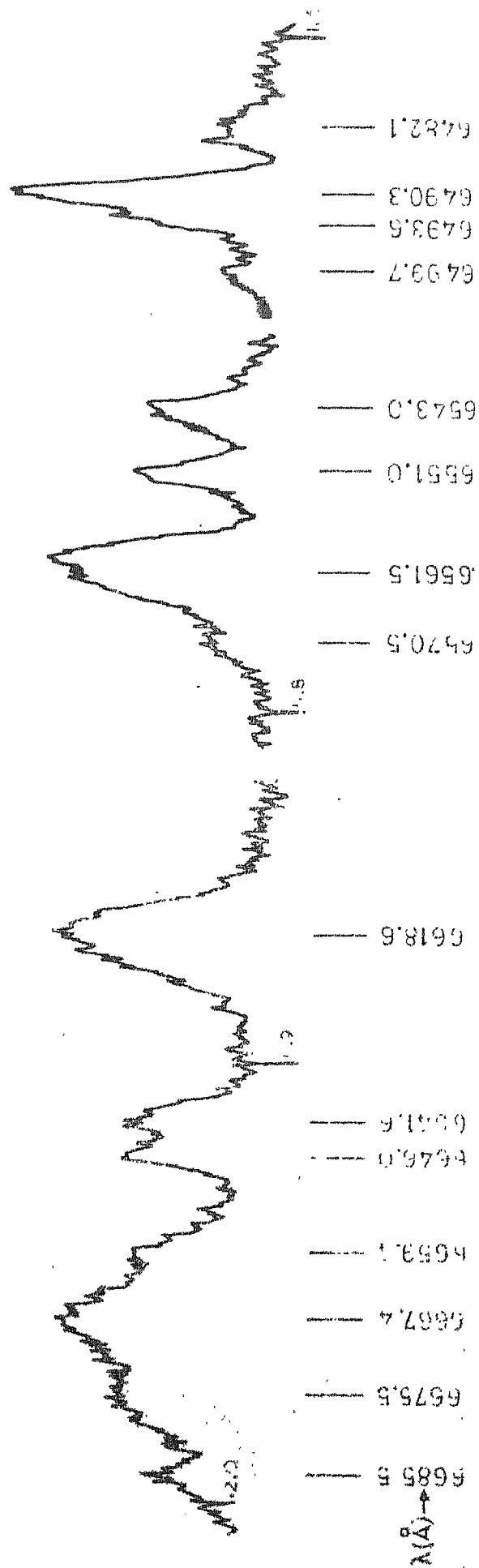


Fig. 3.14: Fe^{2+} emission at 7115, 501-25 group.

Excitation 4580 Å, 80 mw

Input slit width 100 μ

Range 3n amp

91

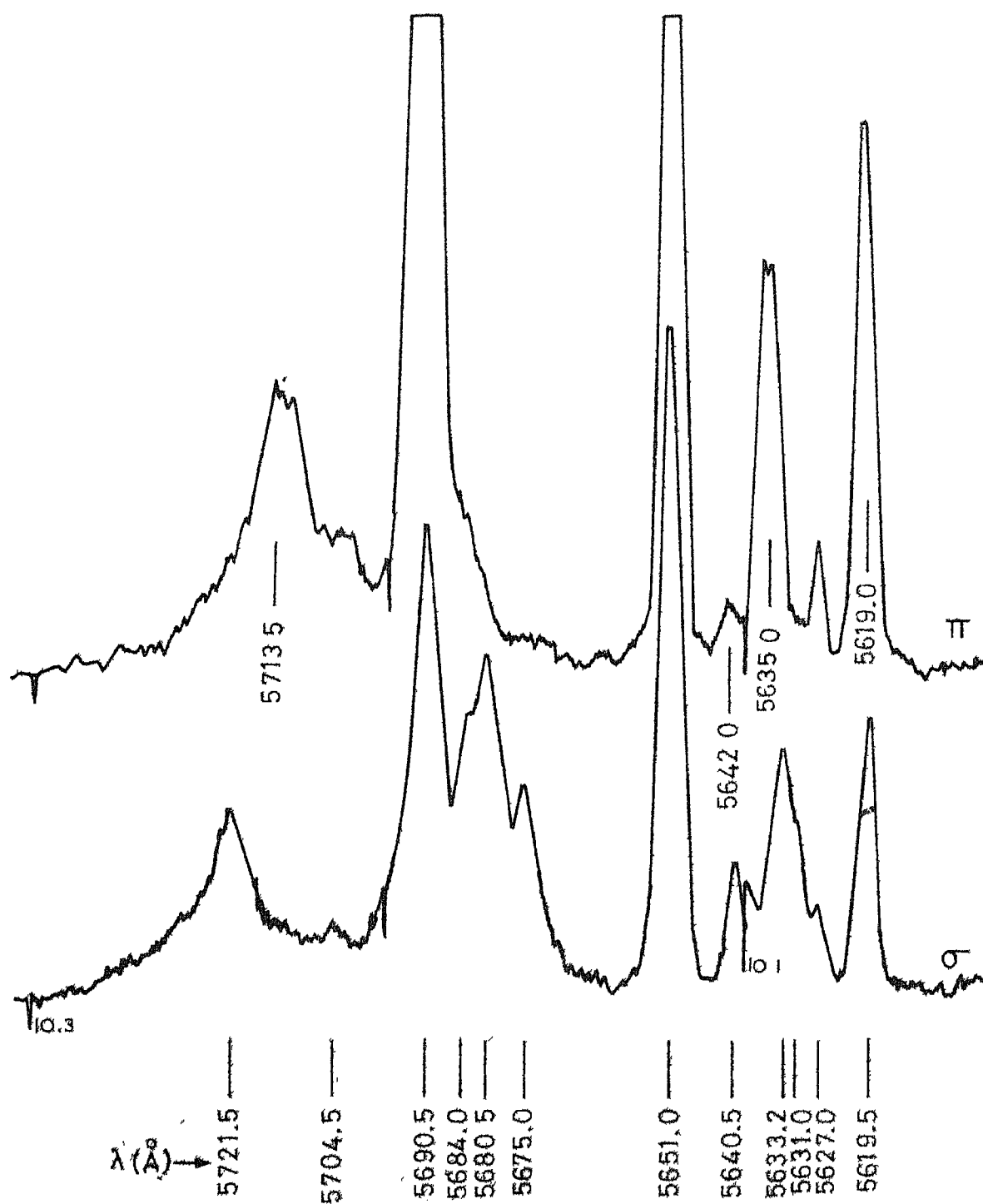


Fig. 3.15 Ar³⁺:LaF₃ fluorescence at 77°K, ⁵D₂-⁷F₅ group.

Table 3.11

The energy levels of $\text{Eu}^{3+} : \text{LaF}_3$
(0 to 22,000 cm^{-1})

SLJ	Stark level Designation	Energy cm^{-1}	Species (under C_{2v})	Centre of gravity cm^{-1}
7F_0	F0	0	A_1	
	F1,1	313	A_2	
7F_1	F1,2	375	B_1	368
	F1,3	415	B_2	
7F_2	F2,1	964	A_1	
	F2,2	997	A_1	1020*
	F2,3	1098	B_2	
7F_3	F3,1	1843	B_1	
	F3,2	1867	A_1	1898 ⁺
	F3,3	1884	A_2	
	F3,4	1889	B_1	
	F3,5	1908	A_2	
	F3,6	1996	B_2	
7F_4	F4,1	2614	B_1	
	F4,2	2788	A_1 or B_1	
	F4,3	2847	A_1 or B_1	
	F4,4	2852	A_2	
	F4,5	2873	B_2	2879
	F4,6	2894	A_1	
	F4,7	2926	B_2	
	F4,8	3047	A_1 or B_1	
	F4,9	3068	A_2	
7F_5		3700-4100		
7F_6		Not observed		

Table 3.11 (contd.)

SLJ	Stark level Designation	Energy cm^{-1}	Species (under C_{2v})	Centre of gravity cm^{-1}
$5D_0$	D0	17293	A_1	
$5D_1$	D1,1	19043.4	A_2	19054
	D1,2	19056.0	B_2	
	D1,3	19062.8	B_1	
$5D_2$	D2,1	21507.4	B_1	21532
	D2,2	21512.3	A_1	
	D2,3	21532.0	B_2	
	D2,4	21541	A_1	
	D2,5	21565	A_2	

* Average of the three observed levels

+ Average of the six observed levels

Table 3.11 lists the determined Stark levels and their symmetry species under C_{2v} . On the whole, the assumption of C_{2v} symmetry for the rare earth site seems to be fairly valid. Almost all the lines and their polarizations are satisfactorily accounted for under this framework. Better assignments of the partially polarized lines and the multiply assigned lines can probably be done only with an order of magnitude improvement in the resolution and wavelength accuracy. This is necessary also to improve the assignments of the lines whose wavelength separations are of the same order as the present inaccuracy. Infrared absorption data when available, would of course be very useful for the assignments.

REFERENCES

1. L.G. De Shazer and G.H. Dieke, J. Chem. Phys. 38, 2190 (1963).
2. G.S. Ofelt, J. Chem. Phys. 38, 2171 (1963).
3. B.R. Judd, Mol. Phys. 2, 407 (1959).
4. E.V. Sayre and S. Freed, J. Chem. Phys. 24, 1211 and 1213 (1956),
 C. Brecher, Phys. Rev. 155, 178 (1967),
 N.C. Chang and J.B. Gruber, J. Chem. Phys. 41, 3227 (1964),
 H.H. Caspers, H.E. Rast and J.L. Fry, J. Chem. Phys. 47, 4505 (1967),
 G.H. Dieke, Spectra and Energy Levels of Rare Earth Ions in Crystals (Interscience 1968); and references contained therein,
 N. Yamada and S. Shlyonoya, J. Phys. Soc. Jap. 31, 847 (1971).
5. M.J. Weber, in Optical Properties of Ions in Crystals ed. H.M. Crosswhite and H.W. Moos (Interscience 1967), page 467.
6. Collete de Rango, G. Tsoucaris and Ch. Zelwer, C.R. Acad. Sc. Paris, 263, 64 Serie. C (1966).
7. J.M. Baker and R.S. Rubins, Proc. Phys. Soc. 78, 1353 (1961).
8. I. Oftedal, Zs. f. Physik, 5, 272 (1929); 13, 190 (1931).
9. M. Mansman, Z. Anorg Allgem, Chem. 331, 98 (1964).
10. R.P. Bauman and S.P.S. Porto, Phys. Rev. 161, 842 (1967).

11. H.H. Caspers et.al., J. Chem. Phys. 43, ²¹²⁴~~3214~~ (1965).
12. V.K. Sarma, J. Chem. Phys. 54, 496 (1971).
13. E.Y. Wong, O.M. Stafsudd and D.R. Johnston, Phys. Rev. 131, 990 (1963).
14. P. Venkateswarlu, unpublished.
15. H.E. Rast, J.L. Fry and H.H. Caspers, J. Chem. Phys. 46, 1460 (1967).
16. W.F. Krupke and J.B. Gruber, J. Chem. Phys. 39, 1024 (1963).
17. K. Schlyter, Arkiv Kemi. 5, 73 (1952).
18. G.S. Ofelt, J. Chem. Phys. 37, 511 (1962).
19. M.J. Weber and R.F. Schaufele, J. Chem. Phys. 43, 7102 (1965).

CHAPTER 4

OPTICAL ABSORPTION AND
FLUORESCENCE SPECTRA OF $\text{Nd}^{3+}:\text{LaF}_3$ ABSTRACT

The optical absorption spectrum of $2\%\text{Nd}^{3+}:\text{LaF}_3$ has been observed in the region 0.25 to 0.9 microns whereas published data is available in the range 0.4 to 5 microns. Five groups of lines are observed in the ultraviolet absorption spectrum (2500-4000Å). The SLJ level designations could be assigned to the concerned levels of four of these groups by comparison with the spectrum reported for $\text{Nd}^{3+}:\text{LaCl}_3$. The absorption spectrum in the region 4000-9000Å conforms with earlier data but for the observation of few sharp extra lines. These extra lines are assigned to be vibronic transitions.

At LNT, excitation with the 5145\AA ($19,431\text{ cm}^{-1}$) emission of the Ar^+ laser produced fluorescence from the E ($19,300\text{ cm}^{-1}$), D ($17,450\text{ cm}^{-1}$) and R ($11,600\text{ cm}^{-1}$) levels as well as some other fluorescence lines whose intensity was proportional to $P^{1.76}$ where P is the incident laser power. These are identified as arising from the K ($26,400\text{ cm}^{-1}$) and L ($28,350\text{ cm}^{-1}$) levels of the Nd^{3+} . This assignment is confirmed by the fluorescence obtained with N_2 laser excitation (3371\AA) which contained transitions from the K and L levels to several lower levels and also from R to the ground state. A sequential two step excitation process is proposed to explain the population of these two high lying levels when excited with the $19,430\text{ cm}^{-1}$ radiation.

Three lines of the R-Z group showed significant self absorption. The simple geometry of laser excitation permitted an accurate calculation of oscillator strengths of these transitions using this effect.

With the 5145\AA excitation, fluorescence from S and A levels also is observed at room temperature beside the fluorescence observed at LNT. The intensity of these two transitions increases with temperature above RT. This is explained as due to an anomalous increase in the populations of S and A levels by an ion pair relaxation process active at high temperatures.

Several lines, in absorption as well as fluorescence are partially polarized, contrary to the expected behaviour of Kramers' ions in orthorhombic sites. Some possible explanations are offered for this behaviour.

4.1 Introduction

Studies on the absorption and fluorescence spectra of Nd^{3+} ion in various lattices have been carried out by several workers¹⁻⁴. Satten's¹ work on the absorption spectrum of $\text{Nd}(\text{BrO}_3)_3 \cdot 9\text{H}_2\text{O}$ and that of Dieke and Carlson² on the absorption and fluorescence spectra of $\text{Nd}^{3+}:\text{LaCl}_3$ firmly established the identity of several levels below $30,000 \text{ cm}^{-1}$. Aggarwal et.al⁴ extended the absorption measurements in $\text{Nd}^{3+}:\text{LaCl}_3$ upto $40,000 \text{ cm}^{-1}$. In their analysis, Carlson and Dieke used free ion energies and wavefunctions calculated by Wybourne⁵ and Carlson and Crosswhite⁶ neglecting configuration interaction. Configuration interaction was later included by Rajnak⁷ to improve the agreement between theoretical and experimental results for $\text{Nd}^{3+}:\text{LaCl}_3$. A calculation made by Crosswhite et.al⁸

including various magnetic interactions namely spin-spin, spin-other orbit etc. beside configuration interaction, reproduced the observed energy levels in LaUCl_3 with an R.M.S. deviation of 9.5 cm^{-1} . The energy levels are shown in figure 4.1.

Wong et.al.⁹ were the first to report the absorption spectrum of $\text{Nd}^{3+}:\text{LaF}_3$. By studying the spectrum in the range 5000 to 8600\AA at liquid helium and liquid nitrogen temperatures, they established the first excited Stark component of the $^4\text{I}_{9/2}$ ground level to be at 44 cm^{-1} . Complete crystal field splittings of most of the levels in this region (5000 to 8600\AA) were also obtained. They noticed however that several lines in the spectrum are polarized, contrary to the expected behaviour of a Kramers ion under an orthorhombic field (chapter 3). They opined that this could be due either to a coupling of neighbouring Nd ions or to a hidden selection rule. Caspers et.al.¹⁰ (hereafter referred to as CRB) extended the absorption study to cover the region 0.4μ to 5μ . They also observed infrared fluorescence due to transitions between the $^4\text{F}_{3/2}(\text{R})$ level at $11,600 \text{ cm}^{-1}$ and the various levels of the ground multiplet $^4\text{I}_9$. From this they could deduce the Stark splitting of the $^4\text{I}_{9/2}$ ground state as 0, 45, 136, 296 and 500 cm^{-1} (labelled Z_1 to Z_5). Using the centres of gravity of eight levels ($^4\text{I}_{9/2, 11/2, 13/2}$, $^4\text{F}_{3/2, 9/2}$, $^4\text{G}_{7/2, 9/2}$ and $^2\text{F}_{1/2}$) for

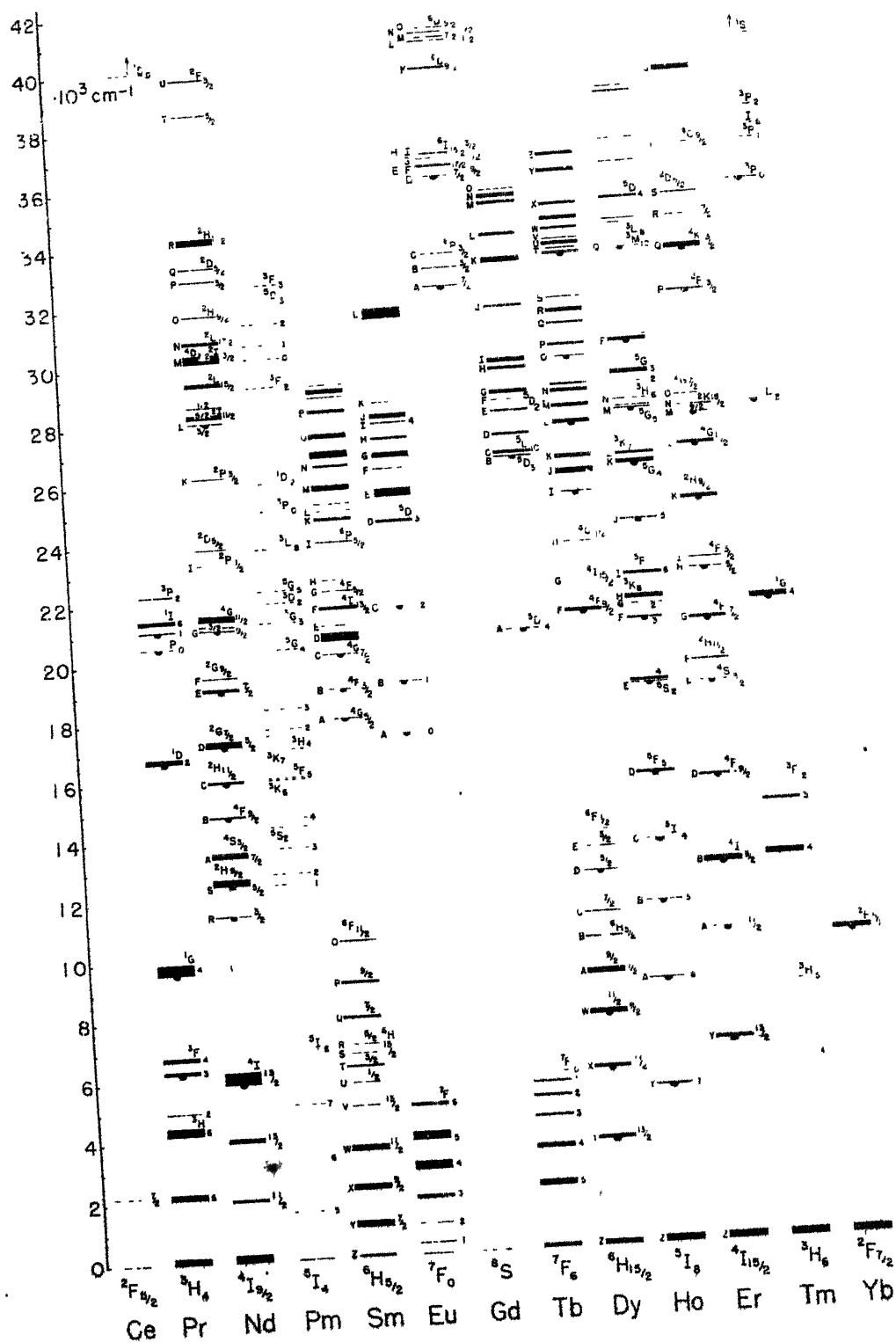


Fig. 4.1 Free ion energy levels of rare earth ions
(from Dieke, ref. 2).

which total Stark splitting is thus established, they calculated the intermediate coupling parameters applicable to $\text{Nd}^{3+}:\text{LaF}_3$ by a variational method given by Wong¹¹. The splitting of the $^4\text{I}_{15/2}$ level which was not completely observed by them was later reported by Voronko et.al¹² from infrared absorption data.

An early investigation of the absorption spectrum of NdF_3 , which is isomorphous with LaF_3 , is due to Chow¹³. Using Zeeman effect he was able to identify several weak lines in the spectrum as vibronic lines. The electronic level positions (of Nd^{3+} ion) identified by him are in agreement with those determined later^{9,10} in $\text{Nd}^{3+}:\text{LaF}_3$.

In this work the absorption studies on $\text{Nd}^{3+}:\text{LaF}_3$ are extended upto $40,000\text{ cm}^{-1}$ resulting in the identification of four levels in the region $28,000 - 40,000\text{ cm}^{-1}$. Using laser excitations fluorescence is obtained in ultraviolet and visible regions also beside the infrared that is earlier reported. The analysis of this spectrum resulted in a better determination of the Stark components of several levels below $13,000\text{ cm}^{-1}$, as well as identification of the $^2(\text{PD})_{3/2}^{\text{or K}}$ level at $26,400\text{ cm}^{-1}$ which is not observed in the absorption spectrum. The fluorescence spectrum also revealed a two photon absorption mechanism (under laser excitation) and two ion pair relaxation processes active at high temperatures.

Self absorption shown by some of the lines is used to calculate the oscillator strengths of the transitions involved.

4.2 The Optical Absorption Spectrum at LNT

The single crystal of LaF_3 doped with 2% Nd was also purchased from Optovac Co. and loaned to us by Professor H.P. Broida. This crystal also was a slab of $10 \times 7 \times 4 \text{ mm}^3$ size with the c-axis perpendicular to the broadest face. The axis is checked by viewing under a polarization microscope as well as by X-ray Laue pattern. A small piece of this crystal is cut for use in the EPR experiment. The remaining piece was repolished and used for the optical work.

The ultraviolet absorption spectrum⁺ (2000 to 4000 Å) which is not so far reported, consists of five groups of lines between 2500 and 3600 Å. There are several strong overabsorbed lines, as well as some weak lines in the spectrum. Most of the weak lines are seen to occur at energies lower by about 45 and 135 cm^{-1} from neighbouring strong lines. It is likely that these are due to transitions from the first two excited Stark levels (Z_2 and Z_3) of the ground state at those energies. Table 4.1 lists the observed absorption lines and the transition assignments made with this assumption. It is necessary however to record the spectrum at liquid helium temperature to confirm these assignments. The Stark levels thus determined

⁺ This is shown in figure 4.2.

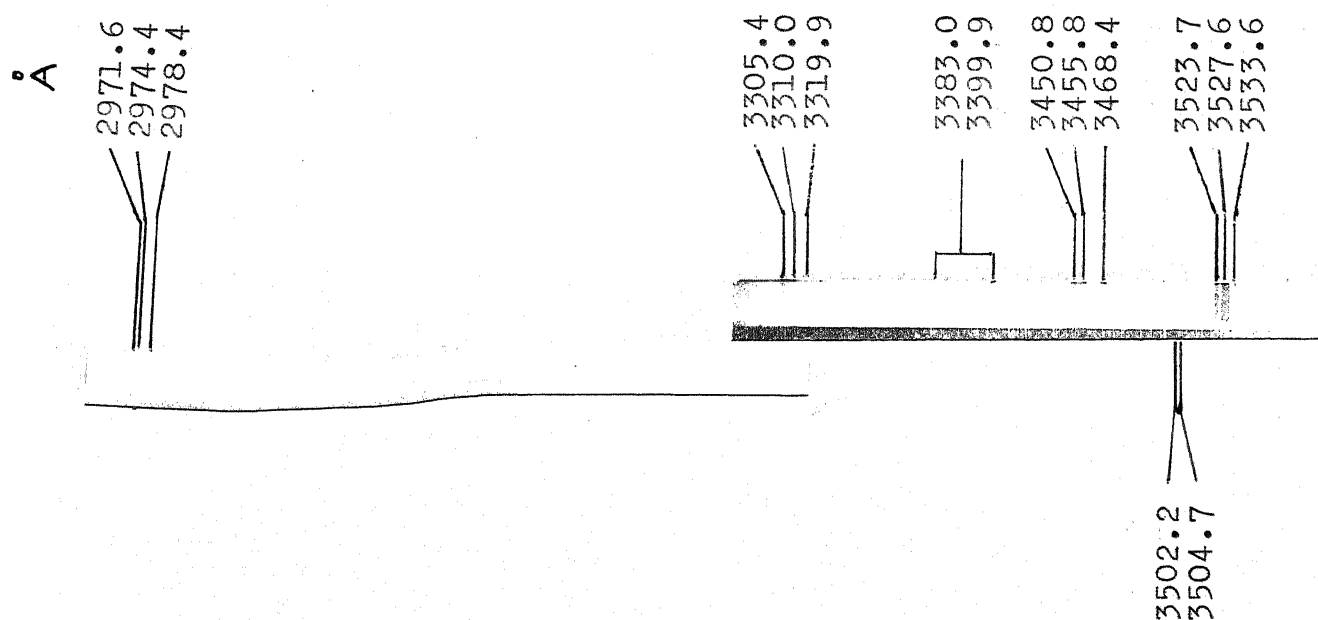


Fig. 4.2 $\text{Nd}^{3+}:\text{LaF}_3$ absorption spectrum at 77°K ,
2500-4000Å.

The two lines at 2907.2 and 2536.6Å could not be reproduced in print and hence not shown here.

Table 4.1

The Ultraviolet absorption spectrum of $\text{Ni}^{3+}:\text{LaF}_3$
at liquid nitrogen temperature

Line	Wavelength \AA	Energy cm^{-1}		Transition	SLJ
L_1	3533.2	28294	0	Z_2-L_2	
L_2	3527.6	28339	0		
L_3	3523.7	28371	0		
L_4	3504.7	28524	w,sh		
L_5	3502.2	28544	w,sh		
L_6	3468.4	28823	vw	Z_3-L_8	
L_7	3455.8	28928	0	Z_2-L_8	
L_8	3450.8	28970	0		
L_9	3399.9	29404	vw, sh	Z_2-L_{10}	
L_{10}	3383.0	29551			
M_1	3319.9	30112			
M_2	3310.0	30202		Z_2-M_3	$^2I_{13/2}$
M_3	3305.4	30,244			
Q_1	2978.4	33565	w,d	Z_2-Q_2	
Q_2	2974.4	33610	w,sh		$^2D_{5/2}$
Q_3	2971.6	33642	w,sh		
R_1	2907.2	34387			$^2H_{11/2}$
U_1	2536.6	39411	vw,sh		$^2F_{3/2}$

0 Overabsorbed. Line centre located from densitometer trace

w,v,w weak, very weak, sh sharp, d diffuse.

are listed in Table 4.2 along with the other levels determined from the present fluorescence data. The alphabetical (A-Z) nomenclature used in the table is the same as used by Dieke and co-workers². Table 4.1 also lists the SLJ designations of these various levels, made by a comparison of the spectrum with that obtained in LaCl_3 ^{2,3,4}. Most levels in this region are well separated from each other and a reliable one to one comparison is possible except for the L group (28,000 - 30,000 cm^{-1}) where several close lying levels are expected to occur.

The absorption spectrum recorded in the region 4000 - 9000 Å consists for the most part of severely overabsorbed lines on which no accurate wavelength measurements are possible. The spectrum however is in substantial agreement with that reported in the two earlier publications^{9,10} but for the presence of some extra lines.

The region of the spectrum where the extra lines are found, 4200 - 5800 Å is shown in figures 4.3 and 4.4. There is a group of faint lines around 4600 Å (figure 4.3) which are too weak to be measured on either the Abbe comparator or the microdensitometer. These may be due to the $^4\text{G}_{11/2}$ level predicted¹⁰ to occur at 21700 cm^{-1} . The sharp line at 4696 Å (21,288 cm^{-1}) occurring within the G group (figure 4.3) may be a missing Stark component of either of the two levels $^2\text{K}_{15/2}$ and $^2\text{G}_{9/2}$ constituting this group. Out of the 13 expected Stark levels only 8 are reported so far^{9,10}.

Table 4.2

The energy levels of $\text{Nd}^{3+}:\text{LaF}_3$

	SLJ	Stark level designation	current values ⁺	Earlier [*] values
Z	$4I_{9/2}$	Z_1	0	0
		Z_2	45	45
		Z_3	139	136
		Z_4	291	296
		Z_5	500	500
Y	$4I_{11/2}$	Y_1	1984	1978
		Y_2	2042	2037
		Y_3	2073	2068
		Y_4	2095	2091
		Y_5	2190	2187
		Y_6	2225	2223
X	$4I_{13/2}$	X_1	3921	3919
		X_2	3982	3979
		X_3	4039	4039
		X_4	4078	4078
		X_5	4121	4120
		X_6	4206	4213
		X_7	4279	4278

Table 4.2 (contd.)

SLJ		Stark level designation	current values ⁺	earlier [*] values
W	$4I_{15/2}$	W_1	5816	5817 ¹²
		W_2	5878	5876
		W_3	5990	5989
		W_4	6140	6142
		W_5	6171	6173
		W_6	6316	6320
		W_7	6447	6448
		W_8	6552	6551
R	$4F_{3/2}$	R_1		11592
		R_2		11634
S	$4F_{5/2}$	S_1	12596	12596
		S_2	12615	12613
		S_3	12622	12621
	$2H_{9/2}$	S_4	12676	12675
		S_5	12694	12693
		S_6	12753	12755
		S_7	12842	
		S_8	12904	

Table 4.2 (contd.)

	SLJ	Stark level designation	current values [†]	earlier [*] values
A	$4S_{3/2}; 4F_{7/2}$	A_1		13515
		A_2		13591
		A_3		13671
		A_4		13677
		A_5		13710
		A_6		13714
B	$4F_{9/2}$	B_1		14835
		B_2		14860
		B_3		14891
		B_4		14927
		B_5		14958
C	$2H_{11/2}$	C_1		15998
		C_2		16033
		C_3		16045
		C_4		16059
		C_5		16103
D	$4G_{5/2}; 2G_{7/2}$	D_1		17304
		D_2		17315
		D_3		17364
		D_4		17512

Table 4.2 (contd.)

SLJ		Stark level designation	current values ⁺	earlier values *
E	$4G_{7/2}$	D_5		17520
		D_6		17570
		D_7		17601
		E_1	19149	19147
		E_2	19238	19235
		E_3	19255	19251
		E_4	19322	19323
		F_1	19568 ^a	19568
		F_2	19612	19617
		F_3	19650	19651
F	$4G_{9/2}$	F_4	19679	19685
		F_5	19704	19702
		F_6	19739	19739
		F_7		19801
		F_8	19831	19839
		G_1	21156 ^a	21158
		G_2	21176	21176
		G_3	21202	21201
G	$2K_{15/2}; 2G_{9/2}$	G_4	21232	21234
		G_5	21252	21254

Table 4.2 (contd.)

SLJ		Stark level designation	current values ⁺	earlier [*] values
		G_6		21302
		G_7	21343	21339
		G_8	21356	21351
I	$^2P_{1/2}$	I_1	23470 ^a	23468
	$^2D_{5/2}$	I_2		23991
K	$^2(P,D)_{3/2}$	K_1	26364	
		K_2	26404	
L		L_2	28339 ^a	
		L_3	28370	
		L_4	28524	
		L_5	28544	
		L_8	28970	
		L_{10}	29551	
M	$^2I_{3/2}$	M_1	30111 ^a	
		M_3	30244	
Q	$^2D_{5/2}$	Q_2	33610 ^a	
		Q_3	33642	
R	$^2H_{11/2}$	R_1	34387 ^a	
U	$^2F_{3/2}$	U_1	39411 ^a	

⁺ The groups of levels marked 'a' are determined from the absorption spectrum. All other levels are determined from fluorescence.

^{*} The group of levels (w) marked '12' are from reference 12. All others from reference 10.

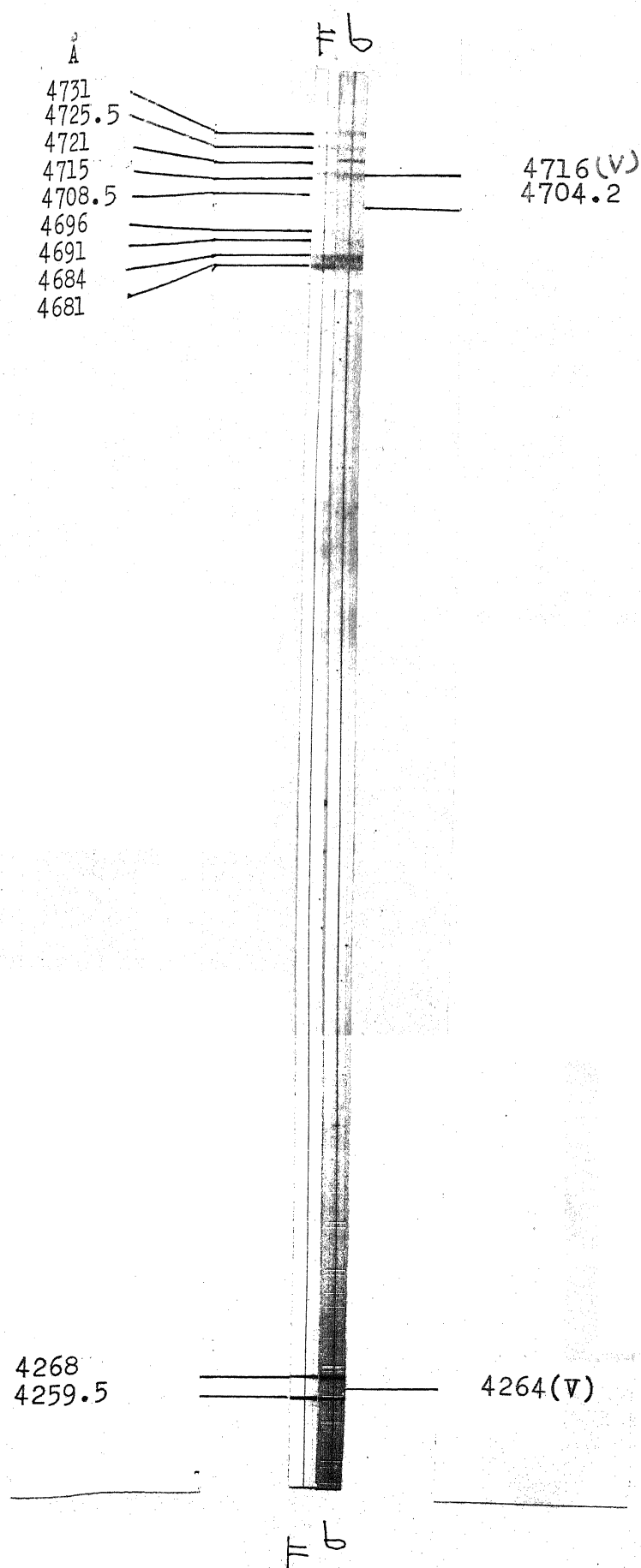


Fig. 4.3 $\text{Nd}^{3+}:\text{LaF}_3$ absorption spectrum at 77°K, 4100-4700Å.

The lines marked 'V' are probably vibronic in origin.

See text.

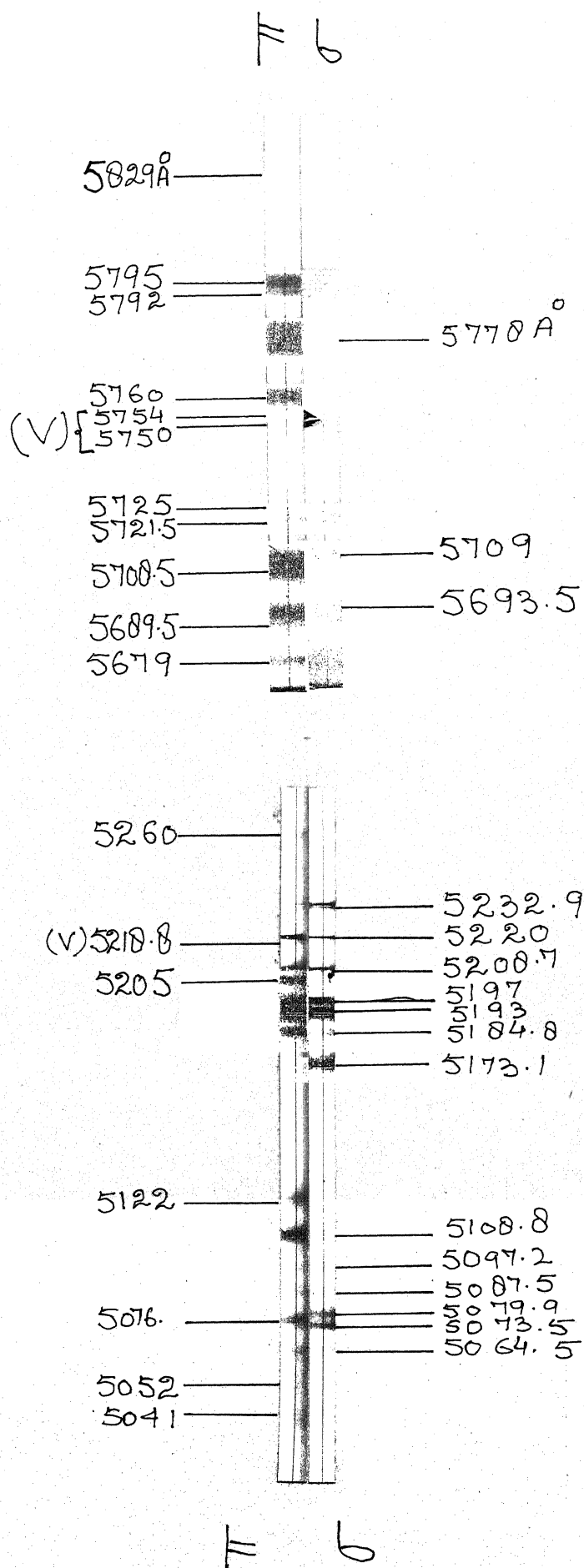


Fig. 4.4 $\text{Nd}^{3+}:\text{LaF}_3$ absorption spectrum at 77°K , 4800-5750 Å.

The lines marked 'V' are probably vibronic in origin.

See text.

The remaining four extra lines at 4264\AA (23445 cm^{-1}); 5218.8\AA ($19,156\text{ cm}^{-1}$); 5750 cm^{-1} ($17,386\text{ cm}^{-1}$) and 5754.0\AA ($17,374\text{ cm}^{-1}$) are however of a different kind. These occur within the I,E and D groups respectively. All the expected numbers of Stark components of the SLJ levels constituting these groups are already observed. So these are not missing Stark components. A possibility is that they belong to Nd^{3+} which (somehow) experience a slightly different crystal field than the rest. The EPR spectrum of Nd^{3+} in the crystal (chapter 5) however did not show any lines attributable to such centres. Another possibility is that they are vibronic lines. The 25 cm^{-1} separation of the 4264\AA line from the neighbouring 4259.5\AA line of $^2P_{1/2}$ (single Stark level expected) is quite close to the phonon frequency of 26 cm^{-1} observed by Yen, Scott and Shawlow¹⁴ in the fluorescence spectrum of $\text{Pr}^{3+}:\text{LaF}_3$. The other 3 lines however occur in regions where there are several Stark levels close by and it is not possible to tell the possible phonon energy associated with those lines. Thus for lack of any other explanation, these four extra lines are thought of as vibronic in origin.

Most of the lines observed (including the extra lines) are polarized, and the present observations tally with earlier observations of Wong et.al⁹ in the region where the two studies overlap ($5000 - 8700\text{\AA}$). Lines due to a Kramers' ion like Nd^{3+} experiencing orthorhombic crystal fields are not expected to be polarized (chapter 3). This point is discussed in a greater detail in section 4.7.

4.3 The Fluorescence Spectrum at LNT

The fluorescence spectrum of $\text{Nd}^{3+}:\text{LaF}_3$ observed here extends all the way from 3500 to 9100Å. Figures 4.5 and 4.6 illustrate the plates taken with Nitrogen laser (3371Å; 29656 cm^{-1}) excitation and figures 4.7 through 4.15 the fluorescence obtained with the Argon ion laser (5145Å; 19,431 cm^{-1}) excitation. The numbers marked in the figures are wavelengths in Å. In the various studies made on Nd^{3+} doped in various lattices⁴, so far, only the infrared fluorescence due to the R level ($^4\text{F}_{3/2}$, 11,600 cm^{-1}) is reported, with the single exception of LaCl_3 ² where fluorescence was observed from several levels below 28,000 cm^{-1} . In fact, with the Ar^+ laser excitation, some initial recordings made here using the cooled 7102 photomultiplier tube showed only the R-Z (8600-9100Å) fluorescence with adequate intensity. The visible fluorescence is recorded with such a poor signal to noise ratio that its existence could be just detected. CRB¹⁰ who used a high pressure mercury arc for excitation and the cooled 7102 tube for detection, might well have not found it as the fluorescence obtainable with conventional sources would be usually weaker than with a laser source.

The 5145Å (19,431 cm^{-1}) radiation available from the Ar^+ laser excites Nd ions primarily into the E levels (figure 4.1). The 5017Å (19,927 cm^{-1}), 4965Å (20,135 cm^{-1}), 4880Å

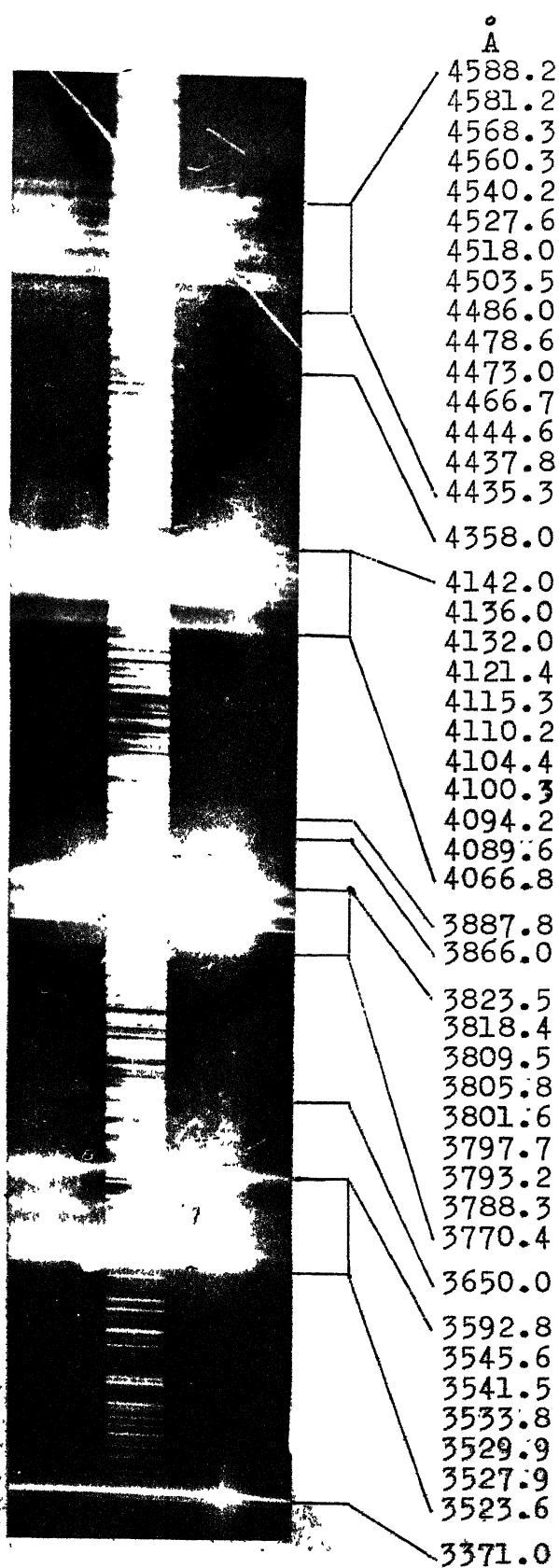


Fig. 4.5 $\text{Nd}^{3+}:\text{LaF}_3$ fluorescence at 77°K, 3400-5000Å, obtained with 3371Å excitation.

Four weak lines at 4866.25, 4907.9, 4985.7 and 5019.0Å could not be reproduced in print and hence not shown here.

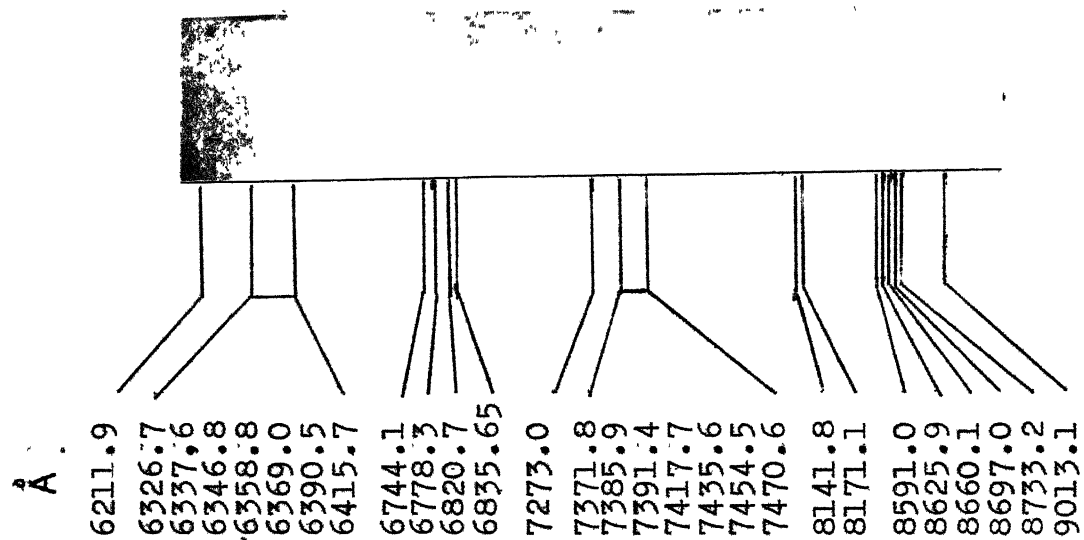


Fig. 4.6 $\text{Nd}^{3+}:\text{LaF}_3$ fluorescence at 77° K, 6000-9000Å; obtained with 3371Å excitation.

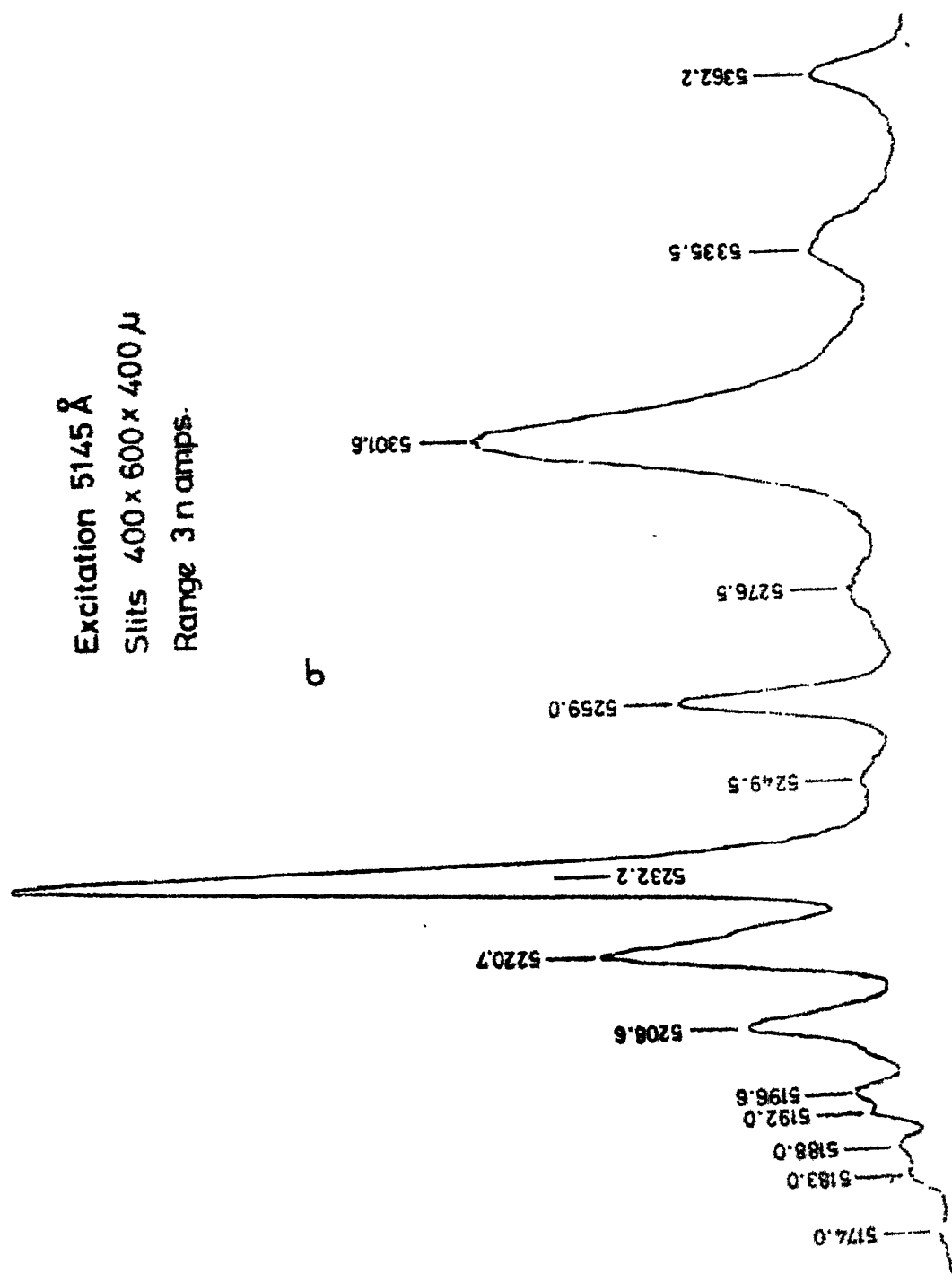


Fig. 4.7a The E-Z fluorescence at LNT, σ polarization.

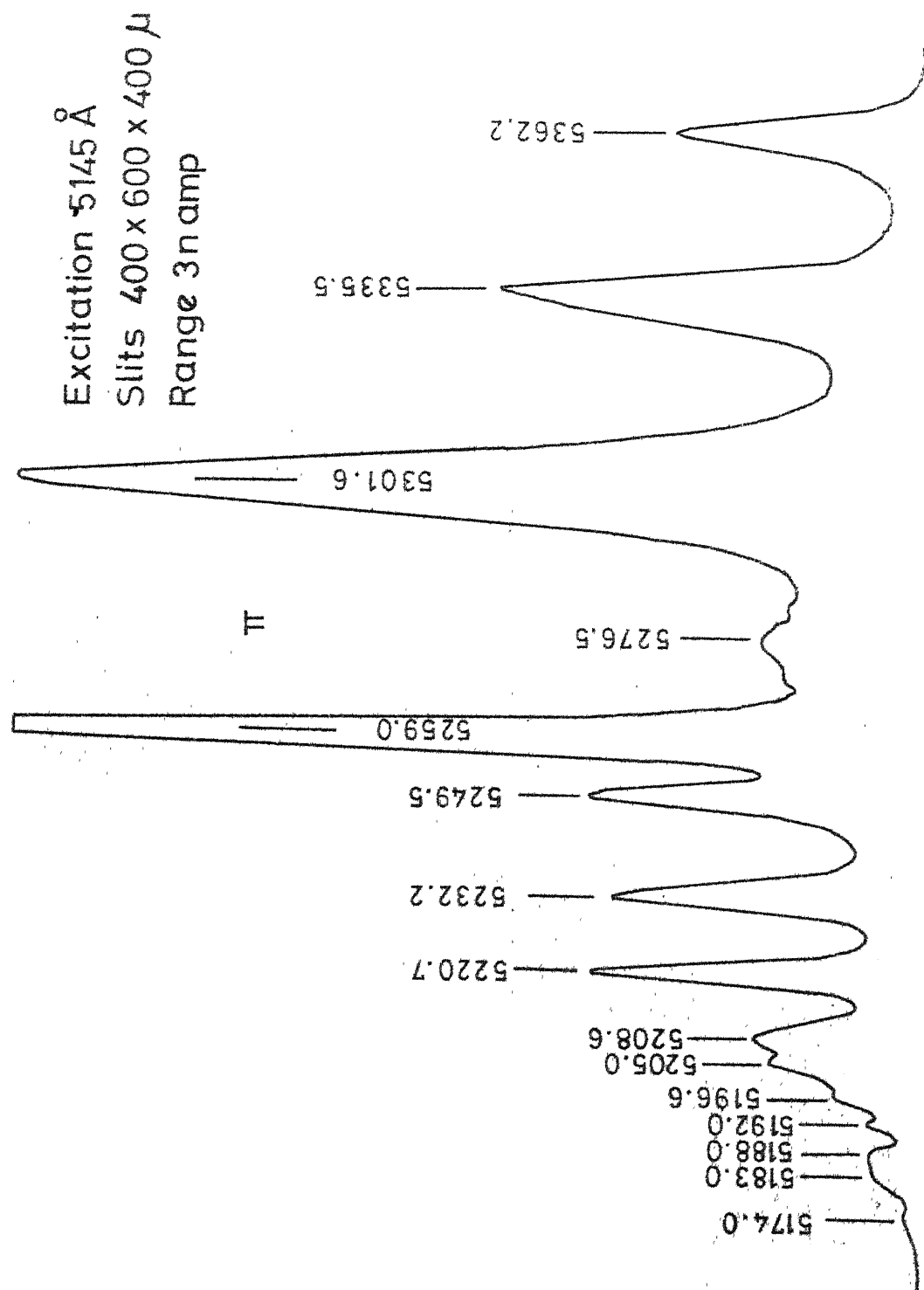


Fig. 4.7b The E-Z fluorescence at LNT π polarization.

Excitation 5145 Å, 100 mW
 Slit width 100 μ
 Range 0.3 nm/nm
 PMT voltage 1400 V

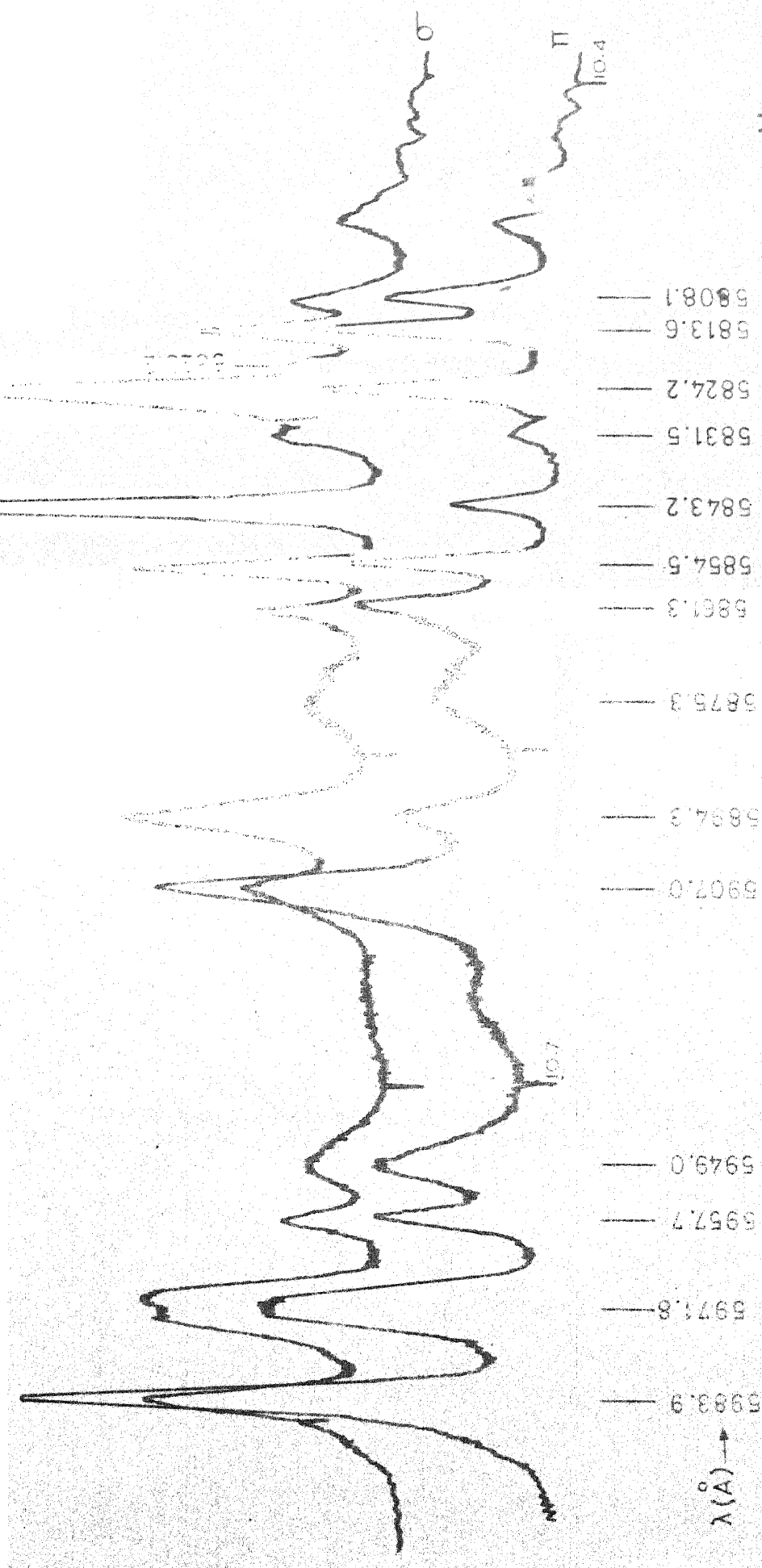


Fig. 4.8 Nd³⁺:LaF₃ fluorescence at 77°K, E(⁴G_{7/2}) → V(⁴I_{11/2}) group; 5145 Å

Excitation 5145 Å, 600 mw
PMT voltage 1260 V

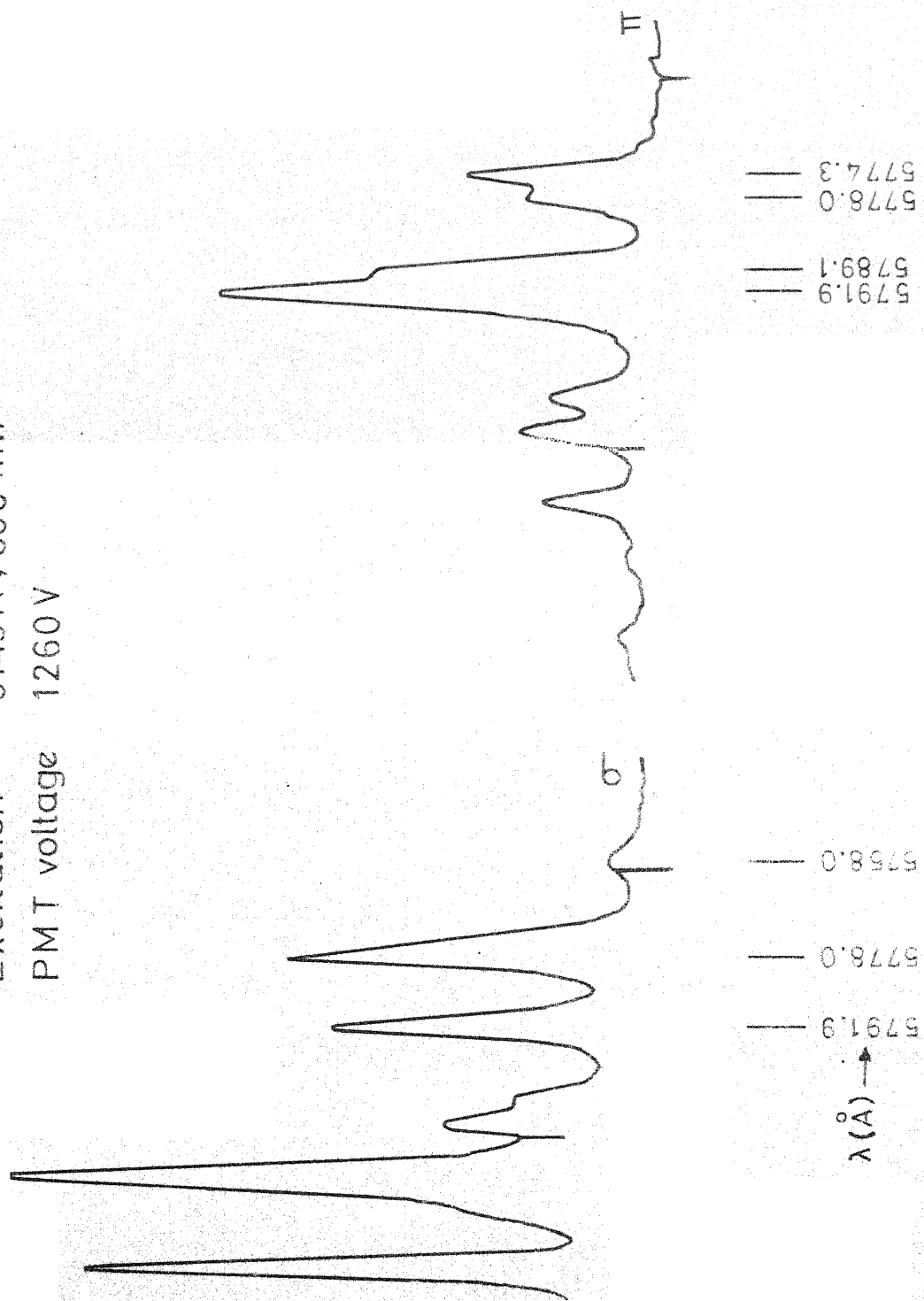


Fig.4.9 Nd³⁺:LaF₃ fluorescence at 77°K, D → Z(⁴I_{9/2}) group; 5145 Å excitation

Excitation 5145 \AA , 100 mw

Slit width 100μ

Range 30 n amp

PMT voltage 1250 V

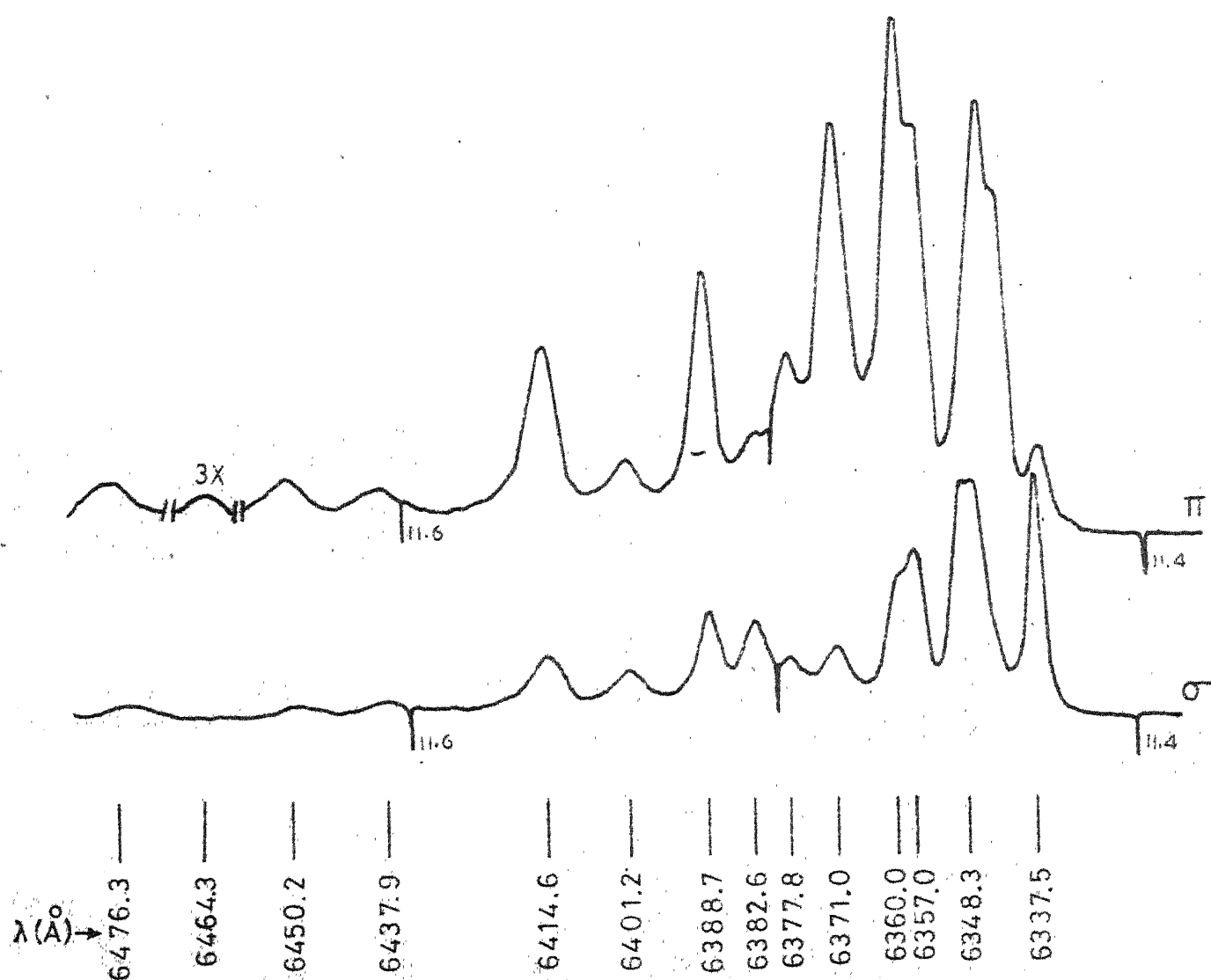


Fig.4.10 $\text{Nd}^{3+}:\text{LaF}_3$ fluorescence at 77°K , L \rightarrow S group;
 5145 \AA excitation.

Excitation 5145 Å, 700 mw
 Slit width 100 μ
 Range 10 n amp
 PMT voltage 1250 V

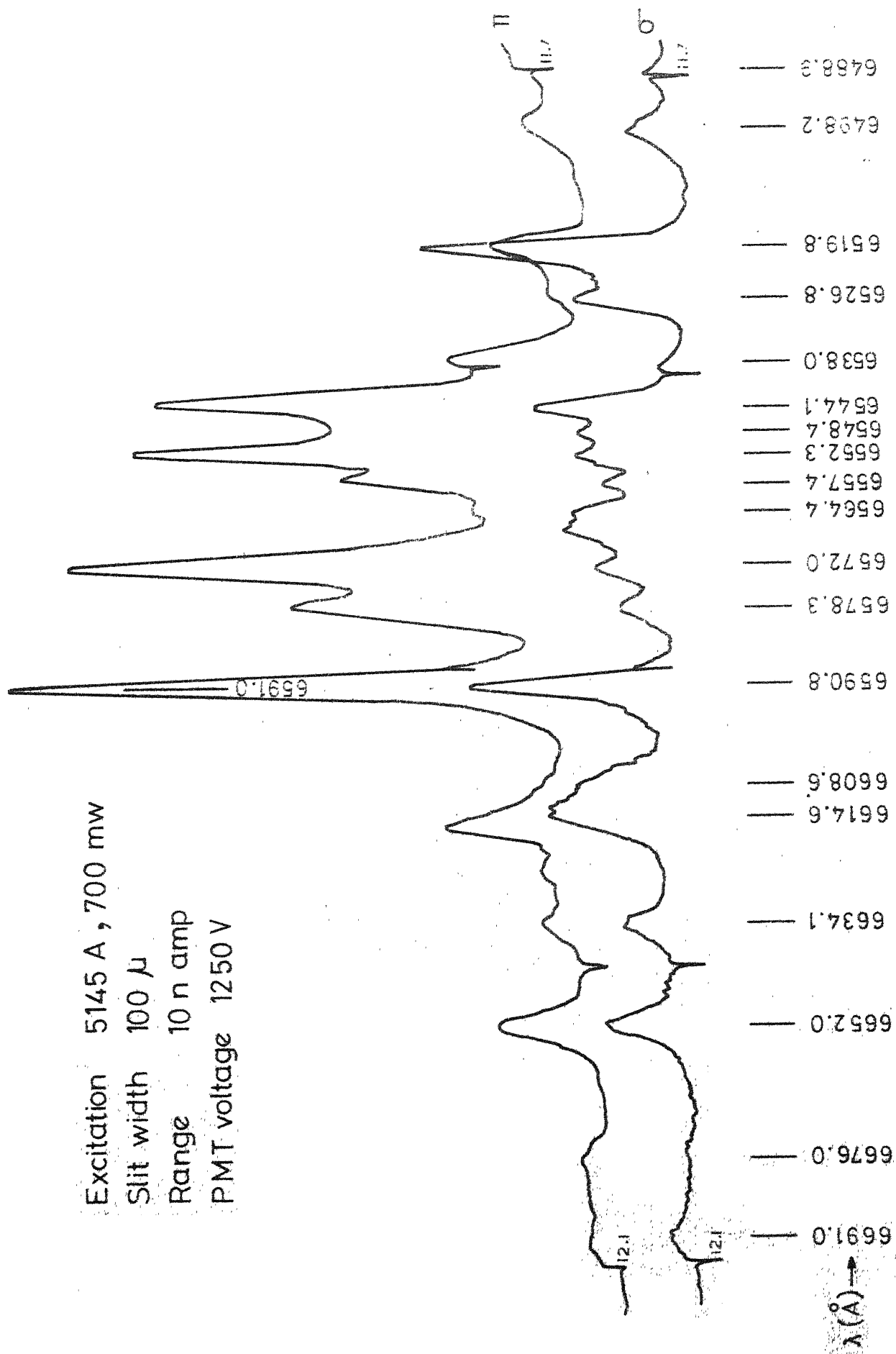


Fig.4.11 $3^+ \text{Nd}:\text{LaF}_3$ fluorescence at 77°K, $E(^4G_{7/2}) \rightarrow X(^1I_{13/2})$ group; 5145 Å excitation.

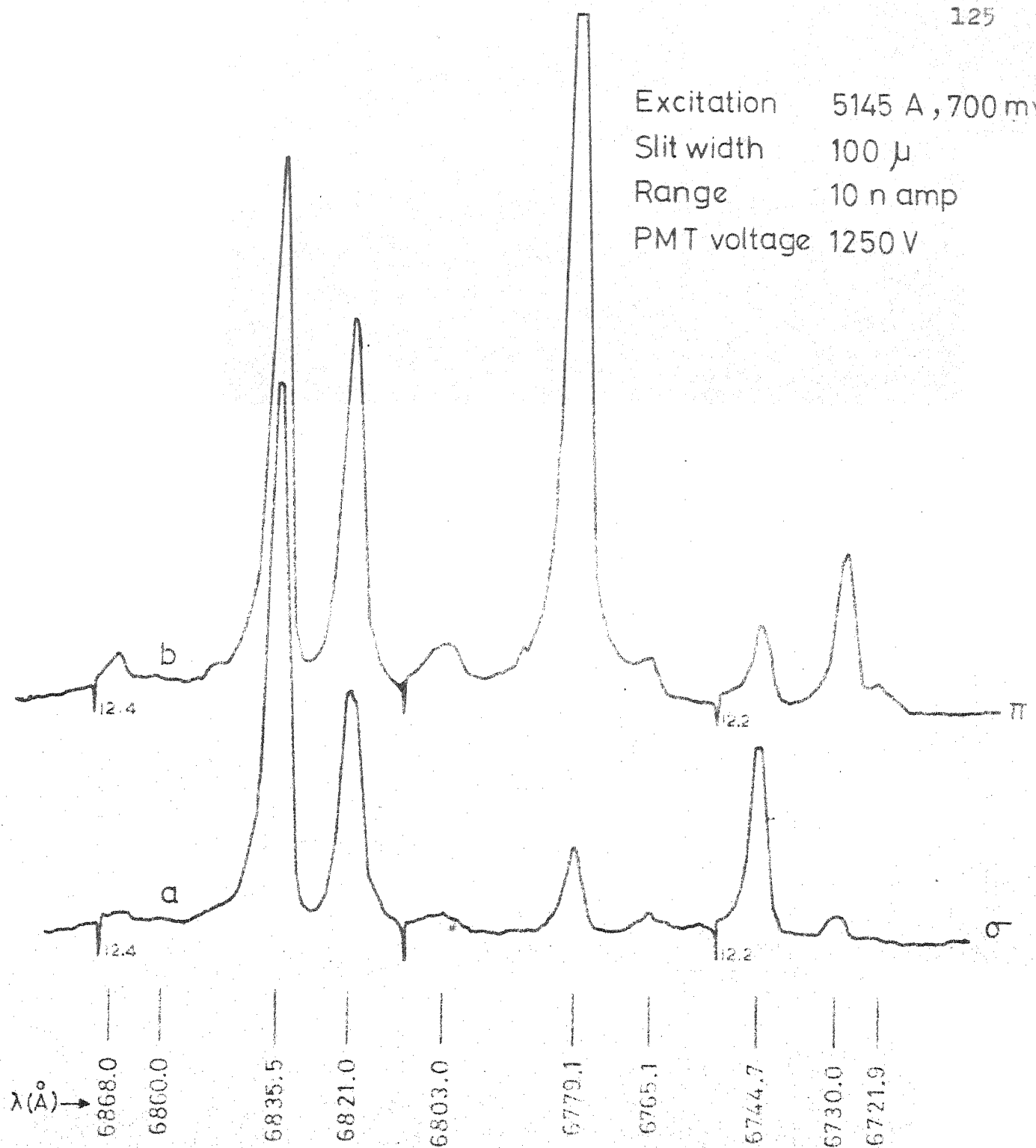


Fig. 4.12 $\text{Nd}^{3+}:\text{LaF}_3$ fluorescence at 77°K,
 L-A group; 5145Å excitation.

Excitation 5145 Å, 700 mw
 Slit width 100 μ
 Range 3 n amps
 PMT voltage 1250 V

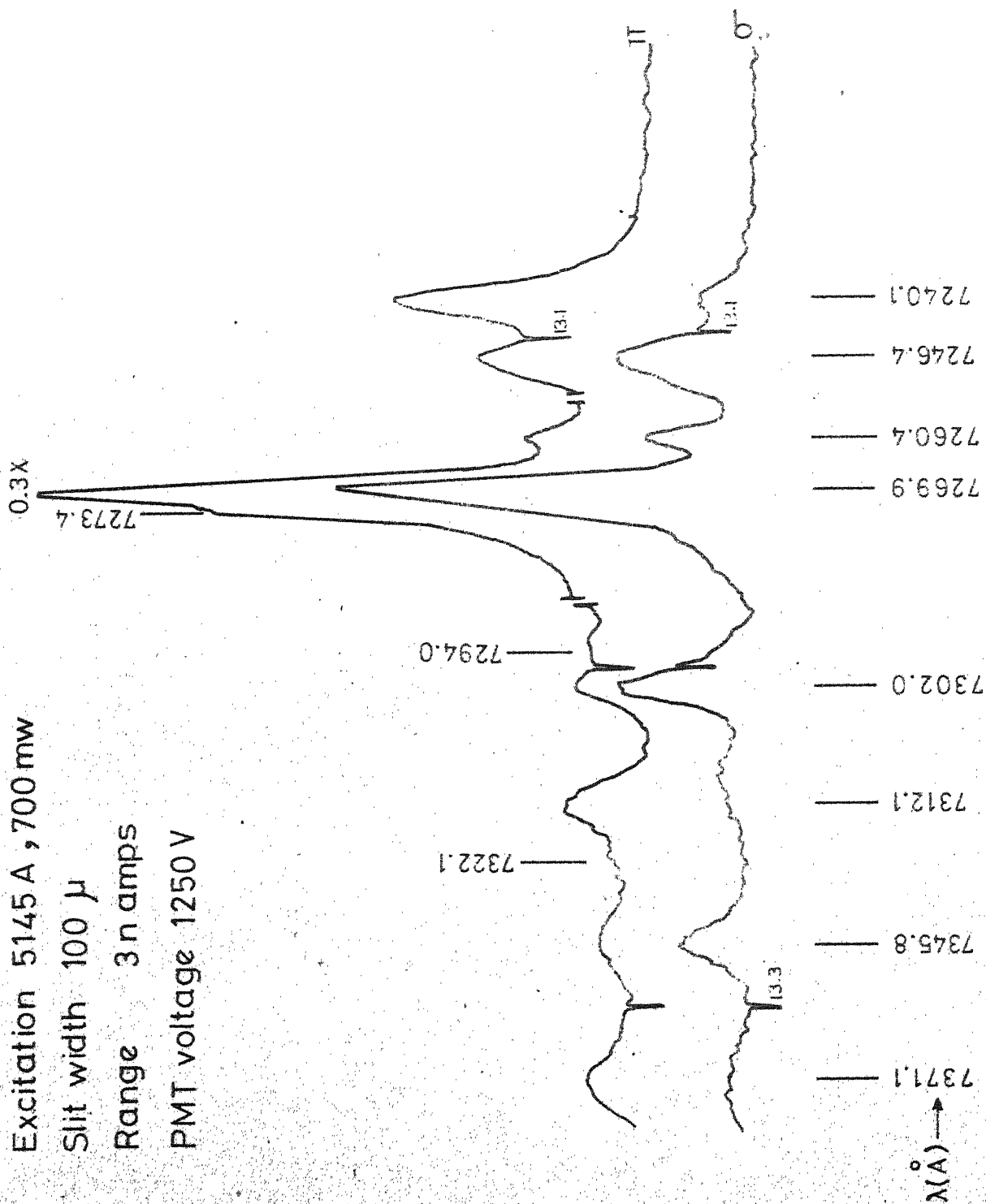


Fig. 4.13 $\text{Nd}^{3+}:\text{LaF}_3$ fluorescence at 77°K, K \rightarrow S group; 5145 Å excitation.

Excitation 5145 Å, 700 mw
 Slit width 100 μ
 Range 3 n amp

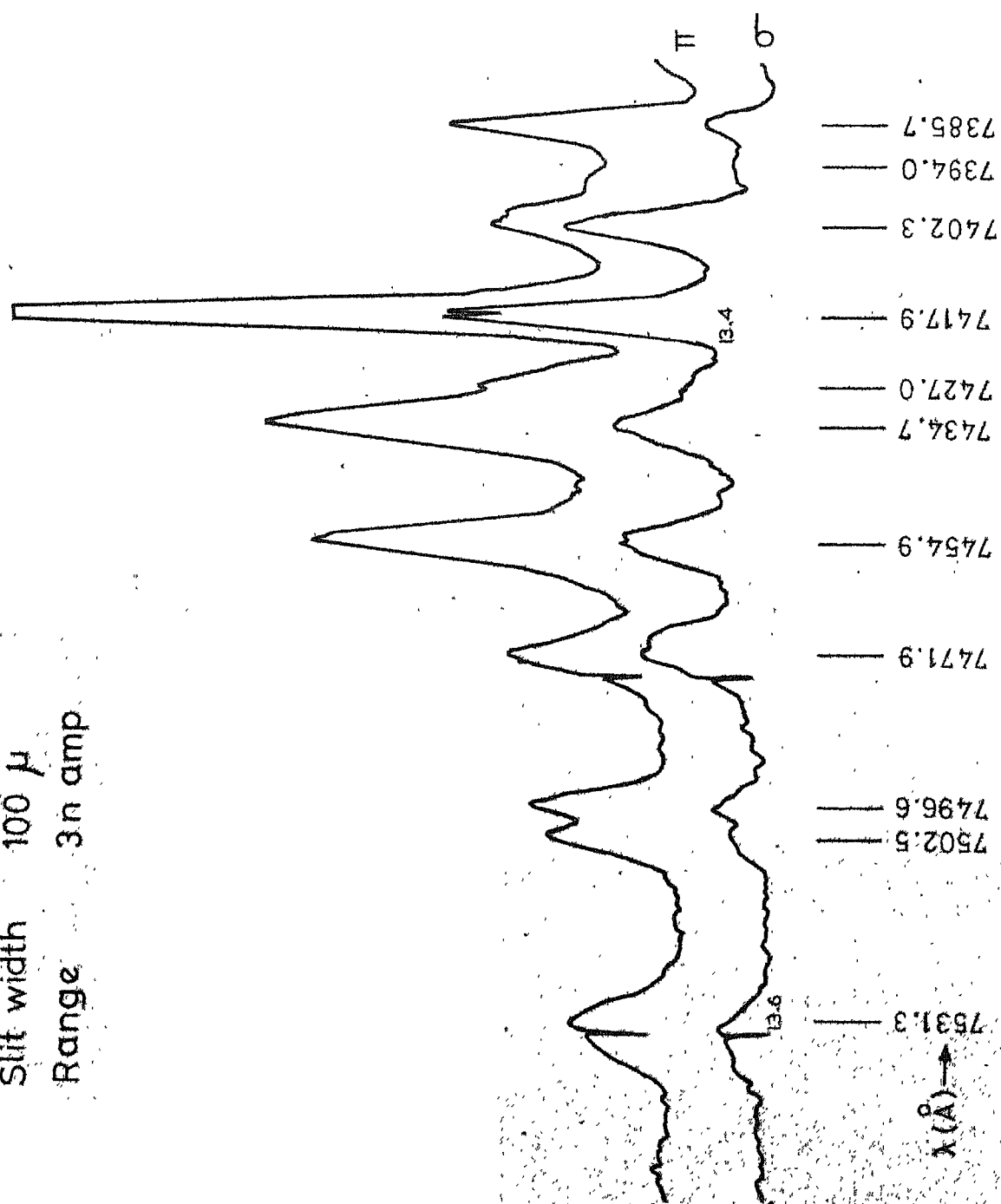


Fig. 4.14 $\text{Nd}^{3+}:\text{LaF}_3$ fluorescence at 77°K, $\text{L} \rightarrow \text{B} (^4\text{F}_{9/2})$ group;
 5145 Å excitation.

Excitation 5145 Å, 500 mw
 Slit width 100 μ
 Range 10 n amp
 PMT voltage 1260 V

a. $x = 0.24$ cm

b. $x = 0.084$ cm

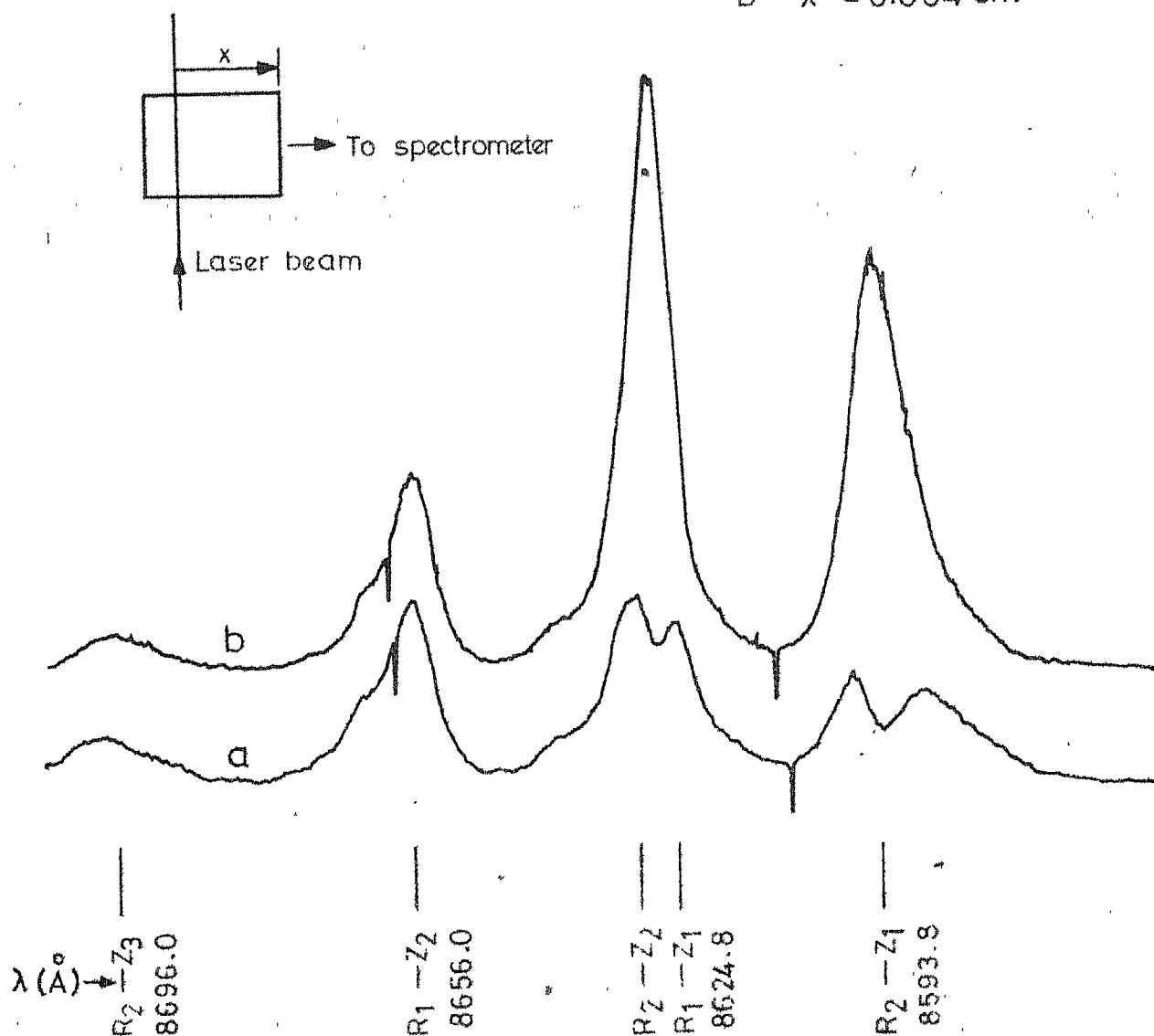


Fig. 4.15 $Nd^{3+}:LaF_3$ fluorescence at 77°K, part of the $R(^4F_{3/2}) \rightarrow Z(^4I_{3/2})$ group in σ polarization, showing self-absorption, 5145 Å excitation.

($20,486\text{ cm}^{-1}$) and 4765\AA ($20,980\text{ cm}^{-1}$) all would populate the F level but very likely, ions in F would decay non-radiatively to the E which is only 250 cm^{-1} below it (chapter 1). No fluorescence is in fact observed from this level. The three shortest wavelengths available from this laser, namely 4727\AA ($21,149\text{ cm}^{-1}$), 4658\AA ($21,462\text{ cm}^{-1}$) and 4580\AA ($21,832\text{ cm}^{-1}$) can be expected to yield fluorescence from the G levels. However in the present case, use of any excitation of shorter wavelength than 4765\AA at LNT and 4880\AA at RT resulted in very strong fluorescence from the $^3\text{P}_0$ level¹⁵ of Pr^{3+} (which is present in the crystal in small quantities as an unintentional codopant). This completely masked the Nd^{3+} fluorescence which is much weaker. The presence of Pr^{3+} is detected as in the earlier case (chapter 3, $\text{Eu}^{3+}:\text{LaF}_3$) by comparison with the fluorescence spectrum of $\text{Pr}^{3+}:\text{LaF}_3$ recorded by P. Venkateswarlu at Santa Barbara. All of the present work is thus carried out using the 5145\AA excitation as the intensity of fluorescence obtained with this is one or two orders of magnitude larger than with the other excitations and does not contain any interfering lines.

The spectrum obtained (5145\AA excitation) is presented in figures 4.7 through 4.15 and contains nine groups of lines. Four of these groups present in charts recorded here as well at Santa Barbara, are easily identified as due to (E-Z), (E-Y),

Table 4.3

The fluorescence spectrum of $\text{Nd}^{3+}:\text{LaF}_3$ at LNT
 obtained with 5145\AA (Ar^+) excitation

Wavelength (\AA)	Energy (cm^{-1})	Polarization		Transition Assignment
		σ	π	
5169.0	19341			Raman
5174.0*	19322	w	w	$E_4 - Z_1$
5183.0	19288	w	w	Raman
5188.0	19270	w	w	Raman
5192.0	19255	w	w	$E_3 - Z_1$
5196.6	19238	w	w	$E_2 - Z_1$
5205.0	19207	w	w	$E_3 - Z_2$
5208.6	19194	w	w	$E_2 - Z_2$
5220.7	19149	3.7	3.7	$E_1 - Z_1$
5232.2	19107	10.0	3.0	$E_1 - Z_2$
5242.6	19069			Raman
5249.5	19044			Raman
5259.0	19009	3.0	12.0	$E_1 - Z_3$
5276.5	18947	0.5	0.5	$E_2 - Z_4$
5301.6	18857	5.0	9.5	$E_1 - Z_4$
5335.5	18737	0.9	4.0	$E_2 - Z_5$
5362.2	18644	1.0	3.0	$E_1 - Z_5$

Table 4.3 (continued)

Wavelength (Å)	Energy (cm ⁻¹)	Polarization		Transition Assignment
		σ	π	
5758.0	17362	0.6		D ₃ — Z ₁
5774.3	17313		5.3	D ₂ — Z ₁
5778.0	17302	6.2	3.6	D ₁ — Z ₁
5789.1	17269		7.8	D ₂ — Z ₂
5791.0	17263	5.4	12.0	D ₁ — Z ₂ , E ₄ — Y ₃ ; E ₂ — Y ₁
5808.1	17212	2.3	3.1	E ₃ — Y ₂
5813.6	17196	4.1	4.4	E ₂ — Y ₂
5820.2	17177	w		D ₂ — Z ₃
5824.2	17165	9.6	4.4	D ₁ — Z ₃ , E ₃ — Y ₄ ; E ₂ — Y ₃ ; E ₁ — Y ₁
5831.5	17143	w	w	E ₂ — Y ₄
5843.2	17109	12.6	2.0	E ₁ — Y ₂
5854.5	17076	5.4	3.7	E ₁ — Y ₃
5861.3	17056	3.5	3.7	E ₁ — Y ₄
5875.3	17016	1.8	2.5	E ₂ — Y ₆ , D ₄ — Z ₅ ; D ₅ — Z ₅
5894.3	16961	5.4	3.0	E ₁ — Y ₅
5907.0	16924	2.9	7.0	E ₁ — Y ₆
5949.0	16805	1.9	3.0	D ₁ — Z ₅
5957.7	16780	2.4	3.0	L ₃ — R ₁
5971.8	16741	5.3	5.0	L ₃ — R ₂ , L ₂ — R ₁
5983.9	16707	5.1	8.5	L ₂ — R ₂

Table 4.3 (continued)

Wavelength (Å)	Energy (cm ⁻¹)	Polarization		Transition Assignment
		σ	π	
6337.5	15775	4.3	0.8	$L_3 - S_1$
6348.3	15748	4.2	6.0	$L_3 - S_2$; $L_3 - S_3$, $L_2 - S_1$
6357.0	15726	3.0	6.5	$L_2 - S_2$
6360.0	15719	2.5	7.1	$L_2 - S_3$
6371.0	15692	0.6	5.5	$L_3 - S_4$
6377.8	15675	0.3	0.5	$L_3 - S_5$
6382.6	15663	1.4	0.3	$L_2 - S_4$
6388.7	15648	1.7	3.6	$L_2 - S_5$
6401.2	15618	0.6	0.5	$L_3 - S_6$
6414.6	15585	0.8	2.5	$L_2 - S_6$
6437.9	15529	0.3	0.3	$L_3 - S_7$
6450.2	15499	0.2	0.5	$L_2 - S_7$
6464.3	15465		0.1	$L_3 - S_8$
6476.3	15437	0.3	0.5	$L_2 - S_8$
6488.9	15407	1.0	0.5	$E_4 - X_1$
6498.2	15385	1.6	0.8	?
6519.8	15334	7.1	1.5	$E_3 - X_1$
6526.8	15317	3.1	0.6	$E_2 - X_1$
6538.0	15291		2.5	$E_4 - X_3$
6544.1	15277	3.7	6.8	$E_3 - X_2$

Table 4.3 (continued)

Wavelength (Å)	Energy (cm ⁻¹)	Polarization		Transition Assignment
		σ	π	
6548.4	15267	w		?
6552.3	15258		8.0	E ₂ — X ₂
6557.4	15246		4.2	E ₄ — X ₄
6564.4	15229	3.5	w	E ₁ — X ₁
6572.0	15212	2.5	8.0	E ₃ — X ₃
6578.3	15197	1.8	5.0	E ₂ — X ₃
6590.8	15168	5.5	9.0	E ₁ — X ₂
6608.6	15128	3.6		E ₃ — X ₅
6614.6	15114	4.5		E ₂ — X ₅
6634.1	15069	2.4	0.8	E ₁ — X ₄
6652.0	15029	2.8	1.8	E ₁ — X ₅
6676.0	14975		w	E ₃ — X ₇
6691.0	14941	1.0		E ₁ — X ₆
6721.9	14873	0.5	0.5	E ₁ — X ₇
6730.0	14855	0.6	2.9	L ₃ — A ₁
6744.7	14822	4.5	1.5	L ₂ — A ₁
6765.1	14778	0.4	0.3	L ₃ — A ₂
6779.1	14747	2.0	12.0	L ₂ — A ₂
6803.0	14695	0.4	0.7	L ₃ — A ₃ ; L ₃ — A ₄
6821.6	14655	5.2	6.5	L ₃ — A ₆ ; L ₃ — A ₅
6835.5	14625	12.5	9.5	L ₂ — A ₆ ; L ₂ — A ₅
6860.0	14573	w	w	?
6868.0	14556	w	0.5	?

Table 4.3 (continued)

Wavelength (Å)	Energy (cm ⁻¹)	Polarization		Transition Assignment
		σ	π	
7240.1	13808	0.6	4.2	K ₂ — S ₁
7246.4	13796	2.8	2.8	K ₂ — S ₂
7260.4	13769	1.6	1.5	K ₁ — S ₁
7269.9	13751	8.4	3.1	K ₁ — S ₂
7273.4	13745		w	K ₁ — S ₃
7294.0	13706		w	K ₂ — S ₅
7302.0	13691	2.5	1.3	K ₁ — S ₄
7312.1	13672	0.4		K ₁ — S ₅
7322.1	13653		1.5	K ₂ — S ₆
7345.8	13609	1.3	0.6	K ₁ — S ₆
7371.1	13563	0.4	0.7	K ₂ — S ₇
7385.7	13536	1.4	3.8	L ₂ — B ₅
7394.0	13521	w	w	K ₁ — S ₇
7402.3	13505	3.9	3.0	L ₂ — B ₅ , L ₃ — B ₂
7417.9	13477	6.0	11.0	L ₃ — B ₃ , L ₂ — B ₄
7427.0	13461	w	w	K ₁ — S ₈
7434.7	13447	3.0	6.5	L ₃ — B ₂ , L ₂ — B ₃
7454.9	13410	2.9	5.8	L ₃ — B ₅ , L ₂ — B ₄
7471.9	13380	2.6	2.8	L ₂ — B ₅
7496.6	13336	1.2	2.5	?
7502.0	13326	1.0	2.3	?
7531.0	13275	1.1	1.9	?

Table 4.3 (continued)

Wavelength (Å)	Energy (cm ⁻¹)	Polarization		Transition Assignment
		σ	π	
8593.8	11633	11.2	2.6	$R_2 - Z_1$
8624.8	11591	14.4	17.0	$R_1 - Z_1, R_2 - Z_2$
8637.5	11574	w	w	$K_2 - B_1$ (?)
8656.0	11549	4.0	8.2	$R_1 - Z_2$
8663.3	11540	w	w	$K_2 - B_2$ (?), $K_1 - B_1$ (?)
8696.0	11496	1.0	1.8	$R_2 - Z_3$
8729.0	11453	1.7	0.6	$R_1 - Z_3$
8813.0	11344		1.1	$R_2 - Z_4$
8846.0	11301	0.4	0.2	$R_1 - Z_4$
8978.0	11135		0.3	$R_2 - Z_5$
9013.0	11092	0.4	0.3	$R_1 - Z_5$

* Wavelengths and intensities of the lines of E-Z group are from recordings made at Santa Barbara.

^w Line weak Intensity not measurable either due to poor S/N or overlap.

for larger distances (see section 4.5). This is evident from figures 4.8 and 4.9.

The remaining four groups of lines (figures 4.10,12, 13,14) could not however be identified that easily. Again these are recorded here by the author only. They are not present in the charts recorded at Santa Barbara. At the first instance it ^{is} ~~is~~ thought that they are due to some unusually strong spontaneous emission from the Ar^+ laser used^φ. Such spurious emission as may be present is sought to be eliminated by the introduction of a band pass filter (Corning No. C.S. 4-97) and later a 0.25 m grating monochromator (Jarrell-Ash) in the laser beam. This resulted only in a decrease in their relative intensity in comparison with the other groups (E-X for example). Thus the laser as the origin is ruled out. The above observation however prompted a study of the variation of the intensity with power. Figure 4.16 is a plot of the variation on a log-log scale for two of the lines 5973.3\AA and 7270.0\AA . These plots show $I \propto P^{1.76}$. This means that the fluorescence is originating in levels that are probably populated by a two photon absorption (this is discussed more fully in section 4.4). A search made among the higher energy levels of Nd^{3+} consequently lead to the identification of the levels at $28,339$ and 28371 cm^{-1} (L_2 and L_3 , Table 4.1) as the originating levels for three of these groups. These are L-S,

^φ It is checked and found that they cannot be due to $\text{Pr}^{3+}\text{LaF}_3$

L-A and L-B transitions. Also the three lines found on the high wavelength side of the E-Y transition (not found in Santa Barbara recordings) are identified as L-R transitions.

The group identified as due to the L-S transitions; 6330-6480Å, (figure 4.10) actually contains four more lines than can be accounted for by the transitions to the six Stark components of this group determined so far. The two levels $4F_{5/2}$, $2H_{9/2}$ which make up this group must split however into eight Stark components. The extra four lines can be adequately accounted for if they are understood to be the transitions from L_2 and L_3 to two more Stark components at 12841 and 12904 cm^{-1} .

The remaining group between 7240Å and 7370Å (figure 4.13) however could not be explained as originating in any of the levels of Nd^{3+} that are determined from the absorption spectrum (present as well as earlier work). A procedure similar to the one adopted to locate the lower levels of Eu^{3+} (chapter 3) is therefore used to find the upper levels. It is however a matrix of the 'sums' of the energies of the possible lower levels and the observed fluorescence lines that is made in this case. A consistently repeating number in this matrix is a possible upper energy level. Table 4.4 shows such a matrix constructed taking the S group of Stark levels as lower levels. The first column of the table lists the

Table 4.4

The 'Sum' matrix for the 7200 \AA group of fluorescence
lines and the 'S' group of Stark levels

Observed lines	S ₁ 12596	S ₂ 12613	S ₃ 12621	S ₄ 12675	S ₅ 12693	S ₆ 12755	S ₇ 12841	S ₈ 12904
13808	26404 ¹	26417 ¹	26429	26483	26501	26563	26649	26712
795	391	408 ¹	416	470	488	550	636	699
769	365 ²	382	390	434	462	524	610	673
751	347	364 ²	372	426	444	506	592	655
744		357	365 ²	419	437	499	585	648
706		319	327	381	399 ¹	461	547	610
691		304	312	366 ²	386	446	532	595
672		285	293	346	365 ²	327	513	576
653			274	325	346	408 ¹	494	557
609			230	284	302	364 ²	450	513
562			183	237	255	317	403 ¹	466
520			141	195	213	275	364 ²	424
460			081	135	153	215	301	364 ²

Note: The superscripts indicate sets of matching numbers.

energies in cm^{-1} of the observed transitions. The first row has the energies of the Stark manifold S. The repetition of the two numbers 26404 ± 4 and $26365 \pm 1 \text{ cm}^{-1}$ is quite convincing and are thus taken to be the positions of the upper levels responsible for this fluorescence⁺. These Stark levels most likely belong to the isolated $^2(\text{P,D})_{3/2}$ level expected in this region (figure 4.1). Other such sum tables made using various other levels below $24,000 \text{ cm}^{-1}$ as lower levels did not produce any consistent upper level positions. This group is thus assigned as due to the K — S transitions. It may be noted here that the transitions to the 12841 and 12904 cm^{-1} levels of S are observed in this group also, confirming the earlier supposition.

Confirmatory evidence for these assignments is obtained from the fluorescence obtained with the nitrogen laser excitation shown in figures 4.5 and 4.6. The spectrum contains many groups of lines all the way from 3500 to 9000\AA . Table 4.5 lists the observed lines and their assignments. Transitions from L_2 and L_3 to nine lower levels (Z,Y,X,W...C) of Nd^{3+} are identified in these plates, as well as transitions to the Y,X,W and S levels from the K level whose position is derived from the Ar^+ laser excited fluorescence. Because of the small dispersion available in the spectrographs used (Q24, three prism, chapter 2) the wavelengths measured are

⁺ The author has found two isolated lines at 26,311 and 26,356 cm^{-1} in the absorption spectrum of NdF_3 , the study of which is not yet complete.

Table 4.5

The fluorescence spectrum of $\text{Nd}^{3+}:\text{LaF}_3$ at LNT
 obtained with 3371\AA (N_2 laser) excitation

Wavelength \AA	Energy cm^{-1}		Transition assignment
3523.6	28372	m sh	$L_3 - Z_1$
3527.9	28337	w sh	$L_2 - Z_1$
3529.9	28321	m sh	$L_3 - Z_2$
3533.8	28290	st sh	$L_2 - Z_2$
3541.5	28228	m sh	$L_3 - Z_3$
3545.6	28193	m sh	$L_2 - Z_3$
3592.8	27825	st d	?
3650.0	27389	w d	Hg ?
3770.4	26515	w d	?
3788.3	26390	st sh	$L_3 - Y_1$
3793.2	26355	m sh	$L_2 - Y_1$
3797.7	26324	w sh	$L_3 - Y_2$
3801.6	26297	st sh	$L_2 - Y_2, L_3 - Y_3$
3805.8	26268	w sh	$L_2 - Y_3$
3809.5	26243	w sh	$L_2 - Y_4$
3818.4	26182	m d	$L_3 - Y_5$
3823.5	26147	st d	$L_2 - Y_5; L_3 - Y_6$

Table 4.5 (continued)

Wavelength Å	Energy cm ⁻¹		Transition assignment
3866.0	25859	w d	?
3887.8	25714	w d	?
4066.8	24582	st d	?
4089.6	24445	m sh	$L_3 - X_1$
4094.2	24418	m sh	$L_2 - X_1, K_2 - Y_1$
4100.3	24382	m sh	$K_1 - Y_1$
4104.4	24357	w sh	$L_2 - X_2$
4110.2	24323	m sh	$K_1 - Y_2$
4115.3	24293	w sh	$L_3 - X_4, K_1 - Y_3$
4121.4	24257	st sh	$L_3 - X_5$
4132 0	24195	w sh	?
4136 0	24171	w sh	$K_1 - Y_5$
4142 0	24136	st sh	$K_1 - Y_6$
4358 0	22940		Hg ?
4435.3	22540	w sh	
4437.8	22527	w sh	$L_2 - W_1$
4444.6	22493	w d	$L_3 - W_2$
4466.65	22382	m sh	$L_3 - W_3; K_1 - X_2$
4473.0	22350	w sh	$L_2 - W_3$
4478.6	22322	m sh	$K_2 - W_4$

Table 4.5 (continued)

Wavelength Å	Energy cm ⁻¹		Transition assignment
4486.0	22285	m sh	$K_2 - X_5$
4503.5	22199	m d	$L_3 - W_5, L_2 - W_4,$ $K_2 - X_6$
4518.0	22127	m d	$K_2 - X_7$
4527.6	22081	m d	$K_1 - X_7$
4540.2	22019	w d	$L_2 - W_6$
4560.3	21921	w d	$L_3 - W_7$
4568.3	21883	m d	$L_2 - W_7$
4581.2	21822	w sh	$L_3 - W_8$
4588.2	21789	m sh	$L_2 - W_8$
4866.25	20544	v w	$K_1 - W_1$
4907.9	20370	v w	$K_1 - W_3$
4985.7	20052	v w	$K_1 - W_6$
5019.0	19919	v w	$K_1 - W_7$
5970.3	16745	v w	$L_3 - R_2, L_2 - R_1$
5983.9	16707	v w	$L_2 - R_2$
6010.3	16634	st b	
6034.9	16566	w sh	
6211.9	16094	st b	
6326.7	15802	v w	

Table 4.5 (continued)

Wavelength Å	Energy cm ⁻¹		Transition assignment
6337.6	15775	w	L ₃ - S ₁
6346.8	15752	w b	L ₃ - S ₂ , L ₃ - S ₃ , L ₂ - S ₁
6358.8	15722	w sh	L ₂ - S ₃
6369.0	15697	w b	L ₃ - S ₄
6390.5	15644	m sh	L ₂ - S ₅
6415.7	15582	m sh	L ₂ - S ₆
6744.1	14824	v w	L ₂ - A ₁
6778.3	14749	m d	L ₂ - A ₂
6820.7	14657	m d	L ₃ - A ₅ ; L ₃ - A ₆
6835.65	14625	m d	L ₂ - A ₅ , L ₂ - A ₆
7273.0	13746	st b	K ₂ - S ₂ , K ₂ - S ₃
7371.8	13562	w sh	K ₁ - S ₇
7385.9	13536	w sh	L ₂ - B ₅
7391.4	13526	w sh	K ₂ - S ₇
7417.7	13478	w sh	L ₃ - B ₃ , L ₂ - B ₄
7435.6	13445	w sh	L ₃ - B ₂ ; L ₂ - B ₃
7454.5	13411	w sh	L ₃ - B ₁ ; L ₂ - B ₂
7470.6	13382	w sh	L ₂ - B ₁

Table 4.5 (continued)

Wavelength Å	Energy cm ⁻¹		Transition assignment
8141.8	12279	v w	
8171.1	12235	v w	
8591.0	11637	m b	R ₂ - Z ₁
8625.9	11590	st b	R ₁ - Z ₁ , R ₂ - Z ₂
8660.1	11544	st b	R ₁ - Z ₂
8697.0	11495	m b	R ₂ - Z ₃
8733.2	11447	m b	R ₁ - Z ₃
9013.1	11092	m b	R ₁ - Z ₅
<hr/>			
st	Strong	sh	Sharp
m	Moderate	d	Diffuse
w	Weak	vw	Veryweak

not very accurate. Also only the strongest of the lines observed with Ar^+ laser are recorded in these plates. There is however enough similarity in the groups observed in both cases.

The observation of as many as 19 groups of fluorescence lines offers a good opportunity of determining the energies of the Stark components of the lower levels with greater accuracy. This is particularly relevant for the ground state which is not directly observed in absorption. Tables 4.6 through 4.10 list these Stark level positions determined from the various observed transitions and the average values. For lines observed with the N_2 laser as well as Ar^+ laser, the values of the lower levels obtained from the latter spectrum are written in these tables as they are more accurate. The present values are seen to agree with earlier values within the experimental uncertainty ($\pm 5 \text{ cm}^{-1}$). Table 4.2 summarizes the data thus obtained about the energy level structure of $\text{Nd}^{3+}:\text{LaF}_3$ from its absorption and fluorescence spectra.

Table 4.6

Crystal field splitting of $^4I_{9/2}(Z)$ level of
 $Nd^{3+} \cdot LaF_3$ from the fluorescence data at LNT^Q

Upper Levels	Lower Levels				
	Z_1	Z_2	Z_3	Z_4	Z_5
R_1	σ	42 π	137 σ	290 σ	499 σ
R_2	σ		137 π	289 π	498 π
D_1	π				
D_2	π	44* π	136 σ		
D_3	σ				
E_1	$\sigma\pi$	42 σ	140 π	292 σ	505 π
E_2		44*		291 $\sigma\pi$	501 σ
E_3		48*			
L_2		47	142		
L_3		50	143		
Average		45	139	291	500
Reference 10		45	136	296	500

^Q Almost all lines are partially polarized. Only the polarization in which the line is stronger is given in the table.

* Uncertain due to overlaps. Not used for averaging.

Table 4.7

Crystal field splittings of $^4I_{11/2}$ (γ) level of
 $\text{Nd}^{3+}:\text{LaF}_3$ from the fluorescence data at LNT^②

Upper Level	Lower Levels					
	γ_1	γ_2	γ_3	γ_4	γ_5	γ_6
E_1		2040 $\sigma\pi$	2073 σ	2093 $\sigma\pi$	2188 σ	2226* π
E_2		2042 $\sigma\pi$		2095		2222 $\sigma\pi$
E_3		2042 $\sigma\pi$				
K_1	1983	2041	2072		2193	2228
K_2	1986					
L_2	1985	2042*	2072	2097	2193*	
L_3	1982	2047	2074*		2190	2225*
Average	1984	2042	2073	2095	2190	2225
Reference 10	1978	2037	2068	2091	2187	2223

② Almost all lines are partially polarized. Only the polarization in which the line is stronger is given in the table.

* Uncertain due to overlaps. Not used for averaging.

Table 4.8

Crystal field splitting of $4_{13/2} (X)$ level of
 $\text{Nd}^{3+}:\text{LaF}_3$ from the fluorescence data at LIT*

Upper level	Lower Levels						
	X_1	X_2	X_3	X_4	X_5	X_6	X_7
E_1	3920 σ	3981 π		4080 σ	4120 σ	4208 σ	4276 $\sigma\pi$
E_2	3921 σ	3980 π	4041 π		4124 σ		
E_3	3921 σ	3978 π	4043 π		4127 σ		4280 π
E_4	3915 σ		4031 π	4076 π	4125 π		
K_1		3982					4284
K_2				4082	4119	4205	4277
K L_2	3921	3982					
L_3	3926	3989		4078	4113		
Average	3921	3982	4038	4079	4121	4207	4279
Reference 10	3919	3979	4039	4078	4120	4213	4278

* Almost all lines are partially polarized. Only the polarization in which the line is stronger is given in the table.

Table 4.9

Crystal field splitting of $^4I_{15/2}$ (W) level of
 $Nd^{3+}:LaF_3$ from the fluorescence data at LNT

Lower levels	Upper levels				Average	Reference 10	Reference 12
	K_1	K_2	L_2	L_3			
W_1	5820		5812		5816	5815	5817
W_2				5879	5879	5877	5876
W_3	5994		5989	5989	5990	5990	5989
W_4			6140*				6142
W_5				6172*	-		6173
W_6	6312		6320		6316		6320
W_7	6445			6450	6448		6448
W_8			6555	6549	6552		6551

* Uncertain due to overlaps. Not used for averaging.

Table 4.10

Crystal field splitting of $4F_{5/2}, 2H_{9/2}$ (S)
 levels of $Nd^{3+}:LaF_3$ from the fluorescence data at LNT*

Upper levels	Lower levels				Average	Reference 10
	K_1	K_2	L_2	L_3		
S_1	12595 $\sigma\pi$	12596 π		12597 σ	12596	12596
S_2	12613 $\sigma\pi$	12609 σ	12613 σ		12615	12613
S_3	12620 π		12620 π		12622	12621
S_4	12673 σ		12676 σ	12680 π	12676	12675
S_5	12693 σ	12698 π	12691 π	12696 $\sigma\pi$	12694	12693
S_6	12755 σ	12751 π	12754 π	12754 $\sigma\pi$	12753	12755
S_7	12844	12842 $\sigma\pi$	12840 π	12843 σ	12842	
S_8	12904		12903 $\sigma\pi$	12906 π	12904	

* Almost all lines are partially polarized. Only the polarization in which the line is stronger is given in the table.

4.4 Two-photon absorption under laser excitation

The intensity (I) of the K and L fluorescence observed with the 5145\AA (Ar^+ laser) excitation is studied as a function of laser power (P) in the range 60 to 700 mw. The laser is used in the 'light control' mode and the power was stable to ± 10 mw throughout. This power range corresponds to a photon flux density⁺ (at the beam waist, see section 2.1) of about 10^{16} - 10^{17} photons $\text{cm}^{-2} \text{sec}^{-1}$. Figure 4.16 is a log-log plot of I vs P for two representative lines, 5973.3\AA (L_3-R_2) and 7270.0\AA (K_2-S_2). The intensity scale is arbitrary and the intensities of the two lines are also not drawn on the same scale. The two straight lines have slopes of 1.72 ± 0.08 and 1.75 ± 0.03 respectively. That is $I \propto P^{1.75}$. The intensities of the other lines also show the same behaviour.

The deviation of this exponent from two is indicative of a more complicated process than a straight forward two photon absorption¹⁶ to be responsible for populating the upper fluorescing levels. This is qualitatively similar to the results obtained in other cases (for example reference 17,18). Reference 17 reports the observation of U.V. and visible fluorescence from $\text{Nd}^{3+}:\text{LaCl}_3$ when excited with the 1.06μ radiation from a Nd:YAG laser. This was explained by them as due to a sequential two step excitation process (inset figure 4.16) involving two photon absorption to the

⁺ An unfocussed laser beam was used while recording the spectrum at Santa Barbara. The much smaller (by a factor of 100) flux densities thus achieved is almost certainly the reason for not observing these lines in those recordings.

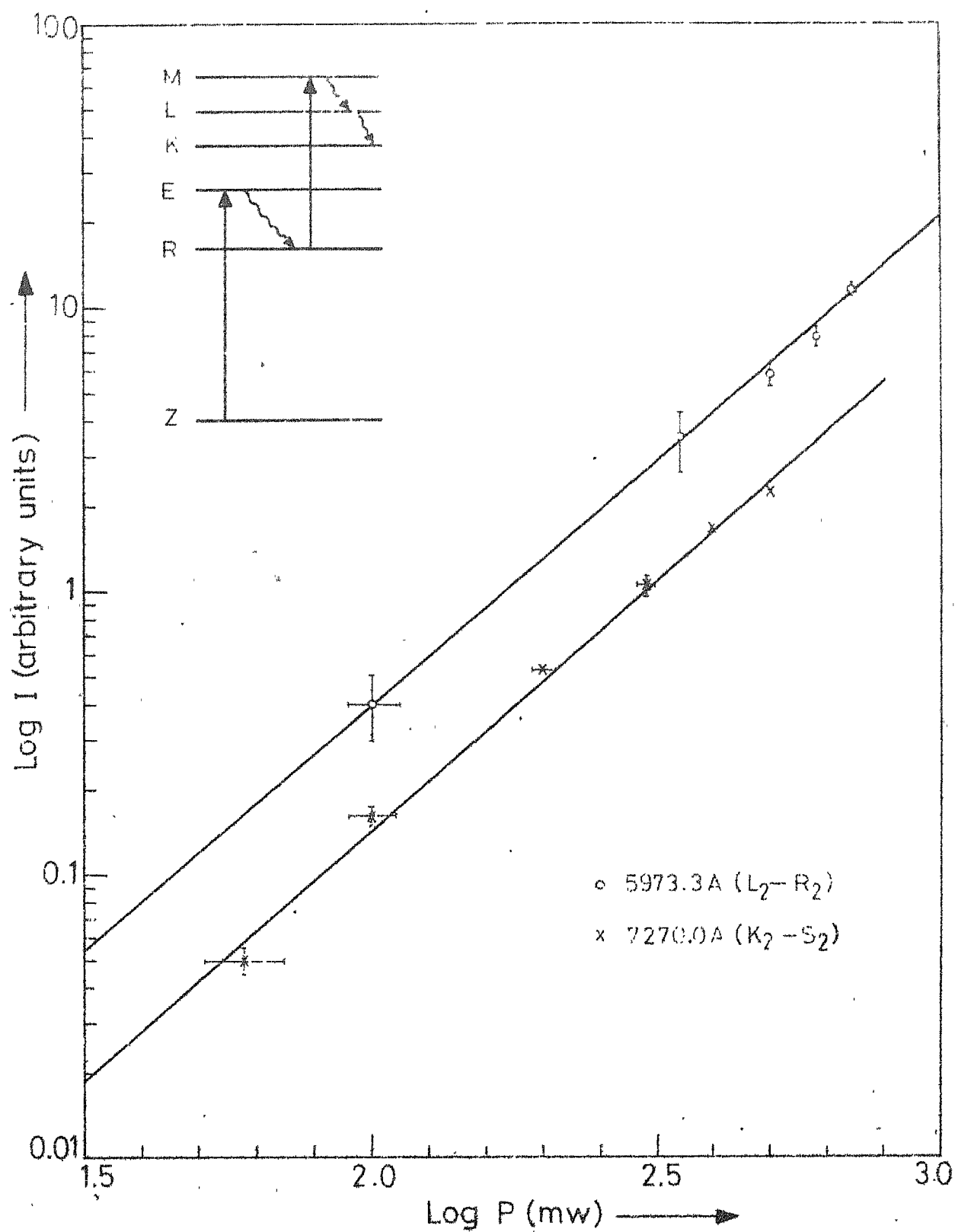


Fig.4.16 The variation of the intensity of K and L fluorescence lines with power.

E level followed by relaxation to the R level and a subsequent two photon absorption to reach the M level. Fluorescence was observed from most of the levels between L and R (figure 4.1) and intensities of all these lines were found to vary as the fourth power of the laser power. This fourth power dependence for the fluorescence from even the levels lower than E is a result of a large efficiency for the four photon process.

Such large efficiencies are however not always encountered. Depopulation from the intermediate states (eg. by $R - Z$, $R - Y$ decay) cause their populations to vary in a sublinear fashion with the laser power and results in a slower rate of increase in the final level population with the laser power, as is being observed in the present case. This was observed in the several multiphoton processes reported in the fluorescence spectra of rare earth ions doped in BaLuF_5 ¹⁸. The intensity varies in general as a polynomial of the n^{th} order (for an n photon process) in the power P . Portions of the plot were seen to be approximatable to a P^m but m rarely being an integer.

In view of this, it can be said that the fluorescence from the K and L levels observed with 5145\AA excitation is not due to a direct two photon absorption but is a result of a more complicated multistep process. One may in general expect energy exchange with the Pr^{3+} (which is present in the crystal) also to be important. Firm conclusions about the detailed

process can be reached only after a study of the time evolution of the fluorescence (after a pulsed excitation) and the various decay rates. It is also necessary to extend the measurements to cover a larger range of incident powers. Such experiments are currently being planned in the laboratory.

4.5 Oscillator strength determination from self absorption

Some of the lines recorded show a double hump nature, characteristic of self absorption (see figure 4.15). The phenomenon can be described briefly as follows. When an active medium of finite physical dimensions is excited (by whatever means), the light emitted in the interior of the medium can get absorbed on its way out. The emission and absorption being due to atoms or ions of the same kind, the absorption co-efficient has substantially the same frequency dependence as the emission line shape. (There can ofcourse be small shifts in the peak position as well as changes in width due to different physical conditions existing in different parts of the medium.) This results in more energy being absorbed at the centre than in the wings. The total intensity and the line shape of the emergent radiation are therefore different from the actual. This is called self absorption.

The observations of this phenomenon are legion in the spectra of gas discharges, the most famous being that of the 2538\AA line of the mercury arc. There are some instances of observation of this effect in the rare earth spectroscopy also (reference 19 for example).

The first complete theoretical treatment of the phenomenon is due to Cowan and Dieke²⁰ who had dealt with the various possible excitation conditions and the line shapes

expected therein. They showed that in the case of a uniformly excited medium, self absorption leads only to a flattening of the peak of the line and in most cases may not be distinguishable from the unabsorbed lines. More pronounced and easily recognizable effects are produced when the absorbing and emitting atoms (or ions) are spatially separated (in general if the degree of excitation is not uniform throughout the medium). In this case the absorption can be so strong that the 'peak' of the line becomes darker than the wings. This is called 'self reversal'. Such conditions obtain in metal arcs and are extensively dealt with by them. A 'hypothetical' idealization of a metal arc, namely one where all the emitters are confined within a narrow cylindrical region around an axis, and all the absorbers are outside, was also considered by them. This ideal condition is achieved in the present experiment, all the emitting ions being within the volume of the narrow laser beam and the rest of the crystal containing the absorbers. The derivation for the line shape under these conditions is outlined here.

In figure 4.15 the laser beam is entering the crystal at a distance ' x ' behind its front face, x being measured along the optic axis of the spectrograph. The symmetry of the excitation around the vertical axis permits a one dimensional treatment and x is the only positional variable needed.

The position of the laser beam can be taken as $x=0$. Then, let

$$I_0(\lambda) = A\phi(\lambda)$$

describe a fluorescence line emitted at $x=0$ with an amplitude A . $\phi(\lambda)$ is a line shape function with the peak at say λ_0 .

After traversing a distance x in a medium containing a uniform density of absorbers, the intensity drops to

$$I_x(\lambda) = A\phi(\lambda) \exp(-\alpha_x x)$$

The absorption co-efficient α_x has the same shape as the emission line shape and thus $\alpha_x = \alpha\phi(\lambda)$. α is called the peak absorptivity and depends on the number of absorbers present per c.c. and the transition probability.

$$\text{Thus} \quad I_x(\lambda) = A\phi(\lambda) \exp[-\alpha\phi(\lambda)x] \quad 1$$

The shape of this function is rather complicated but the positions of its extrema only are of interest for the present. These are at $\frac{d\phi(\lambda)}{d\lambda} = 0$ 2

that is, the centre of the line and at

$$[1 - \alpha x \phi(\lambda)] = 0 \quad 3$$

Since $\phi(\lambda) \leq 1$, equation 3 is satisfied only for $\alpha x > 1$. Also $\phi(\lambda)$ being symmetric around λ_0 , there are two values of λ symmetrically disposed about λ_0 for which this equation is satisfied. A calculation of the second derivative shows that for $\alpha x > 1$, the centre of the line is a minimum, and the two extrema given by equation 3 are maxima.

The line therefore shows a double hump character. The positions and intensities of the humps depend on the exact nature of $\phi(\lambda)$ but the intensity at the line centre is given by

$$I_x(\lambda_0) = \exp(-\alpha x) \quad 4$$

and is valid for any line shape. α is related to the oscillator strength 'f' of the transition by the relation²¹,

$$N_A f = 8.21 \times 10^{16} \frac{n^2}{(n^2+2)^2} \alpha(E) E$$

where n is the refractive index at the wavelength of interest, N_A is the number of absorbing ions per c.c., α is measured in cm^{-1} , and E in electron volts. For a Lorentzian shape function $\phi(\lambda) = 1/[1+a^2(\lambda-\lambda_0)^2]$, the value of the integral is $\alpha\pi/a$. The refractive index of LaF_3 at 8600\AA is earlier reported²² to be 1.58. Using this and converting the energy to cm^{-1} units, one obtains

$$N_A f = 1.249 \times 10^{12} \alpha w \quad 5$$

where w is the full width at half maximum in cm^{-1} (of the unabsorbed line shape) equal to $2/a$. A measurement of the line centre intensity as a function of x (varied by moving the laser beam along the length of the crystal) thus yields the value of α and therefore the oscillator strength. However before using equation 5 the following point has to be considered.

The peak position as well as the width of the transition are functions of temperature and any local heating caused by the laser beam can displace as well as broaden the emission line in relation to the absorption line. The shifts of the R_1-Z_1 and R_2-Z_1 lines are reported²³ as rather small; of the order of 0.1 cm^{-1} per one degree rise in this temperature range. The 'dips' of the recorded self absorbed lines are indeed found to be occurring at the same place as the 'peaks' of the unabsorbed (small x) lines to within 0.5\AA . No measurements are reported on the variation of the width of these lines with temperature. But if the variation found for the R-Y lines²³ is anything to go by, it is a steeply varying function. If the two widths are not same (absorption and emission), it is the width w of the absorption line shape that must be used in equation 5, which is not an observable in the emission experiment.

A simple test is devised to check this. This consists of observing the variation of the hump separation of the self absorbed line shape with αx (or equivalently x) for each line. Substituting the Lorentzian shape function for $\phi(\lambda)$ in equation 3, the humps are seen to be at

$$1 - \frac{\alpha x}{1 + a^2(\lambda - \lambda_0)^2} = 0$$

or at $(\lambda - \lambda_0) = \pm \frac{\sqrt{\alpha x - 1}}{a}$

The hump separation $S = \frac{2\sqrt{ax-1}}{a} = w\sqrt{ax-1}$ 7

This equation is also derived by Cowan and Dieke though the notation used is different. The plot of S^2 vs x for a given line would be a straight line⁺ with an intercept on the yaxis equal to $-w^2$.

These equations are no longer valid if the absorption line has a width $2/b$ different from that of the emission line $2/a$. This situation is not treated in reference 20^φ. Here instead of equation 1 one has,

$$I_x(\lambda) = \frac{A}{1+a^2(\lambda-\lambda_0)^2} \exp\left[\frac{-ax}{1+b^2(\lambda-\lambda_0)^2}\right] \quad 8$$

The humps of this function are located at λ given by

$$(\lambda-\lambda_0)^2 = \frac{-a^2b^2(2-ax) \pm \sqrt{a^4b^4a^2x^2 - 4ax(a^4b^4 - a^2b^6)}}{2a^2b^4} \quad 9$$

A plot of S^2 vs x will be very complicated indeed and will be a straight line only if the term linear in x under the radical is very small compared to the x^2 term which is the same as saying that a is not very much different from b . The test for the equivalence of a and b thus consists in the linearity or otherwise of the S^2 vs x plot.

⁺ For a Gaussian line shape, the relation is $S^2 = \frac{w^2 \ln ax}{\ln 2}$. The plot will not be a straight line.

^φ It may be mentioned here that the entire treatment given in this section has been independantly developed by the author before ~~he~~ came across reference 20.

Experimental details: As is apparent from the preceding discussion, the experiment consists of recording the spectrum with the laser beam entering the crystal at different distances x behind the front face of the crystal (the face towards the monochromator).

The crystal is mounted inside the low temperature dewar in such a way as to have the longest side (4.5 mm) along the optic axis of the spectrometer to have the largest path x possible. It is fortunate that this side is not the c axis, for, in that case only the σ part of transition would be observed. To change x , the dewar, containing the crystal is moved along the optical bench. It is more convenient to do this than to shift the position of the laser beam as the latter involves moving the various components used for steering and focussing the beam. The distance is measured using an OSAW (India) horizontal/vertical cathetometer. Its least count is 0.01 mm, but the inaccuracy in the measured values of x is somewhat larger than this because of the finite width of the luminescence 'streak'.

Three lines identified as the $R_2-Z_1(8593.8\text{\AA})$, $R_1-Z_1(8624.8\text{\AA})$ and $R_1-Z_2(8656.0\text{\AA})$ are seen to be effected, the former two showing self reversal as well. Figure 4.15 shows the lines in the σ polarization. The intensities of these line centres are measured with respect to that of the $R_2-Z_3(8696.0\text{\AA})$ line

recorded in the same run. The line did not show any self absorption and is thus a good 'internal standard' of intensity. This is considered superior to using the values of signal current as such, for the following reason. The bottom window of the dewar (through which the laser beam enters) as well as the bottom face of the crystal can have small dust particles or irregularities on them, and these will lead to a variation in the laser power that actually enters the crystal, as the dewar is moved. This and the other causes like fluctuations in the laser power, line voltage etc. also effect the signal current measured and make it unreliable.

Figures 4.17 and 18 show the $\log I_x(\lambda_0)$ vs x plots for these three lines in the σ and π polarizations respectively. The values of α measured from these plots are given in Table 4.11 alongwith their respective widths. Figure 4.19 is a plot of S^2 vs x for the two lines that show self reversal. The variation is linear and the intercepts 64\AA^2 and 44\AA^2 conform well with the corresponding values of w^2 measured from the unabsorbed emission lines. It can therefore be safely concluded that the emission and absorption line shapes have the same width and the effect of local heating if any is not significant. The lines show significant assymetry, the reason for which is not understood. However, both sides of the lines independantly have Lorentzian shapes and the full widths of the lines are taken 'as measured' without any corrections.

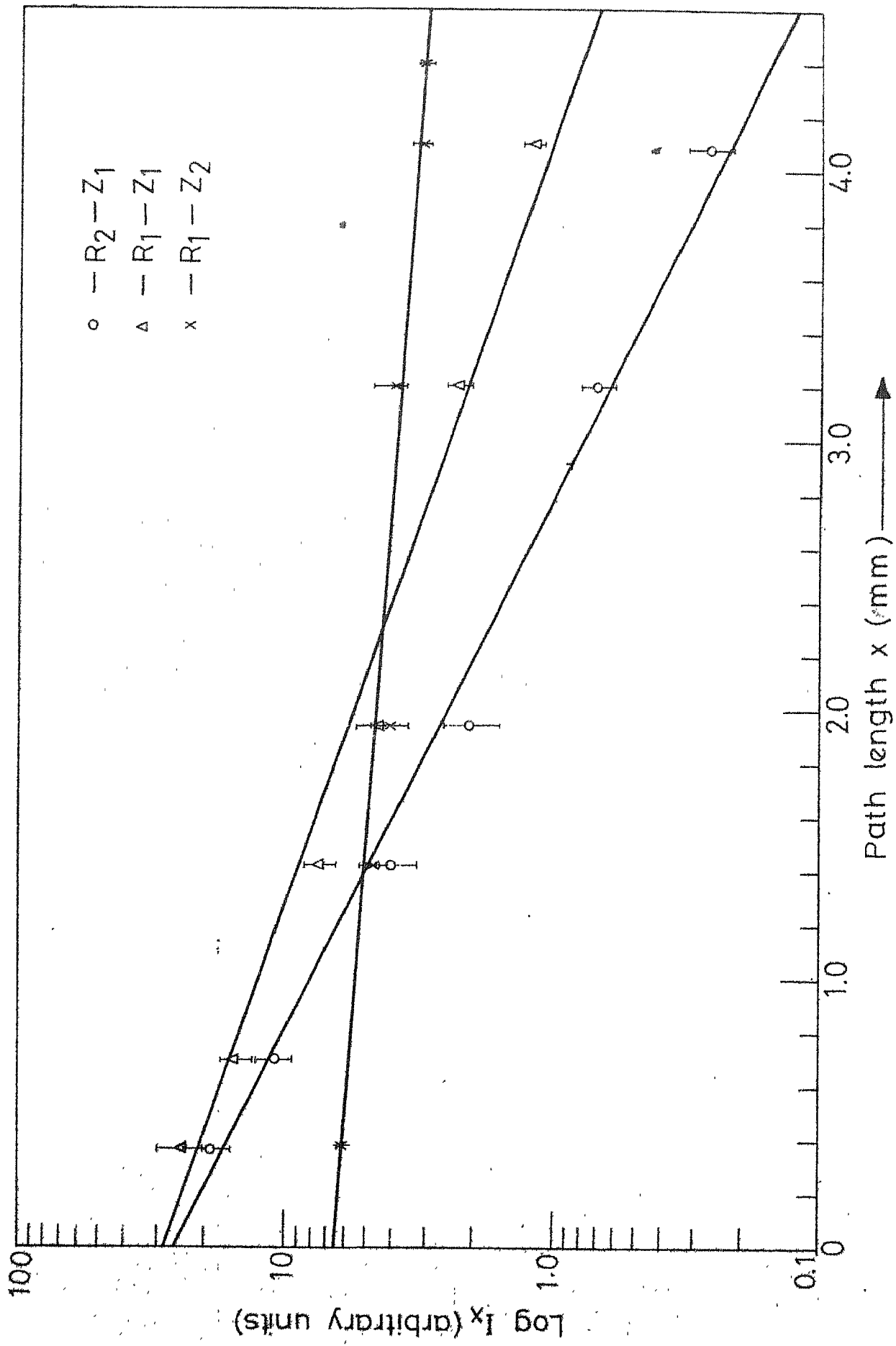


Fig.4.17 Variation of the line centre intensities of the $R \rightarrow Z$ lines with x in σ polarization at 77°K .

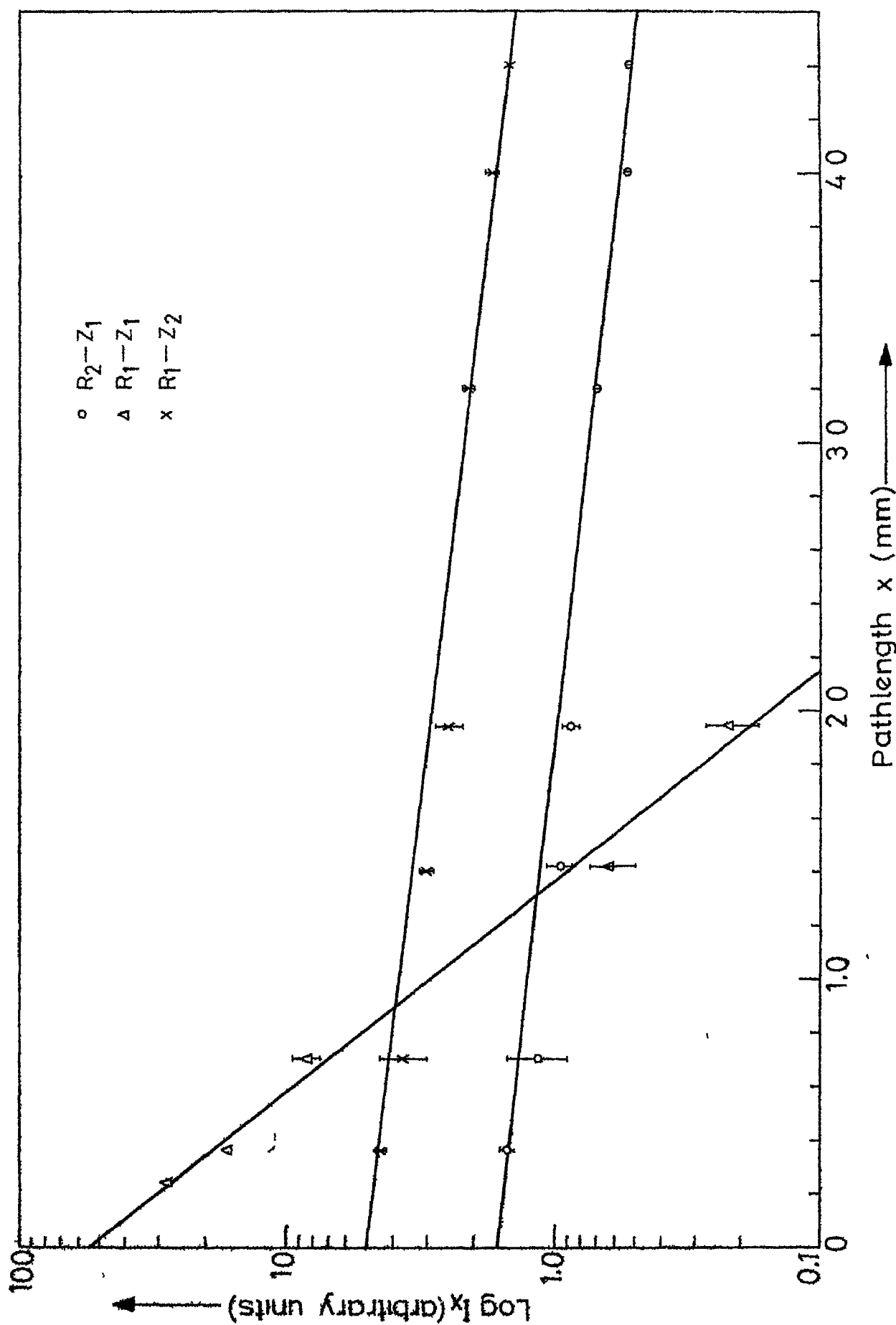


Fig.4.18 Variation of the line centre intensities of the $R \rightarrow Z$ lines with x in π polarization, 77°K.

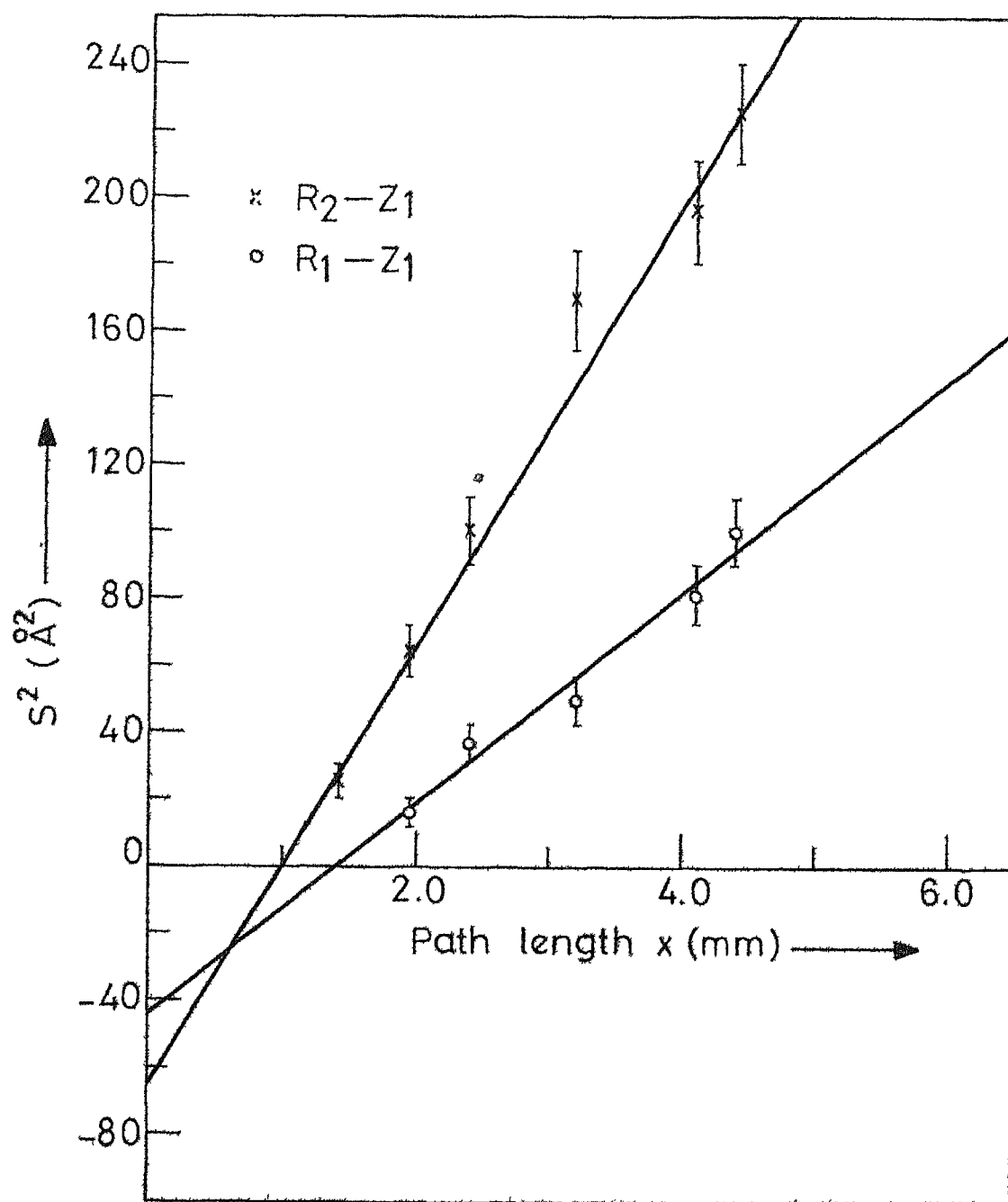


Fig. 4.19. Variation of hump separation (S) of the self reversed lines of the $R \rightarrow Z$ group with x at 77°K .

From the reported²⁴ values of the dimensions of the unit cell; $a = 7.186\text{\AA}$ and $c = 7.352\text{\AA}$, (volume 328.8\AA^3) and the doping percentage (2%, Optovac data), the number density of Neodymium ions N_A is calculated to be equal to 3.65×10^{20} per c.c. Substituting this value of N_A and the values of α from Table 4.11 in equation 5 gives the f number of the transitions.

The 'total' f number of all these (R-Z) transitions is $1.72 \pm 0.08 \times 10^{-6}$. This value is different from the value of 1.09×10^{-6} measured by Krupke²⁵ from optical absorption measurements at room temperature. The reason for the discrepancy is the considerably different population distribution among the Stark components of the $^4I_{9/2}(Z)$ state at the two temperatures. The population in the Z_1 component which accounts for 90% of the absorption at LNT, is only 33% at R.T compared to 61.6% at LNT ($\sim 90^\circ\text{K}$). The population of Z_2 level (45 cm^{-1}) is about 30% in both cases. Using the appropriate weighting factors to reflect these changes, an f number at R.T. of $0.99 \pm 0.05 \times 10^{-6}$ is obtained from the present α values⁺. The current results are therefore in agreement with earlier values.

The (D-Z) group at 5770\AA also is severely self absorbed. Comparison of figures 4.8 and 4.9 shows that these lines are 'almost completely absorbed even for $x = 0.024\text{ cm}$. Varying

⁺ Here it is assumed that the intensity of the 8625\AA line is completely due to the R_1-Z_1 transition. However, part of this (considered to be quite small) is contributed by the R_2-Z_2 transition.

x in steps smaller than this is not possible in the present set up. Also the signal to noise ratio is considerably smaller here than for the (R-Z) group. No measurements are therefore made on these lines. This however demonstrates the nice point that though α (i.e. essentially the radiative transition probability) is larger, the emission intensity could still be smaller evidently due to greater depopulation of D level by phonon processes than the R level.

If the fluorescence were excited by conventional means, that is by using a high pressure mercury lamp or a tungsten lamp, essentially the whole bulk of the crystal is illuminated but the degree of excitation varies from point to point and cannot be calculated. Under this conditions, there is no way to relate the 'dip' height (if at all observed) with absorptivity. This may well be the reason why effects of self absorption were sought to be avoided rather than made use of by earlier workers¹⁹.

This method of measuring 'f' numbers from laser excited fluorescence is probably practicable for α values in the range of 1 to 100 cm⁻¹, the limits being set by normally realizable crystal sizes. In this range, this method offers the advantage of not having to use a calibrated double beam spectrometer that is necessary for absorption measurements.

4.6 The fluorescence spectrum at high temperatures

The relative importance of phonon induced depopulation increases rapidly with temperature (chapter 1) resulting in smaller fluorescence intensities and larger linewidths. The utility of the fluorescence spectrum at R.T or higher temperatures is thus generally limited for the elucidation of energy level structure and related properties. There are however two interesting features observed in the spectrum of $\text{Nd}^{3+}:\text{LaF}_3$ that merit a discussion here.

The first of these is an increase in the total integrated intensity of the fluorescence in going from LNT to RT though the increased phonon rates are amply evident in the much larger linewidths at RT. The broadening is actually so large that all the lines in a single group coalesce together into a broad band. This increase in intensity has probably a simple explanation. At room temperature as many as 32% of the Nd ions are in the Z_3 and Z_4 levels (139 and 291 cm^{-1}) and these ions can resonantly absorb the $19,431\text{ cm}^{-1}$ (5145\AA) photons to reach the F_1 and F_6 levels at 19568 and 19739 cm^{-1} (Table 4.2) respectively. No such resonant absorption is possible from the Z_1 and Z_2 (0 and 45 cm^{-1}) levels which together contain about 90% of the ions at LNT. This would surely lead to greater populations in the fluorescing levels at RT than at LNT and explains the increased fluorescence intensity.

Another prominent feature is the occurrence of S-Z ($7750\text{--}8250\text{\AA}$) and A-Z ($7300\text{--}7600\text{\AA}$) fluorescence at room temperature. These two broad bands completely disappear even a few minutes after pouring liquid nitrogen into the dewar. Heating the crystal to about 85°C increases their intensity by factors of 1.5 and 2.5 respectively while at the same time, the intensity of other fluorescence eg. from E and R levels decreases by a factor of 1.5.

For this experiment, the crystal is held on a copper block (fixed with Quickfix) and heated by a jet of air from a hot air blower. The temperature is measured by a mercury thermometer placed near the crystal. The temperature attained equilibrium in a few minutes and remained constant for the duration of the experiment, of about one hour.

The intensity of fluorescence from a level can increase either due to an increased rate of population of that level or by a decrease in the rate of depopulation by non-radiative processes. In the present case, greater input into the S and A levels by multiphonon decay from higher levels is expected but the energy gap below these levels is about 1000 cm^{-1} and is of the same order as between various other levels. Thus the population of these levels also would be depleted fast by non-radiative decay. A net increase in the population is thus not immediately obvious. This must be brought about by a process which leads to a higher rate of population into

these levels without a corresponding increase in the depletion rate. It must also be more effective at high temperatures. A thermally assisted ion pair relaxation process suggests itself as being most likely. Table 4.12 lists various such transition pairs capable of populating the S level. These involve the decay of a neodymium ion from C to S level by exchanging the difference of energy with another Nd ion in the Z_5 Stark level (500 cm^{-1}) of the ground state, raising it to either X_1 or X_2 . The population of the Z_5 level is negligible at LNT but increases with temperature giving greater efficiency to the process at higher temperatures. That the ion pair processes are more efficient than multiphonon depopulation processes is well known. The variation of the lifetime of the R level with temperature in $\text{Nd}^{3+}:\text{LaF}_3$ is in fact attributed to such a process²⁷. The process responsible for population build up in the A manifold is probably one which involves decay of Nd^{3+} from D to A, and simultaneous excitation of Pr^{3+} (which is present in the crystal) from the upper Stark components ($136\text{--}500\text{ cm}^{-1}$) of the $^3\text{H}_4$ ground state into the $^3\text{H}_6$ level. Several such transition pairs could be located from the energy level structures of the two ions. These are indicated in Table 4.13. Extensive ion pair energy exchange between Nd^{3+} and Pr^{3+} was in fact observed earlier²⁶.

Table 4.12

Possible ion pair transitions to populate
the S level of Nd^{3+} at high temperatures

Transition (Downward) Nd^{3+}	Energy cm^{-1}	Transition (Upward) Nd^{3-}	Energy cm^{-1}
$G_2 - S_2$	3420	$Z_5 - X_1$	3419
$G_3 - S_3$	3424		
$G_5 - S_4$	3428		
$G_5 - S_5$	3410		
$G_5 - S_2$	3490	$Z_5 - X_2$	3479
$G_5 - S_3$	3482		

Differences in energy of the order of 10 cm^{-1} are not
important because of the large widths of the transitions
at high temperatures.

Table 4.13

Possible ion pair transitions to populate the
the A level of Nd^{3+} at high temperatures

Downward transition Nd^{3+}	Energy cm^{-1}	Upward transition* Pr^{3+}		Energy cm^{-1}
		$^3\text{H}_4$	\longrightarrow	$^3\text{H}_6$
$\text{D}_7 - \text{A}_1$	4086	137		4219
		137		4223
		207		4300
		296		4385
		508		4591
$\text{D}_6 - \text{A}_1$	4055	203		4266
		330		4385
$\text{D}_5 - \text{A}_1$	4005	296		4300
$\text{D}_4 - \text{A}_1$	3997	508		4508
$\text{D}_1 - \text{A}_1$	3789	508		4300
$\text{D}_7 - \text{A}_2$	4010	203		4219
		508		4527
$\text{D}_1 - \text{A}_2$	3713	508		4219
		508		4223
$\text{D}_7 - \text{A}_3$	3930	296		4219
		296		4223
		508		4440
$\text{D}_6 - \text{A}_3$	3899	330		4223
$\text{D}_6 - \text{A}_4$	3893			

Energy differences of the order of 10 cm^{-1} are not of importance
because of the large widths of the transitions at high temperatures.

* Pr^{3+} energy levels are from reference 16.

This explanation has the status of being only plausible at this stage. Looking simply for changes in the intensity of the X-Z fluorescence of Nd^{3+} as the temperature is varied may not lead to conclusive results since there can be various factors effecting this quantity. (An earlier attempt by Asawa and Robinson²⁷ to observe the X-Z and X-Y fluorescence was not successful). Looking for the ${}^3\text{H}_6\text{-}{}^3\text{H}_4$ fluorescence from Pr^{3+} also may not be fruitful since transitions between several other levels of Nd^{3+} (X-Z, W-Y, C-R) are also capable of populating the $\text{Pr}^{3+}\text{-}{}^3\text{H}_4$ level by energy exchange. Confirmatory evidence can only be obtained by a detailed investigation of the build up and decay times of the various fluorescence transitions in the temperature range of interest.

4.7 Polarization of the observed lines

In view of what is said in section 3.2 and reference 9 there is no simple explanation for this feature of the spectrum. Such polarization has been also observed²⁸ in the spectrum of Neodymium in Lanthanum penta phosphate recently. In this crystal, the site symmetry of Nd^{3+} is C_1 .

One possible explanation is that the lines, at least some of them, are vibronic in nature. The symmetry does not actually predict polarization in that case also, but it is not unreasonable to expect that the vibronic line would be

stronger in the polarization in which the electric vector is parallel to the direction of oscillation of say the R.E. ion. The two Stark components Z_2 and Z_3 actually occur at almost the same positions as two of the observed phonon frequencies. And it is likely that all transitions identified as involving Z_2 and Z_3 actually involve phonons of those energies. If the above hypothesis were true, then all lines involving say 45 cm^{-1} as lower level must be similarly polarized. Data presented in Tables 4.6 through 4.10 does not support this. No such uniform polarization is observed in transitions involving either a particular lower level or even a particular upper level. Also, the Zeman⁷ study¹³ on NdF_3 makes ~~one~~ inclined to believe that the observed levels are in fact electronic levels only.

In the end, it may be just that, while the symmetry allows a transition in both the polarizations, the relative intensities depend on the detailed nature of the wavefunctions and the line can still be partially polarized or even be completely polarized.

REFERENCES

1. Robert A. Satten, J. Chem. Phys. 21, 637 (1953).
2. G.H. Dicke, Spectra and Energy Levels of Rare Earth Ions in Crystals (Interscience 1968),
E. Carlson and G.H. Dieke, J. Chem. Phys. 29, 229 (1958); 34, 1602 (1961),
E.H. Carlson, Johns Hopkins Spectroscopic Report No. 18 (1960).
3. J.C. Eisenstein, J. Chem. Phys. 39, 2134 (1963),
L.F. Johnson, J. Appl. Phys. 34, 897 (1963),
J.A. Konningstein and J.E. Geusic, 136, A711 (1964),
N.C. Chang, J. Chem. Phys. 44, 4044 (1966),
P.A. Narayana, Can. J. Phys. 47, 2753 (1969),
M.J. Weber and T.E. Vartans, J. Appl. Phys. 42, 4996 (1971),
Stanely M. Kulpa, J. Chem. Phys. 56, 1198 (1972),
A.J. Lindop and D.W. Goodwin, J. Phys. C. Solid State Phys. 6, 1818 (1973).
4. R.M. Aggarwal et.al., Proc. Ind. Acad. Sci. LV, 325 (1962).
5. B.G. Wybourne, J. Chem. Phys. 32, 639 (1960);
34, 279 (1961).
6. E.H. Carlson, Johns Hopkins Spectroscopic Report No. 19 (1960).
7. K. Rajnak, J. Chem. Phys. 43, 847 (1965).
8. H. Crosswhite, H.M. Crosswhite and B.R. Judd, Phys. Rev. 174, 89 (1968).
9. E.Y. Wong, O.M. Stafsudd, D.R. Johnston, Phys. Rev. 131, 990 (1963).

10. H.H. Caspers, H.E. Rast, R.A. Buchanan, J. Chem. Phys. 42, 3214 (1965).
11. E.Y. Wong, J. Chem. Phys. 35, 544 (1961).
12. Yu.K. Voron'ko, V.V. Osiko, N.V. Sarostyanova, V.S. Fedorov and I.A. Scherbakov, Soviet Phys. Solid State 14, 2294 (1973).
13. Y.K. Chow, Zs. f. Physik 124, 52 (1948).
14. W.M. Yen, W.C. Scott and A.L. Schawlow, Phys. Rev. 136, A271 (1964).
15. H.H. Caspers, H.E. Rast and R.A. Buchanan, J. Chem. Phys. 43, 2124 (1965).
16. W. Kaiser and C.G.B. Garrett, Phys. Rev. Letters 7, 229 (1961),
John F. Porter Jr., Phys. Rev. Letters 7, 414 (1961),
Warner L. Petticolas, John. P. Goldsborough and
K.E. Reickhoff, Phys. Rev. Letters 10, 43 (1963),
M. Ianuzzi and E. Polacco, Phys. Rev. Letters 13,
371 (1964).
17. S. Singh and J.E. Geusic, in Optical Properties of Ions in Crystals ed. H.M. Crosswhite and H.W. Moos (Interscience 1967), page 493.
18. L.F. Johnson, H.J. Guggenheim, T.C. Rich and F.W. Ostermayer, J. Appl. Phys. 43, 1125 (1972).
19. G.K. Asawa, Phys. Rev. 155, 188 (1967).
20. R.D. Cowan and G.H. Dieke, Rev. Mod. Phys. 20, 418 (1948).
21. Y.B. Fowler, Physics of Colour Centres (Academic Press 1968) page 72.

22. G. Hass, J.B. Ramsey and R. Thun, J. Opt. Soc. Am. 49, 116 (1959).
23. S.A. Johnson, H.G. Freie, A.L. Schawlow and W.M. Yen, J. Opt. Soc. Am. 57, 734 (1967).
24. J.D.H. Donnay and D. Donnay, Crystal data (American Crystallographic Association, 1963)2nd ed.
25. William F. Krupke, Phys. Rev. 145, 325 (1966).
26. D.J. Zalucha, J.A. Sell and F.K. Fong, J Chem. Phys. 60, 1660 (1974).
27. C.K. Asawa and M. Robinson, Phys. Rev. 141, 251 (1966).
28. S. Singh, D.C. Miller, J.R. Protopowicz and L.K. Shick, J. Appl. Phys. 46, 1191 (1975).

CHAPTER 5

THE EPR SPECTRA OF Nd^{3+} IN LaF_3 AND
 PbMoO_4 AT LIQUID HELIUM TEMPERATUREABSTRACT

The EPR spectra at liquid helium temperatures of Nd^{3+} : LaF_3 and Nd^{3+} : PbMoO_4 are reinvestigated to check whether extra lines found in the respective absorption spectra could be due to the existence of different kinds of Nd centres. No evidence for this was found in LaF_3 . In PbMoO_4 however the EPR spectrum contained a set of lines attributable to Nd^{3+} possibly associated with a next neighbour defect in the [110] plane. The intensity of these lines is less than 1% of the main lines which are due to Nd^{3+} experiencing a crystal field of S_4 symmetry oriented along the c axis of the crystal.

5.1 Introduction

Electron paramagnetic resonance is a very powerful tool for studying the local symmetries of paramagnetic ions either in solutions or solid lattices. The specific feature of relevance to the present study is its ability to detect small changes in site symmetry. If a small fraction of the paramagnetic ions present in a crystal experience a slightly different crystal field than the rest of the ions, they would give rise only to weak satellite lines in the optical spectrum. The information obtainable from these satellites is usually very small. The EPR spectrum of these ions could on the other hand differ significantly from the main spectrum and a proper investigation of the anagular variation of the spectrum would yield reliable information about the difference in the site symmetry.

The optical spectra of $\text{Nd}^{3+}:\text{LaF}_3$ ¹ and the $\text{Nd}^{3+}:\text{PbMoO}_4$ ² contain some weak extra lines which might conceivably belong to Neodymium ions situated at sites that are different from the rest. This chapter describes the work done on the EPR spectra of these crystals to locate any such centres.

5.2 The spin Hamiltonian

The ground state¹ of Nd^{3+} is $^4\text{I}_{9/2}$. Because of the large orbital angular momentum (unquenched) of this state, the EPR spectrum is observable only at liquid helium temperatures. At higher temperatures, the spin-lattice relaxation times are very short and the lines become unobservably weak and broad³.

In any crystal field of less than cubic symmetry, (which is unlikely to be encountered in the present case), the $^4\text{I}_{9/2}$ state splits into five Kramers' doublets and for Nd^{3+} in these two crystals, the splitting is of the order of 50 to 100 cm^{-1} . Thus at LHeT ⁺, only the ground state Kramers' doublet is populated. The first excited state is also too far off to be effected by the microwave frequency (less than 1 cm^{-1}) of the EPR experiment. An 'effective spin half' Hamiltonian³ would therefore be appropriate for this two level (Kramers' doublet) system

$$\mathcal{H} = \beta \underline{H} \cdot \underline{g} \cdot \underline{S} + \underline{I} \cdot \underline{A} \cdot \underline{S}$$

⁺ Liquid helium temperature.

where the symbols have their usual meaning. In case of axial symmetry the Hamiltonian would be

$$\mathcal{H} = g_{\parallel} \beta H_z S_z + g_{\perp} \beta (H_x S_x + H_y S_y) + A I_z S_z + \frac{B}{2} (S_+ I_- + S_- I_+)$$

Natural Neodymium has several even isotopes (zero nuclear spin) making upto 80% of the total and two odd mass isotopes with mass numbers 143 and 145. The odd mass isotopes have 12.2% and 8.3% natural abundances and both have nuclear spins of 7/2. In cases where the hyperfine structure is large enough to be resolvable, the spectrum would consist of a strong central line due to the even mass isotopes and two sets of eight hyperfine lines each, due to the odd isotopes. The magnetic moment of the lighter isotope (143) being about 1.5 times larger than that of the heavier isotope (145), the hyperfine groups are usually well separated.

5.3 Experimental details

The experiments are done⁺ on a Varian No. V4502-12, X-band EPR spectrometer equipped with a V-K3525, superheterodyne adapter and a V4545A, liquid helium accessory. The D.C. field (H_0) is provided by a Varian No. V3400, 9" rotatable magnet.

⁺ The author is thankful to Dr. T.M. Srinivasan for his co-operation and help in these experiments.

The following minor modifications are made to the liquid helium accessory to suit the current requirements. For large crystals the fixed (iris) cavity coupler supplied by Varian is found inadequate and a variable coupler similar to the one described by Ramon and Stamires⁴ is incorporated. In this the coupling is varied by moving a 12BA screw across the coupling hole with a worm and gear combination. It is possible to achieve critical coupling with this arrangement even with a crystal as large as $10 \times 7 \times 4 \text{ mm}^3$ of LaF_3 . Another modification is with regard to the field modulation coils. These are mounted on the outside of liquid helium dewar itself (figure 5.1) and are found to be the source of excessive baseline drift⁺ with field (H_0), when it is directed at angles ϕ larger than about 20° from the axis (xx in figure 5.1) of the coils. Also, at large angles the component of the modulation field parallel to the static field (H_0) is greatly reduced and signal intensity is lost. Both these problems are solved by removing these coils and fixing another pair of circular (Helmholtz) coils mounted directly on the magnetic pole pieces. The coils are made of 150 turns (each) of 38SWG enamelled copper wire wound on $1/8"$ thick perspex discs of 5.5 cm radius (equal to the pole gap).

⁺ The mechanical vibration of the modulation coils induced by H_0 is responsible for this.

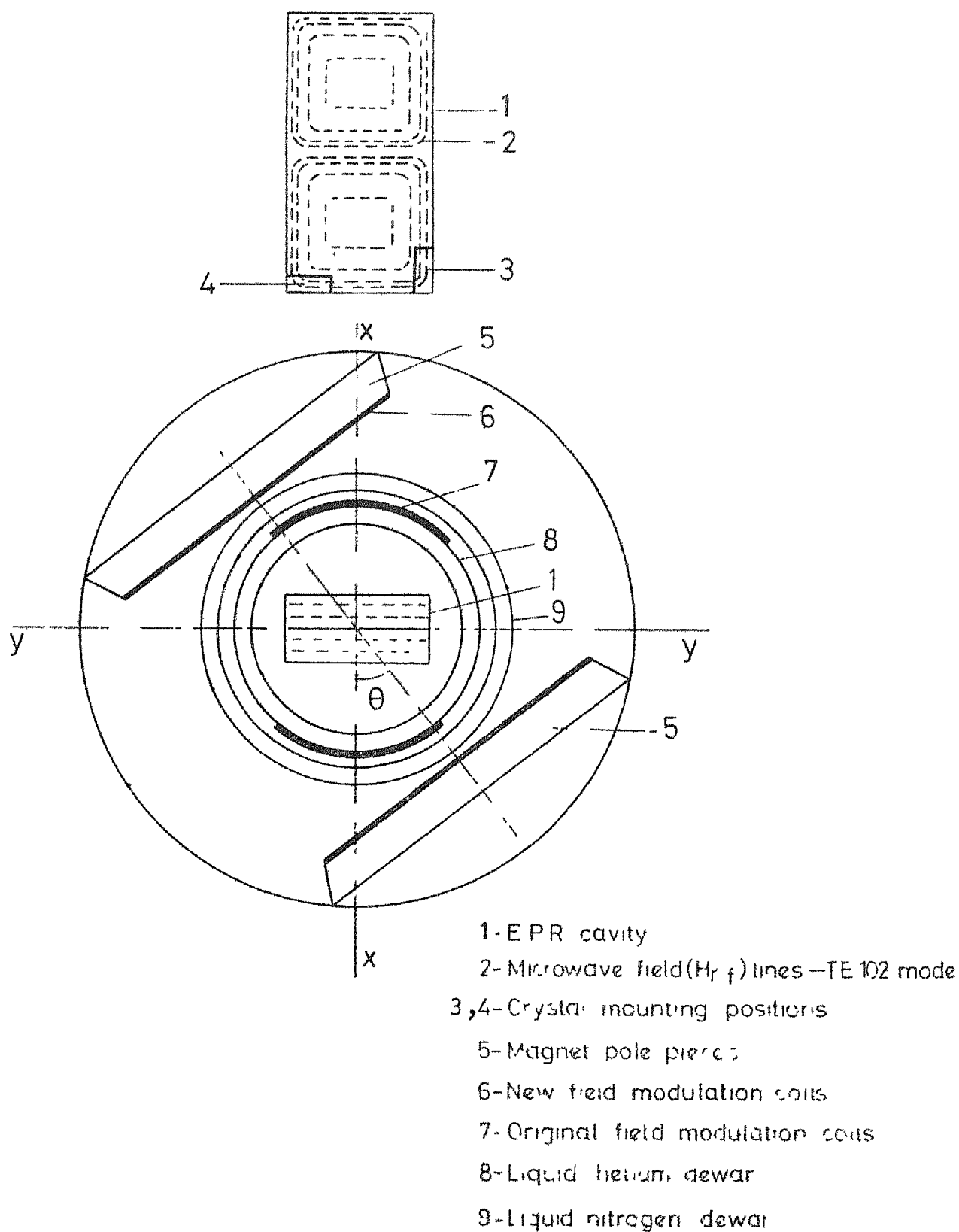


Fig.5.1 Configuration of magnetic fields in the EPR set-up at 4.2°K.

The microwave cavity operates in the TE_{102} mode with the microwave field in the form of flat loops in vertical planes as shown in figure 5.1. Both the crystals studied (LaF_3 and $PbMoO_4$) have their principal axes parallel to their external sides and thus the problems of orientation are minimized by cementing the crystals with quickfix in a corner of the cavity flush to the walls. Due to this, the crystals experience a horizontal as well as a vertical component of the microwave field as can be seen from figure 5.1. When H_0 is oriented along the narrow side of the cavity (xx in the figure), both these components are perpendicular to it. But at other angles the horizontal arm gives rise to a component parallel to H_0 . This situation leads to the observation of some interesting forbidden transitions described in section 5.7.

5.4 The EPR spectrum of $Nd^{3+}:LaF_3$

Previous publications⁵ on this spectrum reported the observation of a six line spectrum attributed to Neodymium ions substituting Lanthanum ions at sites of C_s symmetry. No hyperfine structure was reported.

A re-investigation made here, of the spectrum and its angular variation in a plane containing the c axis as well as in a plane perpendicular to it, has only reproduced the results of the earlier observations. Figure 5.2 shows the spectrum

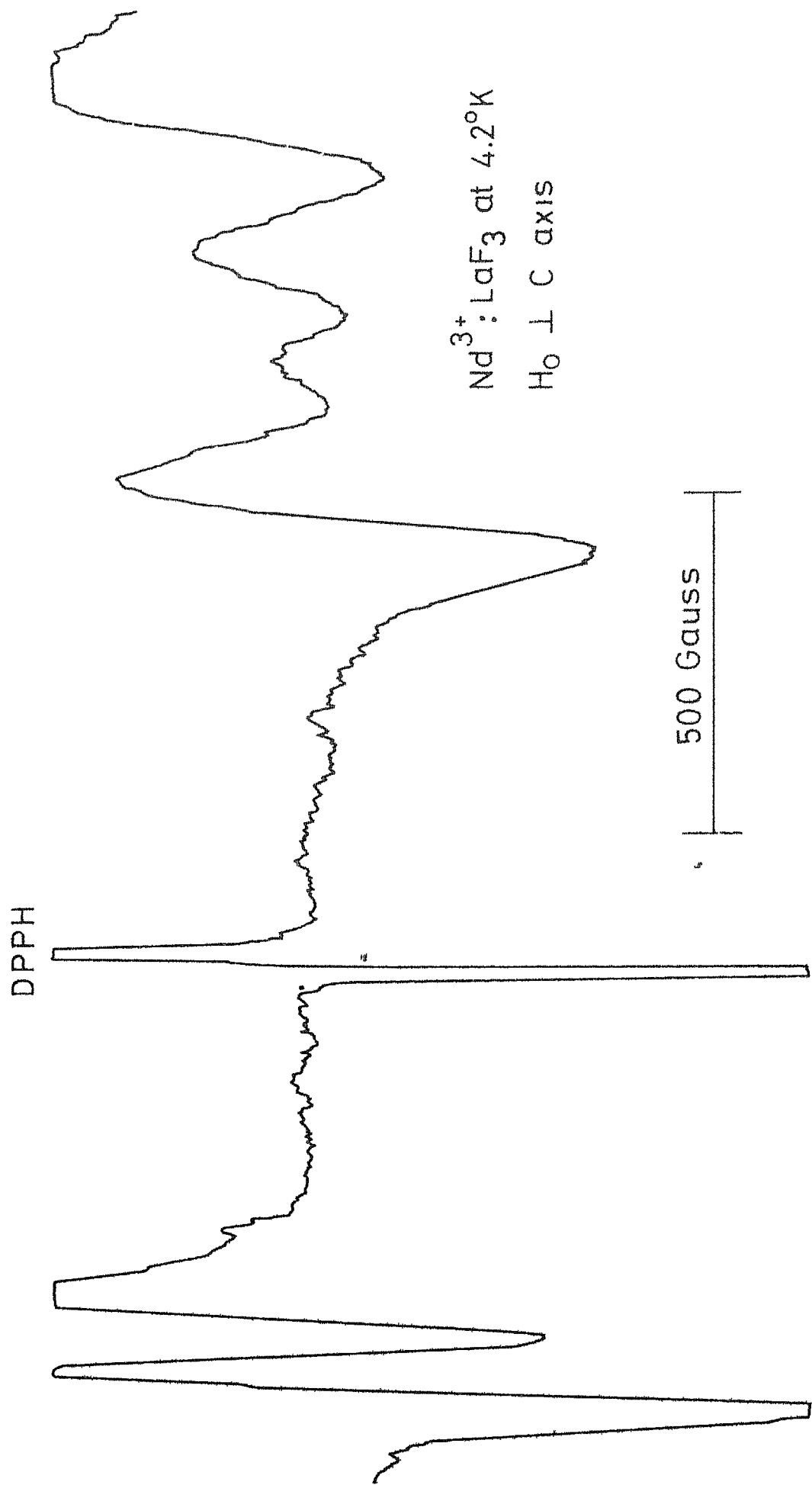


Fig.5.2 $\text{Nd}^{3+}:\text{LaF}_3$ EPR spectrum at 4.2°K , H_0 in a direction perpendicular to c axis

obtained with H_0 oriented in a direction perpendicular to the c axis. No extra lines that can be attributed to a different kind of Neodymium centre are found.

The lines observed have widths varying between 50 and 100 gauss with angle. These large widths may be due to unresolved hyperfine structure (no HF lines are observed). Considering the width of the lines to be representing the total spread of a hyperfine spectrum, the hyperfine coupling constant is estimated to be about 10 gauss which is rather low.

5.5 EPR spectrum of $PbMoO_4$

Lead Molybdate is a member of the Scheelite ($CaWO_4$) homolog series. The crystal structure⁶ is tetragonal and the space group is C_{6h}^4 . The unit cell is illustrated in figure 5.3. The oxygen ions (not shown in the figure) surrounding the lead ions (larger circles) give them S_4 symmetry. Numerous earlier EPR investigations on Nd^{3+} doped in lead molybdate⁷ and other Scheelites⁸ demonstrated that the Nd^{3+} replaces Pb^{2+} substitutionally and the charge compensation is usually far away and does not change the site symmetry. There have been however one or two cases⁹ where effects of nearby defects were observed. The optical absorption study of Minhas et al.² on Nd^{3+} $PbMoO_4$ showed that the spectrum is essentially due to

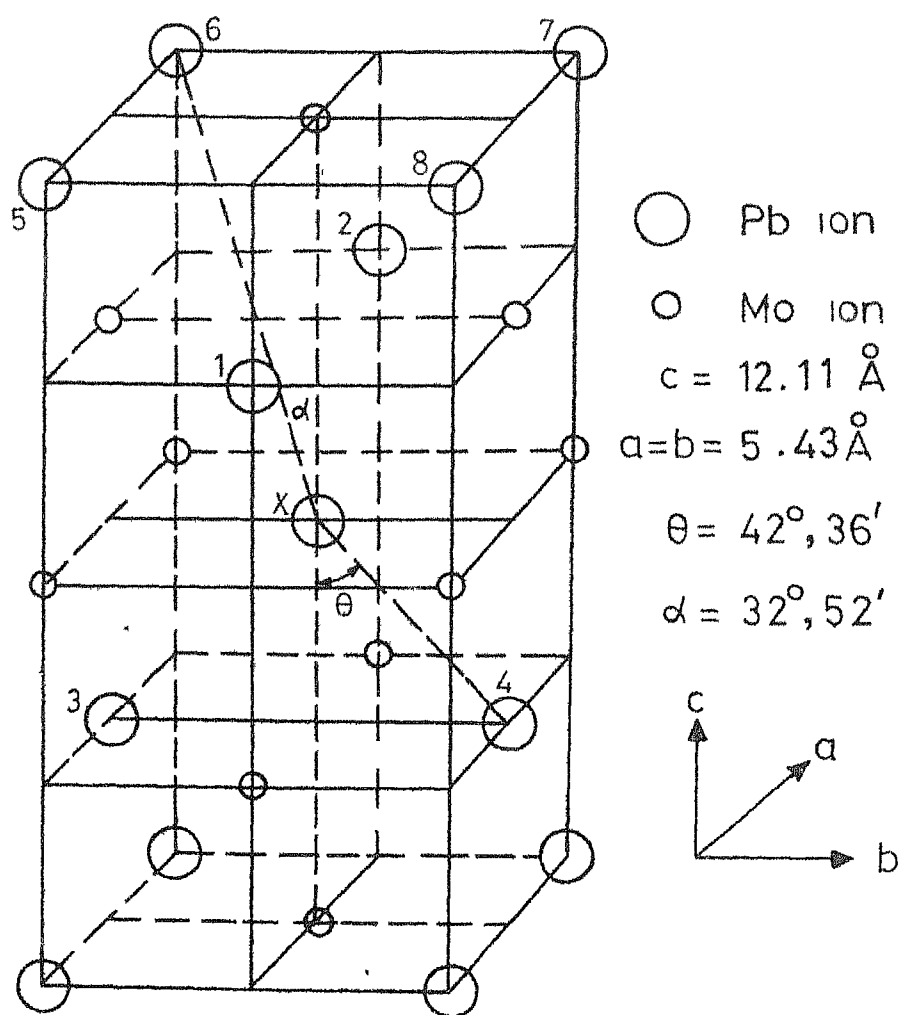


Fig.5.3 Unit cell of PbMoO_4 .

Neodymium ions at undistorted S_4 sites but there exist a few weak lines close to the main lines which do not belong to those ions. They felt that these may be due to a different kind of Nd centres.

Single crystals of $\text{Nd}^{3+}:\text{PbMoO}_4$ were grown by Minhas and Sarma using the Czochralski technique. A spectroscopic analysis (carried out at the Spectroscopy division, BARC, Bombay) showed that the crystals contain 180 ppm of Neodymium and a comparable amount of sodium which is added for charge compensation. A thin rectangular plate $1 \times 3 \times 6 \text{ mm}^3$ was cut from one of these crystals for this EPR study. The plane of the plate is parallel to the crystalline ac plane (found by Laue photograph) with the c axis parallel to the 3 mm side. The crystal is mounted in the EPR cavity in either position 3 or 4 (figure 5.1) depending on the plane (aa or ac) in which the spectrum is to be studied.

Figure 5.4 shows the spectrum obtained with H_0 oriented 25° away from the c axis, in the ac plane. The spectrum is dominated by the seventeen line structure of Nd^{3+} at the undistorted sites. In the figure, the spin-less transition is designated as 0, the hyperfine lines of the lighter isotope as a_1 - a_8 and those of the heavier isotope as b_1 - b_8 . Figure 5.5 shows the angular variation of the positions of lines 0 and a_1 - a_8 . The set 'b' vary in a similar fashion.

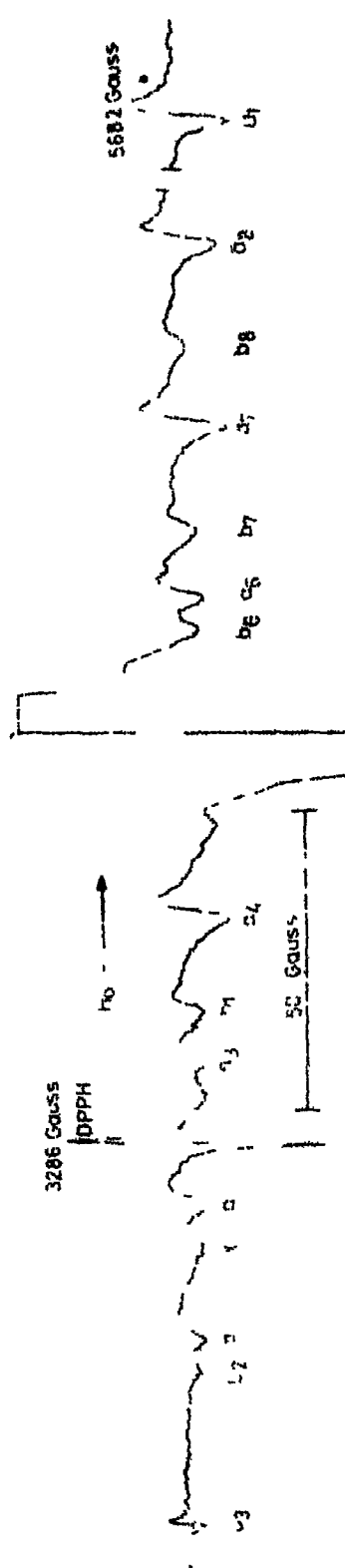


Fig 5.4 The EPR spectrum of Nd^{3+} in LaCl_3 at 4.2°K with H_0 at 25° to the c axis in an ac plane (a) — (g) — HLF lines of Nd^{3+} (h) — (l) — HLF lines of Nd^{3+} spinless transition

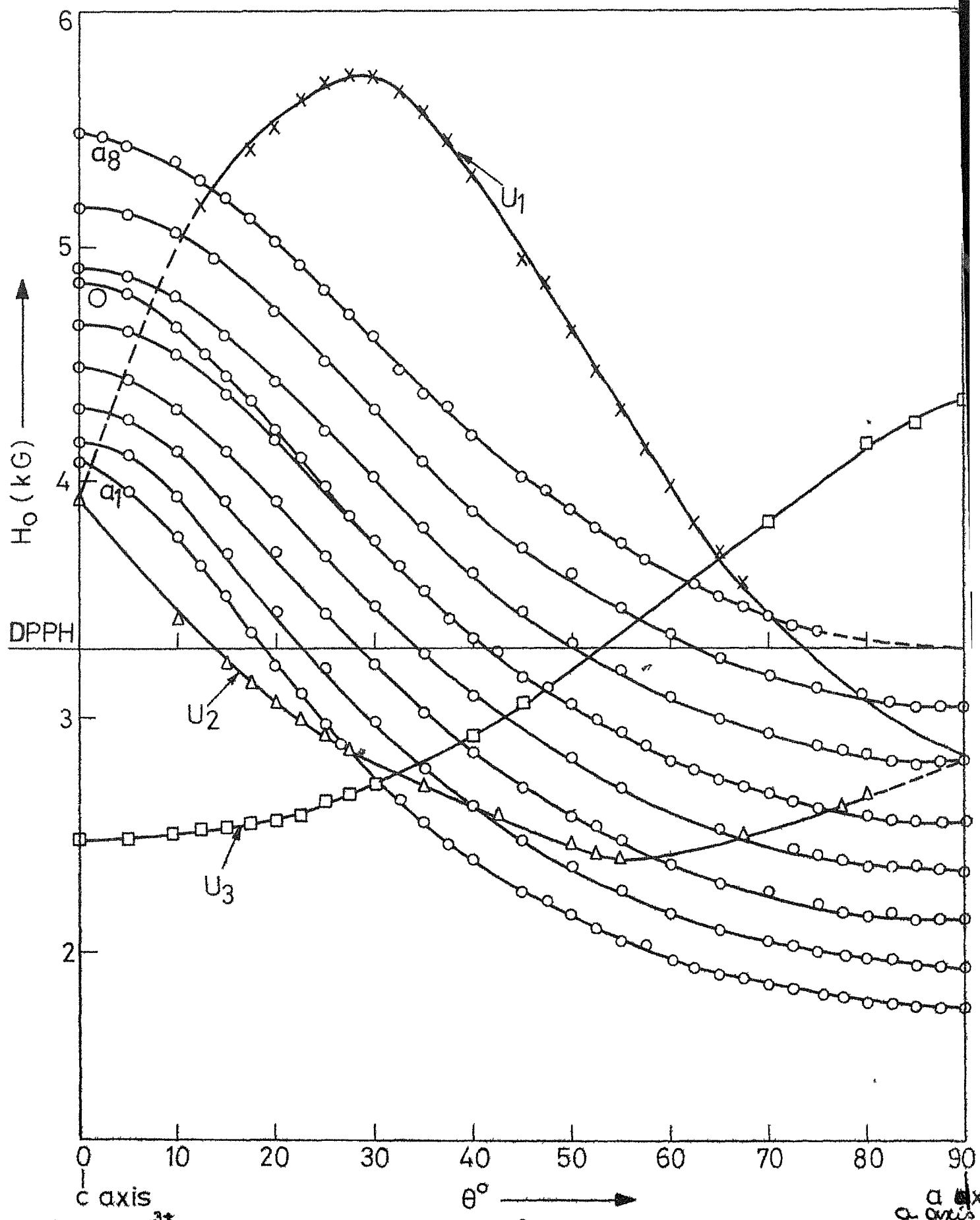


Fig.5.5. $\text{Nd}^{3+}:\text{PbMoO}_4$ EPR spectrum at 4.2°K, angular variation in the ac plane.

but are not shown in the figure. The constants of the spectrum are

$$g_{||} = 2.595 \pm 0.02 (2.592 \pm 0.005), \quad g_{\perp} = 1.348 \pm 0.006 (1.351 \pm 0.002)$$

$$A^{143} = 24 \pm 2 \times 10^{-4} \text{ cm}^{-1} (128 \pm 1), \quad B^{143} = 267 \pm 4 \times 10^{-4} \text{ cm}^{-1} (269 \pm 1)$$

$$A^{145} = 79 \pm 1 \times 10^{-4} \text{ cm}^{-1} (80 \pm 1), \quad B^{145} = 167 \pm 2 \times 10^{-4} \text{ cm}^{-1} (167 \pm 1)$$

The values in paranthesis are the results of earlier^{8,9} determinations.

The spectrum also shows three more lines (marked U_1, U_2 and U_3 in figure 5.4) which do not belong to this set. The angular variation in the ac plane of these lines also is shown in figure 5.5. The lines U_1 and U_2 appear to be coalescing into a single line when H_0 is parallel either to the c axis or the a axis. However, there is considerable overlap in these directions with the strong lines of the main spectrum and it is not possible to be sure about this point. The extrema of these lines occur 30° and 60° away from the c axis. This feature sets them apart from the U_3 line which has its extrema on the c and a axes. The g values (in the ac plane) are

$$g_{\min}(U_1) = 1.15 \pm 0.005, \quad g_{\max}(U_2) = 2.76 \pm 0.02$$

$$g_c(U_3) = 2.662 \pm 0.02, \quad g_a(U_3) = 1.522 \pm 0.005$$

When the magnetic field is varied in the aa plane, the main spectrum remains invariant. The U_3 line which does not split in the ac plane and has extrema along the a and c axes must also be angular independent in this plane. Unfortunately in this particular experiment, only in one case namely, H_0 oriented 15° away from an a axis, is the spectrum scanned upto the high field (about 4.5 kG) necessary to record this line⁺. And in this, the line is in fact found at the same field value, as on the a axis and so it can be concluded that it is invariant in the plane. The two lines U_1 and U_2 should show angular variation in this plane also but it is not found possible to locate them among the strong lines of the main spectrum.

There are several possible locations, a compensating charge (Na^+ for example) or any other defect can occupy and alter the environment of the paramagnetic ion. The first possibility to be considered is that the U_3 line is due to Nd ions associated with a defect along the c axis at a distance of one lattice unit (12.4\AA), the hyperfine lines which would be two orders of magnitude weaker, being lost in noise. The distance of the defect being rather large, its effect will probably be small. Reference 9 gives the data on the EPR spectra of Nd^{3+} in nine Scheelites with varying c/a ratios. Here it was seen that the value of g_{11} ,

⁺ The experiment could not be repeated due to the non-availability of liquid helium later on.

varies rather widely between 0.7 and 2.17 but g_{\perp} varies only between 2.535 and 2.58 along the whole series. Thus, varying axial perturbations have little effect on g_{\perp} . Thus U_3 line for which g_{\perp} is 1.522 does not belong to Nd^{3+} . The g values however are close to the values $g_{\parallel} = 2.92$, $g_{\perp} = 1.43$ found¹⁰ for Ce^{3+} substituting Calcium in CaWO_4 at S_4 sites. It is therefore likely that this line belongs to Ce^{3+} substituting Pb^{2+} at undistorted S_4 sites.

U_1 and U_2 as a pair should be due to centres associated with off axis defects. The Pb site along $[111]$ direction (positions 5,6,7,8 in the figure 5.3) is a likely choice. There are four such centres oriented along the four $[111]$ axes. All of these would give rise to a single line along the c axis which splits into two in the ac plane. These two again coalesce into one along the a axis, if one of the g principal axes lies along the $[111]$. In that case the angular variation can probably show extrema at about 30 and 60 to the c axis, the angle the $[111]$ makes with the c axis being about 33° . The maximum and minimum g values of these lines are in the same range as for Nd^{3+} in Scheelites and so U_1 and U_2 may be assigned to Nd^{3+} associated with a defect along $[111]$ axis.

Centres associated with defects in the 1,2,3 or 4 kind of (figure 5.3) sites should give three lines in the ac plane.

Centres associated with defects along the a axis would give rise to two lines in the ac plane but, must have one of their g principal axes parallel to the a , the ac plane being a symmetry plane. Ions substituting for M_0 in the molybdate group will have more or less isotropic g tensors because of their near tetrahedral oxygen co-ordination. None of these three models can thus explain the observed angular variation and are discarded.

In conclusion, it is likely that the U_3 line is due to a Ce^{3+} at undistorted lead sites^{and} the two lines U_1 and U_2 are due to Nd^{3+} associated with a defect along the $[111]$ direction. Thus the conjecture that the extra lines in the optical spectrum are due to a different kind of Nd centre is probably true.

5.6 Forbidden transitions in the EPR spectrum of $Nd^{3+} : PbMoO_4$

The spin Hamiltonian contains terms which are not diagonal in I_z and S_z and which mix together the various electron nuclear product wavefunctions. For the simple case of a spin half Hamiltonian with H_0 parallel to the Z axis,

$$\mathcal{H} = g\beta H_0 S_z + A I_z S_z + \frac{B}{2} (S_+ I_- + S_- I_+)$$

the second order energies are given by

$$E_{Mm} = g\beta H_0 M + AmM + O[B^2/2g\beta H_0]$$

where M and m are electronic and nuclear magnetic quantum numbers respectively, and the last term on the RHS represents the second order correction of the order of $(B^2/2g\beta H_0)$. The first order wavefunctions are given by

$$\begin{aligned} |1/2, m\rangle' &= |1/2, m\rangle + \frac{BI_m}{g\beta H_0} |-1/2, m+1\rangle \\ |-1/2, m\rangle' &= |1/2, m\rangle + \frac{BI_m}{g\beta H_0} |1/2, m-1\rangle \\ |-1/2, m+1\rangle' &= |1/2, m+1\rangle + \frac{BI_{m+1}}{g\beta H_0} |1/2, m\rangle \end{aligned}$$

and so on. Here $|1/2, m\rangle'$ is an unperturbed wavefunction and $|1/2, m\rangle$ is a perturbed wavefunction, and $I_m = \langle m+1 | I_+ | m \rangle = [I(I+1) - m(m+1)]^{1/2}$. The ordinary hyperfine transitions are between states described by $|1/2, m\rangle'$ and $|-1/2, m\rangle'$ (figure 5.6) and do not involve a change in the nuclear magnetic quantum number. These occur at

$$h\nu = g\beta H + \frac{Am}{2} + O(B^2/2g\beta H)$$

But transition between states like $|1/2, m\rangle'$ and $|-1/2, m+1\rangle'$ can also take place because of the mixtures, but only through a M.W. field parallel to H_0 . These are illustrated by dashed lines in figure 5.6. These transitions occur at

$$h\nu = g\beta H + \frac{A}{2} (m + 1/2) + O(B^2/2g\beta H)$$

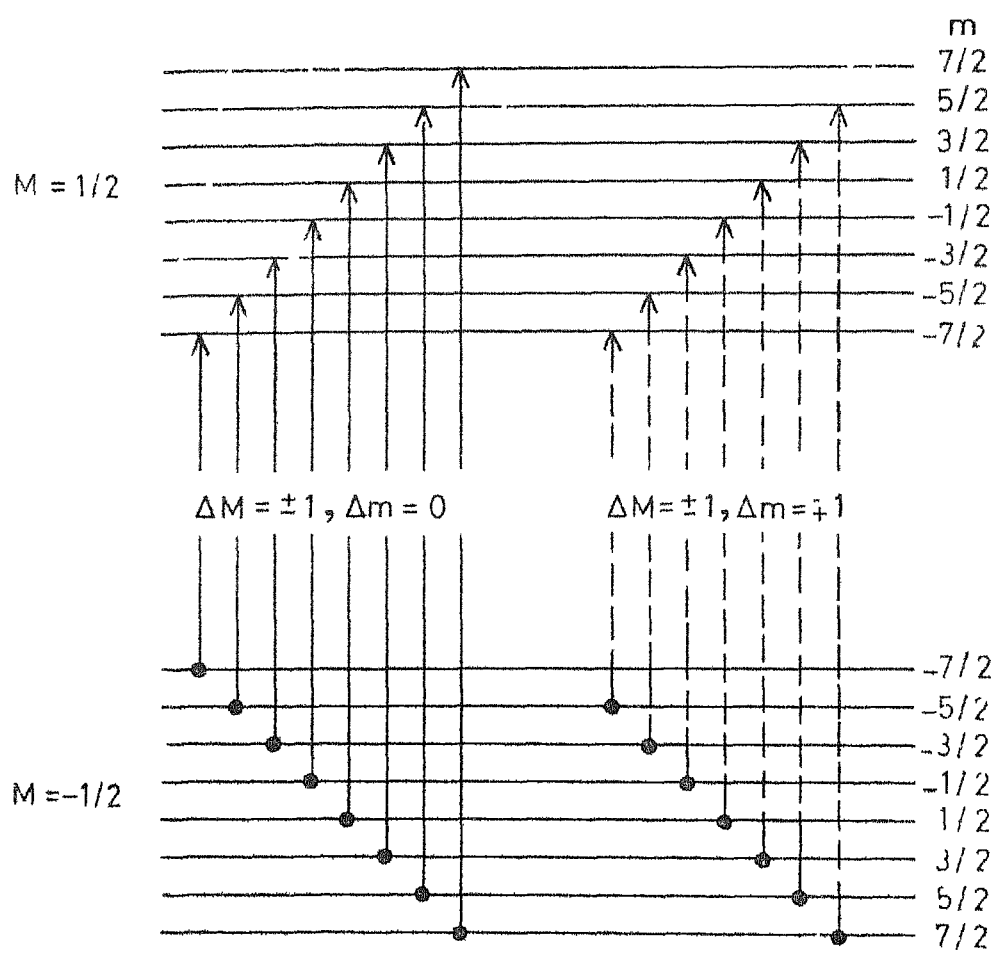


Fig.5.6 Allowed and forbidden hyperfine transitions of a spin $1/2$ system

that is, exactly midway between the allowed transitions (but for the second order terms). The intensity of these transitions is proportional to the mixture co-efficients and is only a few percent of the allowed lines (0.5 to 1% here). Also all the $2I$ lines do not have the same intensity. They vary as $[I(I+1)-m(m+1)]$ where m is magnetic quantum number of the upper nuclear state.

In the present experimental set up where for angles of $\theta \neq 0$, (figure 5.1) the microwave field has a component parallel to H_0 , such transitions are indeed observed. Figure 5.7 illustrates the spectra recorded with H_0 parallel to the c axis but one with H_0 in the XX orientation and the other YY orientation. The forbidden lines X_1-X_7 and Y_1-Y_7 occurring midway between the respective allowed lines can be clearly seen. Their relative intensities also vary as expected. Such forbidden lines were earlier observed in Cobalt, manganese and Vanadyl salts¹¹.

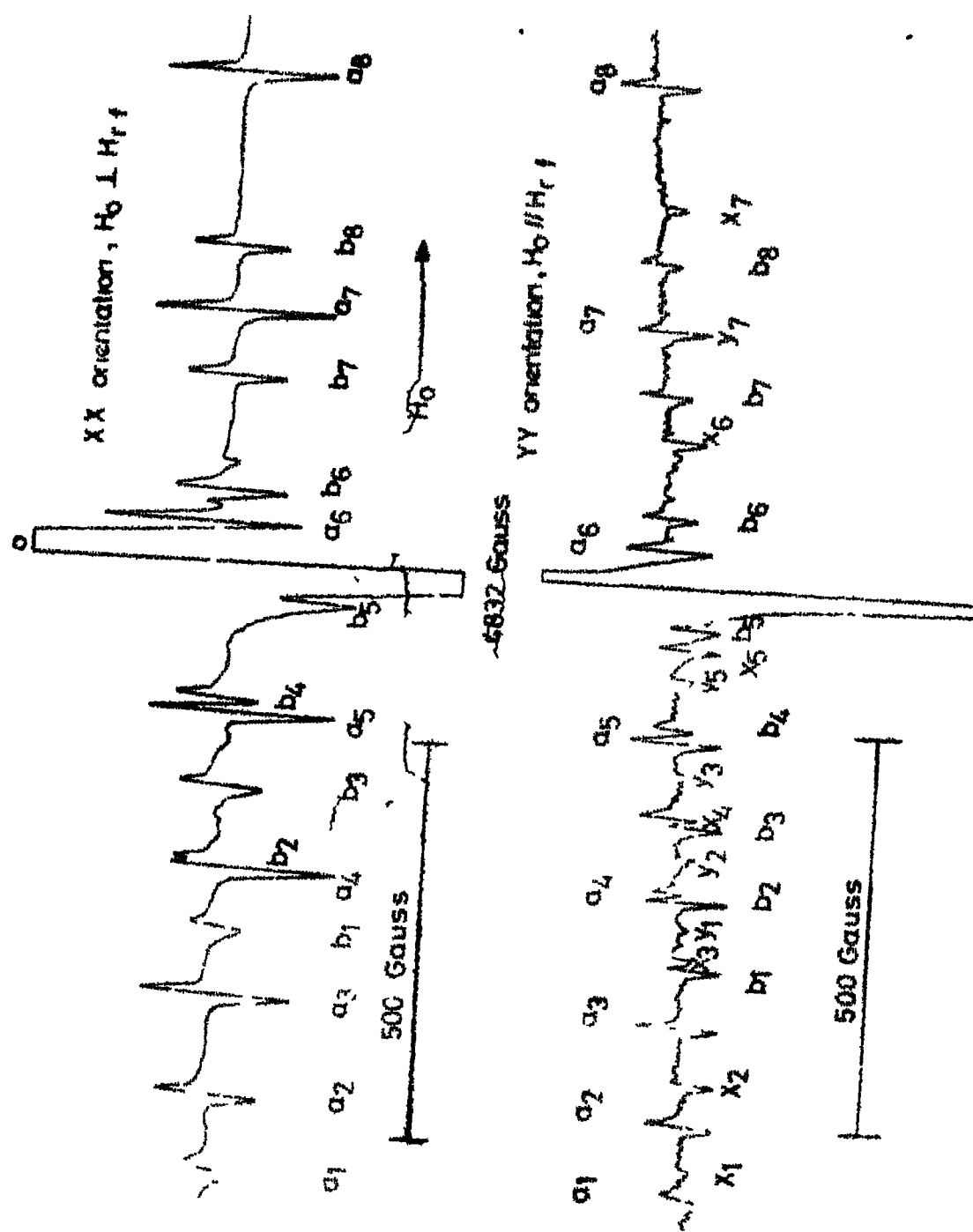


Fig 57 The EPR spectrum of Nd^{3+} PbMoO_4 at 4.2°K with H_0 along showing forbidden hyperfine lines, x_1 — x_7 and y_1 — y_7

REFERENCES

1. Chapter 4 of this thesis.
2. I.S. Minhas, A study of the Optical Properties of $\text{Nd}^{3+}:\text{PbMoO}_4$ system. Thesis submitted to IITK, Kanpur 1972; I.S. Minhas, K.K. Sarma and J.B. Gruber, Phys. Rev. 8, B385 (1973).
3. A. Abragam and B. Bleaney, Electron Paramagnetic Resonance of Transition Ions (Oxford 1970).
4. U. Rannon and D.N. Stammers, Rev. Sci. Instrum 41, 147 (1970).
5. J.M. Baker and R.S. Rubins, Proc. Phys. Soc. 78, 1353 (1961); E.Y. Wong, G.M. Stafsudd and D.R. Johnston, Phys. Rev. 131, 990 (1963).
6. R.W.G. Wyckoff, Crystal Structures, Vol. 3 (Interscience 1965).
7. I.N. Kurin and L.Ya. Shekun, Soviet Phys. Solid State 6, 1144 (1964).
8. I.N. Kurin, ibid. 8, 585 (1966).
9. V. Volterra, J. Bronstein and M. Rockni, Appl. Phys. Letters 8, 212 (1966).
10. W.B. Mims and R. Gillen, Phys. Rev. 148, 438 (1966).
11. C.D. Jeffries, Phys. Rev. 106, 164 (1957),
M. Abragam, R.W. Kedzie and C.D. Jeffries, Phys. Rev. 106, 165 (1957),
Weston A. Anderson and Lawrence H. Pittle, J. Chem. Phys. 30, 591 (1959).

